2013

Enhanced pool boiling of water with open microchannels over cylindrical tubes

Jeet Mehta

Enhanced Pool Boiling of Water with Open Microchannels over Cylindrical Tubes

by

Jeet S. Mehta

A Thesis Submitted in Partial Fulfillment of the Requirements for the Degree of Master of Science in Mechanical Engineering

Approved by:

Dr. Satish G. Kandlikar Department of Mechanical Engineering	(Thesis Advisor)
Dr. Robert J. Stevens Department of Mechanical Engineering	(Committee Member)
Dr. Denis R. Cormier Department of Industrial Engineering	(Committee Member)
Dr. Wayne W. Walter Department of Mechanical Engineering	(Department Representative)

Thermal Analysis, Microfluidics, and Fuel Cell Laboratory
Department of Mechanical Engineering
Kate Gleason College of Engineering
Rochester Institute of Technology
Rochester, New York 14623
February, 2013

Abstract

Pool boiling is a stable and efficient method for transferring large quantities of heat. It is employed in a wide range of applications, including steam generation in boilers, petrochemical, pharmaceutical, cryogenic and many other industrial processes. The objective of this work was to investigate the augmentation in the boiling heat transfer rates with an array of open microchannels over a cylindrical tube. In order to develop high performance surfaces, rectangular and V-groove cross-sectional geometry microchannels were fabricated and tested over tubular test sections. These microchannels were manufactured in two configurations: circumferentially around the test section and axially along the length. The effects of the microchannel geometric parameters on pool boiling performance were studied under horizontal and vertical orientations. Twenty uniquely modified microchannel surfaces were designed, fabricated and tested. The best performance was obtained with a circumferential rectangular microchannel test section in the horizontal orientation. A maximum heat transfer coefficient of 129 $kW/m^2 \cdot K$ was achieved at a heat flux of 1095 kW/m^2, while maintaining a wall superheat of 8.5 K. The overall enhancement factors obtained at the maximum heat flux condition, ranged between 1.9 and 3.4 in the horizontal orientation, and 2.1 and 3.1 in the vertical orientation. The critical heat flux for almost all the designed test surfaces was increased by a factor of at least 1.6 over a plain tube. Area normalized results indicated that factors other than area enhancement are responsible for augmenting the heat transfer performance. High-speed videography of bubbles nucleating, growing and departing from the heated surface was performed. The bubble behavior over these open microchannels was analyzed to understand the fundamental mechanism during pool boiling. The bubble interactions in and over the open microchannels, and the liquid rewetting phenomenon greatly influence the heat transfer performance for these surface.

Acknowledgement

I would like to take this opportunity to thank everyone for their help and support. I am extremely grateful to my advisor Dr. Kandlikar for giving me the opportunity to work under his guidance. You have been an endless source of encouragement and motivation. I greatly appreciate the design discussions that we had on various projects, and the insightful information that improved my knowledge as an engineer. The confidence you have shown in my work inspires me to always deliver the best performance. I would like to thank the committee members for taking the time to review and evaluate my thesis work.

I would like to specially thank Dave Hathaway and William Finch for their personal support and guidance over the years. I am also grateful to Robert Kraynik and Jan Maneti at RIT's Mechanical Engineering machine shop, for their constant guidance and patience during the fabrication of the experimental setups for the various projects. I am also thankful to Dr. Hensel and the staff of the mechanical engineering department for advising me during the course of my graduate studies at RIT. I am thankful to all the members of the Thermal Analysis, Microfluidics, and Fuel Cell Laboratory, for their assistance and support throughout my time at RIT.

Finally, I would like to thank my parents and sister for their support and for giving me the opportunity to have this wonderful experience. I know the distance has been very hard on all of us, but your constant encouragement and love made this possible. I love you very much. Special thanks to all my friends who have always been there for me. I hope my accomplishment today gives all of you a reason to be proud of me.

Table of Contents

List of Figures

List of Tables

Nomenclature

A_s	projected surface area at the outer diameter, m^2
h	heat transfer coefficient, $W/m^2 \cdot K$
I	current supplied, A
k	thermal conductivity of copper, W/m·K
L	test section length, m
$q_{a,l}$	axial heat losses, W
q_h	total heat input, W
q_r	resultant radial heat output, W
q_r''	resultant radial heat flux at the outer diameter, W/m^2
r_1	radius for thermocouple location inside the test section, m
r_2	test section outer surface radius, m
$T_1 - T_4$	temperature inside test section at locations 1 – 4, °C
T_5	bulk liquid temperature, °C
T_{ave}	average temperature inside the test section at radius r_1, °C
T_s	surface temperature at the outer diameter, °C
ΔT	wall superheat, K
U_{T_s}	uncertainty in the surface temperature, °C
$U_{q_r''}$	uncertainty in the resultant radial heat flux, W/m^2
U_h	uncertainty in the heat transfer coefficient, $W/m^2 \cdot K$
V	voltage applied, V

Abbreviations

ARM	Axial Rectangular Microchannels
CHF	Critical Heat Flux
CRM	Circumferential Rectangular Microchannels
CVM	Circumferential V-groove Microchannels
ONB	Onset of Nucleate Boiling

1. Introduction

Heat transfer in nature can be broadly classified into three physical mechanisms, namely, conduction, convection, and radiation. Conduction is the transfer of energy in the form of heat from particles at higher energy to particles at lower energy due to the interaction between these particles. In convection, the heat transfer is mainly due to the motion of the fluid and conduction within the fluid. Radiation is the transfer of heat from a material in the form of electromagnetic waves.

Convective heat transfer is widely used for various heating and cooling applications. Heat exchangers work on this principle mechanism. Convection heat transfer can be further classified into three categories:

1. Free or natural convection: Fluid motion occurs mainly due to the buoyancy forces created by the temperature variations in the fluid.
2. Forced convection: Fluid motion is induced by external forces to increase the rate of heat transfer.
3. Convection with phase change: Heat transfer occurs due to the change of phase of the fluid, therefore an additional transfer of heat, equivalent to the latent heat of the fluid is observed.

The rate of convective heat transfer in a system is given by the Newton's law of cooling.

$$q" = h_c\,(T_S - T_\infty)$$

Where $q"$ is the heat flux, h_c is the convective heat transfer, and T_S and T_∞ are the surface and fluid temperatures, respectively. An approximate range of heat transfer coefficients for different modes of convective heat transfer are given in Table 1 reproduced from [1].

Convective heat transfer mode	h_c (W/m^2·K)
Free convection – Gases	2 – 25
Free convection – Liquids	50 – 1000
Forced convection – Gases	25 – 250
Forced convection – Liquids	50 – 20,000
Convection with phase change – Boiling	**2,500 – 100,000**

Table 1: Standard heat transfer coefficient ranges for convective heat transfer modes [1]

Heat transfer to boiling liquids or from condensing vapor is a convection process that involves a change of phase from liquid to vapor or vapor to liquid respectively. As seen from Table 1, very high heat transfer coefficients are observed during the boiling process due to additional heat removal equal to the latent heat of the fluid.

1.1 Boiling

The boiling heat transfer phenomenon can be further classified into forced convection boiling and pool boiling. In forced convection boiling, liquid motion is due to an external force and the mixing of fluid is a result of the boiling process which includes bubble growth and departure, whereas in pool boiling, the liquid motion and mixing near the heated surface are induced solely by the growth and departure of nucleating bubbles. The noticeably high heat transfer coefficient observed in the boiling process is due to the addition of the latent heat of vaporization associated with the phase change from liquid to vapor. The heat transfer during the boiling process is highly advantageous in systems that generate large quantities of heat over a relatively small area. The numerous difficulties and instabilities observed in the flow of the two phase fluid in forced convection boiling hinder its successful application in various high heat removal systems. Hence extending critical heat flux and improving heat transfer coefficient is of great interest in pool boiling.

1.2 Pool Boiling

Pool boiling is a simple heat transfer system consisting of a heating element immersed in a pool of saturated liquid and the heat transfer occurs on the surface of the heating element. The high heat transfer coefficient observed in the pool boiling process is due to the change of phase of the fluid. Pool boiling is a highly efficient process for removal of large quantities of heat from a heated surface. This heat transfer system does not employ any moving parts, therefore no external power is necessary for its operation which makes this system very attractive even from the cost perspective. Notable applications of this process are two phase heat exchangers and evaporators, boilers and steam generators. Extensive studies have been conducted on boiling heat transfer technique to further enhance its performance. The pool boiling performance and its behavior over a surface are represented using a boiling curve which depicts the various heat transfer mechanisms observed during the boiling process. In the next section, the boiling curve and the associated boiling heat transfer mechanisms are identified and explained in detail.

1.3 Boiling Curve

The boiling curve quantifies the heat dissipation ability of a surface through the boiling process. The different heat transfer mechanisms observed during the boiling process at different heat flux conditions are explained using this curve. Shown in Figure 1, reproduced from [2], is a boiling curve which is a plot of the heat flux, q'' (W/m^2) versus the temperature difference between the boiling surface and the fluid saturation temperature, ΔT (K), also known as the wall superheat. The curve is representative of the ability of a given surface-liquid pair to dissipate heat. The various regimes observed during pool boiling of a fluid are depicted in Figure 1.

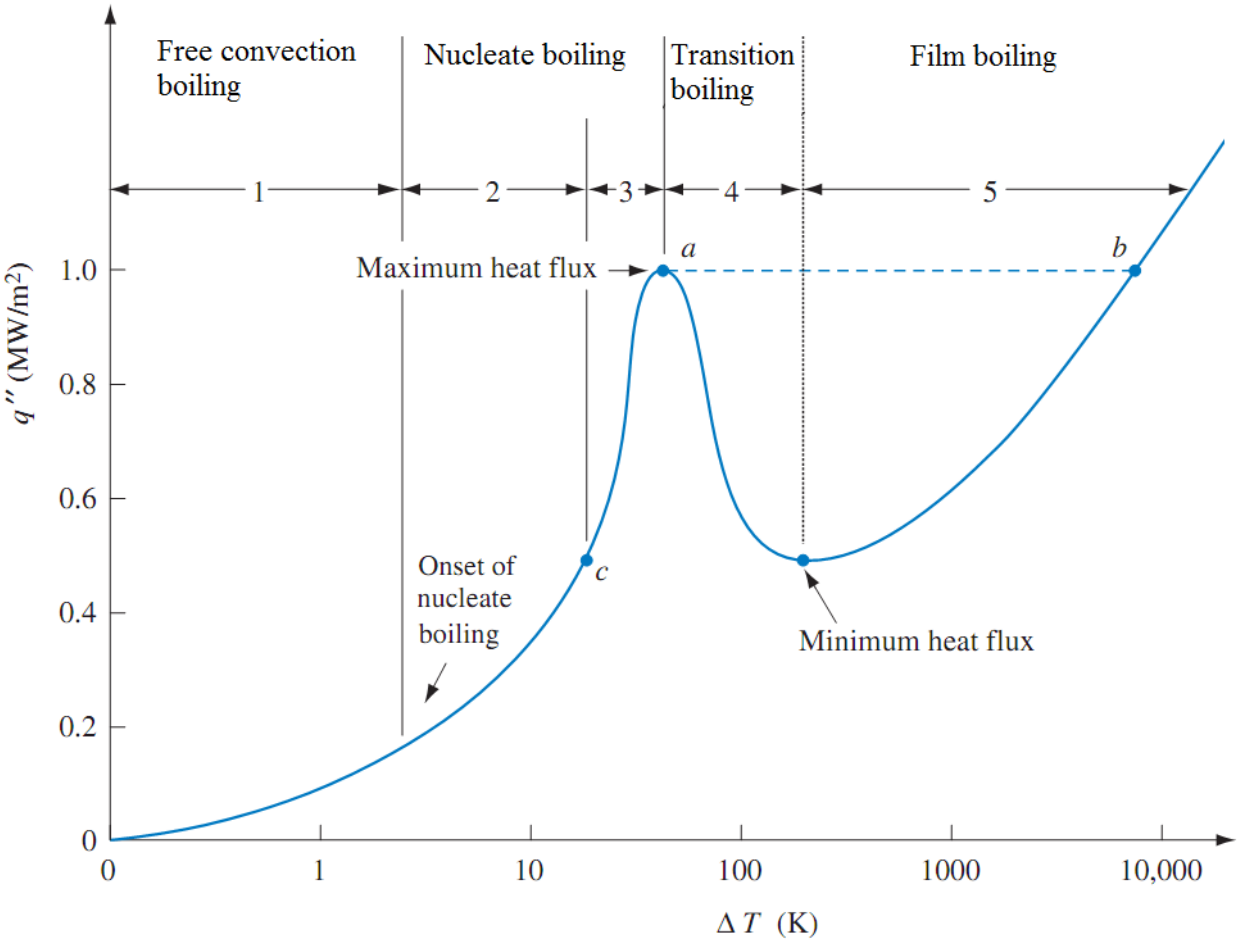

Figure 1: Typical pool boiling curve for saturated water at atmospheric pressure [2]

1.3.1 Free convection

This is the first regime of the boiling process and is shown as region 1 in Figure 1. In this portion of the boiling curve, free convection is observed and a representative schematic of this mechanism is shown in Figure 2(a), reproduced from [2]. The wall superheat in this region is insufficient for the nucleation of bubbles over the given surface. As the wall superheat increases, bubble nucleation initiates over the surface. The condition at which bubbles start nucleating over the given surface is known as the Onset of Nucleate Boiling (ONB), which is indicated in Figure 1. A representative schematic of this condition is shown in Figure 2(b).

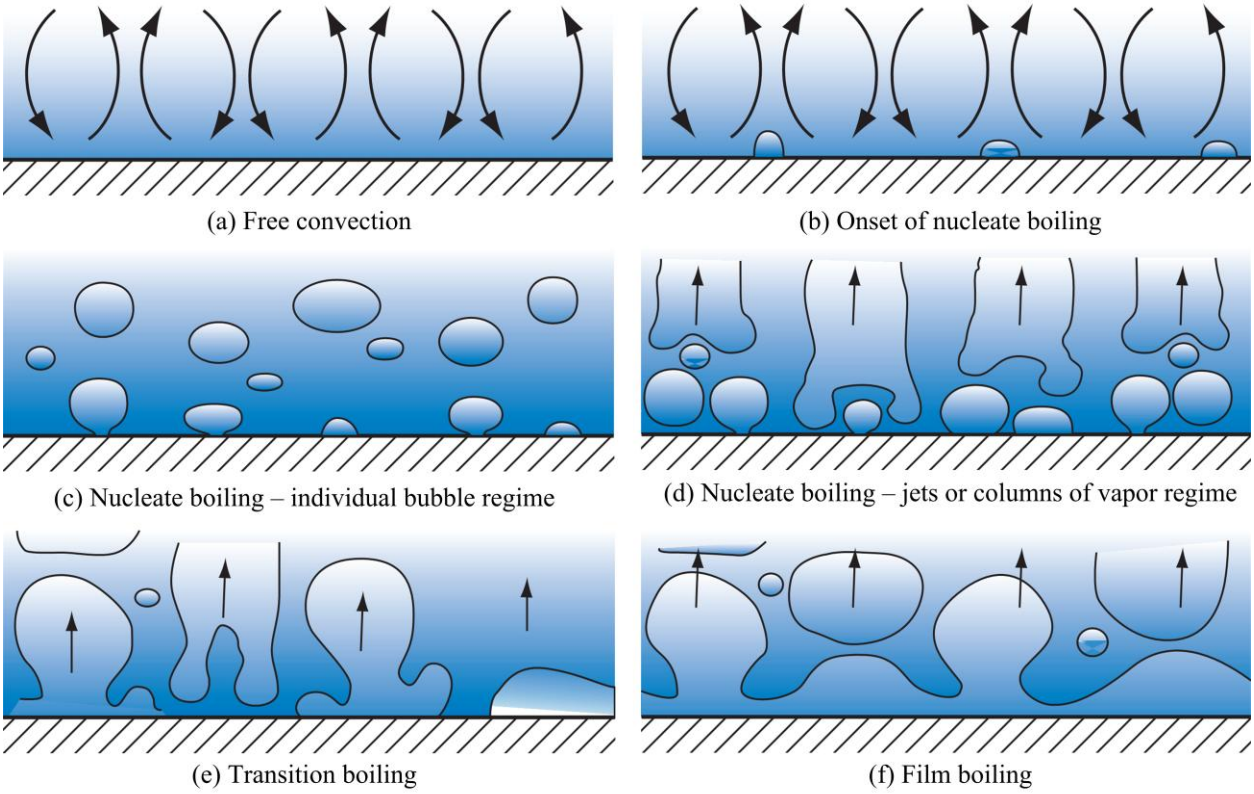

Figure 2: Boiling mechanisms observed during pool boiling over a surface [2]

1.3.2 Nucleate boiling

After the ONB condition is reached, the regime of nucleate boiling is observed. This regime is depicted by regions 2 and 3 on the boiling curve (Figure 1). As the wall superheat increases, the number of nucleation sites on the heated surface also increase. In region 2 of this regime, individual bubbles nucleate and rise through the liquid. This is known as the individual bubble regime or partial nucleate boiling regime. A representative schematic of this mechanism is shown in Figure 2(c). As the wall superheat increases further, the rate of bubble generation and the bubble departure velocities increase. These high bubble generation rates combined with increased nucleation sites over the surface, lead to the interaction between adjacent bubbles. These adjacent bubbles coalesce to form jet or columns of vapor through the pool of liquid. This

regime is known as the slugs or columns of vapor regime, or fully developed nucleate boiling regime. This regime is indicated as region 3 in Figure 1. A representative schematic of this phenomenon over the surface is shown in Figure 2(d). Highest heat transfer rates are seen in this regime. The maximum heat flux achievable in this regime is known as the Critical Heat Flux (CHF), which is shown by the point 'a' in Figure 1. This limit has direct implications on the safe operation of a system and will be further explained in Section 1.4. Heat transfer rates observed close to the CHF limit are very high. Operation under such conditions is highly advantageous in the removal of large quantities of heat.

1.3.3 Transition boiling

As the heat flux is increased above the CHF limit the boiling mechanism transitions from the nucleate boiling regime directly into the film boiling regime, as shown by the dotted line 'ab' on boiling curve (Figure 1). This transition from the nucleate boiling regime into the film boiling regime is only seen in increasing heat flux systems. Whereas in a temperature controlled system, as the temperature increases further the heat transfer rate sharply decreases. This decrease is observed due the formation of an unstable film of vapor over the surface which obstructs the continuous wetting of the surface by the liquid. As the temperature increases further, the stability of this film of vapor increases and the heat transfer rate reduces. This regime is indicated by region 4 on the boiling curve in Figure 1, and a representative schematic is shown in Figure 2(e).

1.3.4 Film boiling

The film boiling regime is shown as region 5 on the boiling curve (Figure 1). As the temperature increases a minimum heat flux is reached. At this point a stable film of vapor encapsulates the entire heated surface. The stability of the film completely obstructs the contact of liquid with the surface. The heat transfer mechanism in this regime is through the film of

vapor, resulting in very low heat transfer coefficients. For an increasing heat flux system the change of mechanism from nucleate boiling to the film boiling is observed. After point ‘b’ on the boiling curve (Figure 1), a steady increase in the heat flux leads to a further increase in the wall temperature. A representative schematic of the film boiling mechanism is shown in Figure 2(f).

1.4 Critical Heat Flux (CHF)

The CHF condition in the boiling process is of great importance. At heat fluxes lower than the critical heat flux maximum heat transfer is observed for a given surface-liquid combination. The boiling performance in terms of the heat transfer coefficient is the highest at this condition, making it is highly advantageous and efficient to operate a system close to its CHF limit. However after reaching the critical heat flux condition, an uncontrolled thermal condition is reached which leads to a spike in the wall superheat due to a decreased heat transfer rates in the film boiling regime. The increased wall temperatures may lead to the failure of the material or system. Hence an extensive study of this condition is very important.

In practical applications such as steam generators, boiling water reactors, and boilers, the critical heat flux is the limiting factor of operation. In such continuous heat input systems it is very dangerous to operate these systems close to their CHF conditions. If the CHF condition is reached, the wall temperature may rise to the melting point of the material employed, and lead to the failure or destruction of the system. As a result, precautions are taken to avoid reaching the CHF limit by operating these systems at much lower heat fluxes, decreasing the overall efficiency of the system. It has been observed that surface modifications can increase the heat transfer rates for a given system, as well as extend the CHF limitations for a given surface.

2. Literature Review

Over the past few decades, extensive research towards augmenting the performance of nucleate boiling heat transfer has been conducted. Numerous enhancement techniques have been researched on, in order to improve the overall heat transfer performance. Out of these techniques, surface modifications have proven to be a viable and efficient option. A number of different surface enhancement techniques are employed in pool boiling. They can be broadly classified into the following four categories.

1. Re-entrant cavities: This type of surfaces are developed using various manufacturing techniques such that larger cavities with desirable mouth openings are generated. These cavities act as nucleation sites by trapping vapor thereby enhancing the heat transfer performance. This type of enhancement has been researched in great detail, and different types of re-entrant cavities are further discussed in Section 2.1.

2. Porous surface: In this type of enhancement a porous matrix of metallic or non-metallic material is coated over the boiling surface or the heater. Using this technique numerous micro and nano pores are created on the surface, which act as nucleation cavities for enhanced bubble generation at much lower surface temperatures. The heat transfer performance achieved mainly depends on the pore dimensions, material of the coating, and the number of active nucleation sites on the surface.

3. Surface roughness and tube orientation: In literature, the surface roughness has shown to nominally influence the heat transfer rates, but is one of the simplest enhancement techniques presently employed. The orientation of the tube has also shown to affect the

heat transfer rate, and can be used as a simplistic enhancement mechanism in the design of various systems.

4. Open microchannels/Integral fins: In this technique, either microchannel grooves or integral fins are generated on the heating surface. The bubble dynamics in and over these microchannels largely dictate the performance of the surface at high heat flux conditions. Most importantly, the rewetting phenomenon observed with this surface enhancement technique is highly advantageous in augmenting the overall heat transfer performance and improving the critical heat flux limit. The details of this technique are further explained in Section 2.4.

Table 2 provides a comprehensive summary of the available literature in the area of pool boiling heat transfer over cylindrical tubes using various surface modification techniques. This table summarizes the enhancement technique employed, surface material, diameter and length of the tested tube, operational heat flux range, and the overall heat transfer enhancement factors observed by various researchers in the past several years. The table also includes a column with some conclusions and comments.

2.1 Re-entrant Cavities

This technique has been widely studied in the past two decades and different methods of generating re-entrant cavities over the heated surface have been developed and established. The re-entrant cavities are fabricated such that they trap vapor to act as nucleation sites and aid in nucleation process, thereby augmenting the heat transfer performance. They have shown to enhance the overall performance by a factor of least 3 or 4. In 1992, Webb and Pais [3] tested four GEWA series re-entrant cavity tubes with five different refrigerants. These re-entrant cavity

tubes were generated by further modifying simple finned tubes. They tested these surfaces with R11, R12, R22, R123 and R134a at saturation temperatures of 4°C (39°F) and 27°C (80°F), and concluded that the better heat transfer rates were observed at the saturation temperature of 27°C (80°F). Memory et al. [4] in 1995 used the commercially available re-entrant cavity tubes such as the GEWA series, Thermoexcel and Turbo tubes to evaluate their respective heat transfer enhancements. Repre4sentative schematic for the GEWA-T and YX re-entrant cavity structures are shown in Figure 3. Their experimental results showed up to 5.5 times higher heat transfer coefficients for the GEWA series tubes, and an enhancement of up to 20 times for the Thermoexcel and the Turbo tubes, but at fairly low heat flux conditions. As the heat flux increased the performance enhancement for these re-entrant cavity tubes reduced significantly, and was similar for all the tubes.

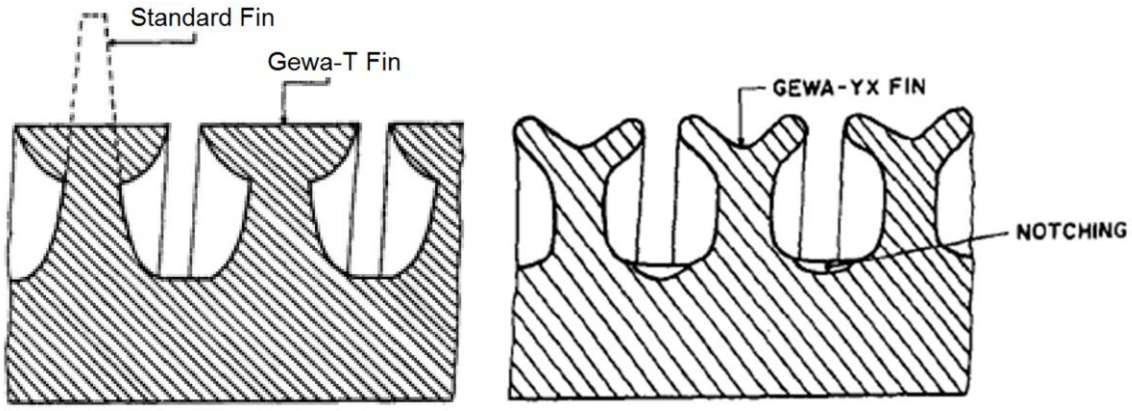

Figure 3: GEWA-T and YX re-entrant cavity surfaces [4]

Huebner and Kunstler [5] tested similar re-entrant cavity copper tubes with n-hexane and propane, and observed enhancement factors in the range of 2.4 – 4. Tatara and Payvar [6] used R134a with a commercially available TURBO-BII-HP tube and reported 60 – 90% further increase in the heat transfer rates compared to the previous generation TURBO-B tube. Rajulu et al. [7] fabricated their own simple re-entrant cavity tubes by modifying the tips of the finned

tubes. Their results showed an enhancement of up to 2.5 times. They observed a slight drop in the enhancement factor with an increase in the heat flux condition. In their study, they also developed a correlation for the enhancement factor as a function of the heat flux and the cavity width of the re-entrant channels.

Jung et al. [8, 9] used various working fluids to study the performance of two re-entrant tubes, and observed that the heat transfer enhancements at low heat fluxes were significant. They concluded that the rate of increase in heat transfer to the increase in heat flux was small, possibly because of the blockage of the liquid re-entry into the tunnels through the pores due to the departing bubbles. The experimental data from their two studies showed a 40% greater enhancement for flammable refrigerants compared to halogenated refrigerants. Ribatski and Thome [10] tested GEWA-B, TURBO-CSL and TURBO-BII-HP tubes and obtained enhancement factors of 2.4 – 5.2, 2.4 – 2.9 and 1.9 – 7.0 times, respectively, for high to low heat flux range. Ji et al. [11] in 2010 tested re-entrant cavity tubes with refrigerant and lubricant mixtures. They concluded that tubes with narrower cavity mouth widths performed better at low heat fluxes, whereas tubes with wider cavity mouth widths performed better at high heat fluxes. They also observed that at higher heat fluxes the overall enhancement in the heat transfer coefficient was relatively poor.

Chien and Webb [12-15] developed re-entrant cavities by wrapping pored foils over the outer surface of finned tubes. They performed a parametric study of the pore diameter, the tunnel pitch and width, and the fin height and a schematic is shown in Figure 4. From their results, they concluded that a greater fin height and a smaller tunnel pitch aided in achieving better performance. Also the sharp tunnel edges filled with liquid were responsible for the subsurface heat transfer. They recommended finned tubes with rectangular base tunnels, and fin heights of

0.7 – 1.0 mm for enhancing the heat transfer performance. Their heat transfer performance results obtained for a finned tube covered with copper pored foil is shown in Figure 5.

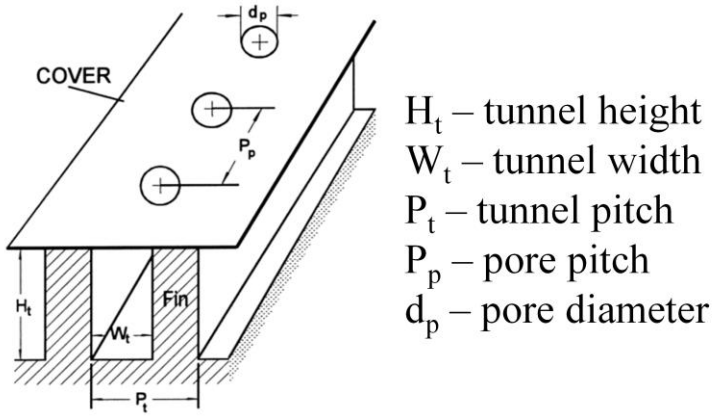

Figure 4: Schematic of porous foil covers on finned tubes [12-14]

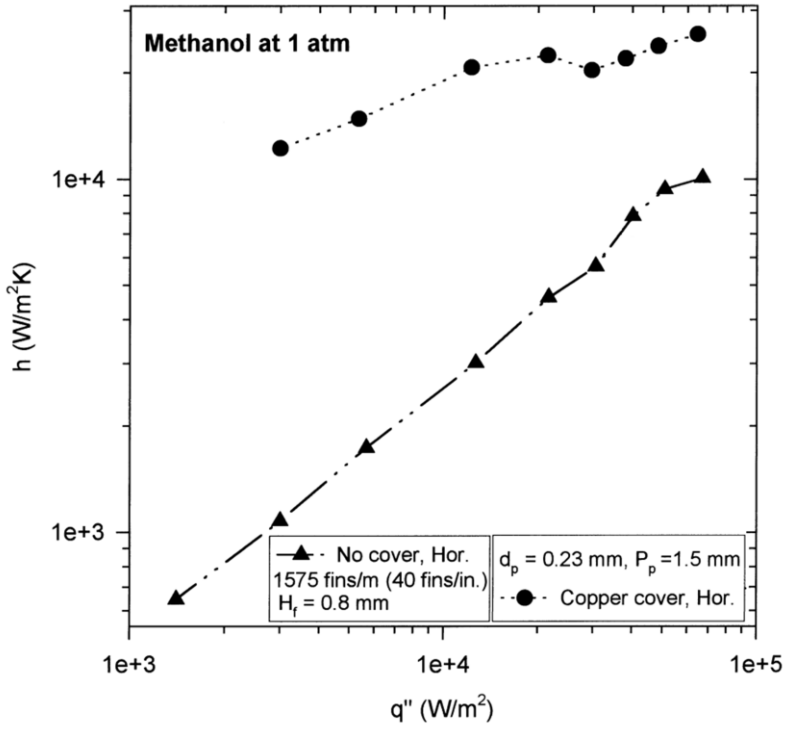

Figure 5: Heat transfer performance results with copper covers over finned tubes [12-14]

Kim and Choi [16] fabricated similar tubes consisting of pores with subsurface connections and observed enhancements of up to 5 – 6.5 times. They concluded that the

subsurface connections aided in continuously supplying liquid to the heated surface and delayed dry-outs. Kulenovic et al. [17] employed structured pores and observed good enhancements in the low to medium heat flux ranges. But at high heat flux conditions, they observed deactivation of the re-entrant cavities. Chen et al. [18] conducted a parametric study of channel widths of 0.05 – 0.2 mm and elliptical pores of 0.01 – 0.1 mm by 0.15 – 1.5 mm. They tested these tubular surfaces in the horizontal orientation, and their results showed 2 – 4 times enhancement in performance over the plain tube.

Chien and Huang [19] used a brass wire mesh cover over a finned copper tube and achieved enhancements of up to 7 – 8 times with R134a at a saturation temperature of 5°C (41°F). They obtained the best performance on a tube with 1524 fins/m and a fin height of 0.4 mm covered by a size 100 mesh. Kotthoff et al. [20] and Gorenflo et al. [21, 22] developed, and extensively tested macro and micro re-entrant cavity surfaces. The macro cavities are used for experimentally testing the effects of re-entrant cavities, and the micro cavities are used for visually understanding the mechanism at the heated surface using high-speed cameras. An uneven circumferential temperature distribution was observed over the heated surface while testing in the horizontal orientation. Experimental results for the re-entrant cavity tubes showed a 45% increase in the overall heat transfer performance compared to the plain tube. They concluded that the re-entrant cavities with narrower mouth openings performed better, as was also concluded by Ji et al. [11]. Number of other investigators have used similar re-entrant cavity surfaces and evaluated the enhancements for various working fluids. Significant enhancements in the heat transfer rates were observed for a given surface temperature using these surfaces, but were limited to the low heat flux range.

2.2 Porous Surfaces

Another commonly employed technique for surface modification to enhance the heat transfer performance is to generate a porous surface over the heated tube. The use of a porous coating over the tube significantly increases the number of active nucleating sites on the surface, which aids in augmenting the heat transfer performance. Hsieh and Yang [23] in 2001 studied the heat transfer mechanism using a porous layer matrix over a heated surface. Their results confirmed the earlier hypothesis of nucleation and evaporation taking place inside the porous matrix under steady boiling conditions. They also studied the effect of porous layer thickness on the heat transfer performance. Cieslinski [24] conducted an extensive parametric study of the porous layer coatings of different materials such as copper, aluminum, molybdenum, zinc and brass. He used water as the working fluid, and concluded aluminum coatings offered the best heat transfer performance. He observed that the boiling process commenced at much lower wall superheats of 0.1 K compared to 8 K that was observed with a smooth tube as shown in Figure 6.

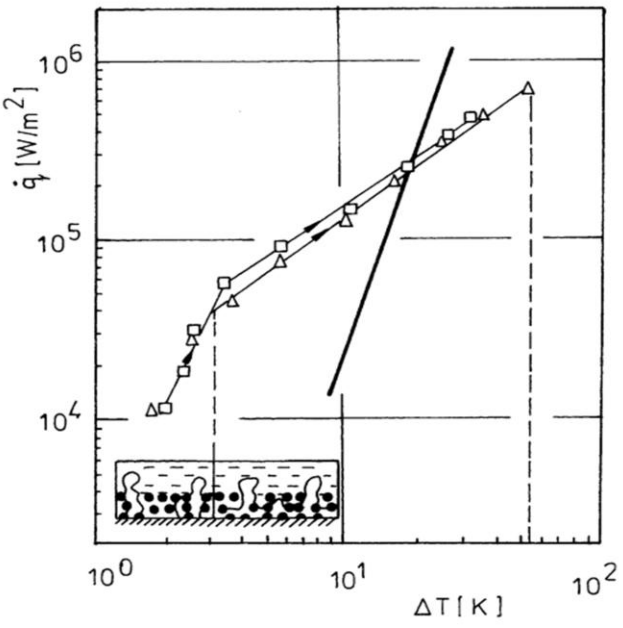

Figure 6: Performance curve comparison for Al porous coated tube and smooth tube [24]

Kim et al. [25] used a porous layer coating over a thin platinum wire and observed an enhancement of up to 3.75 times. They concluded that the porous layer coatings reduced the bubble departure diameter, and increased the bubbling frequency and the number of active nucleation sites. Dominiczak and Cieslinski [26] used distilled water as the working fluid and tested porous aluminum coatings over stainless steel tubes. They studied the temperature distribution over the tube in the horizontal orientation, and made similar observations as Kotthoff et al. [20]. They applied the porous layer coating only over a third of the top half of the tube. Employing this technique they observed a reduction in the circumferential temperature distribution around the tube, due to an increase in the localized heat transfer rates. A few researchers [4, 10, 27] used the commercially available HIGHFLUX porous surface tube and observed heat transfer enhancements of up to 10 times at very low heat flux conditions and the results form one of the studies are shown in Figure 7. But all these researchers observed a similar decline in the overall enhancement factor with an increase in the heat flux.

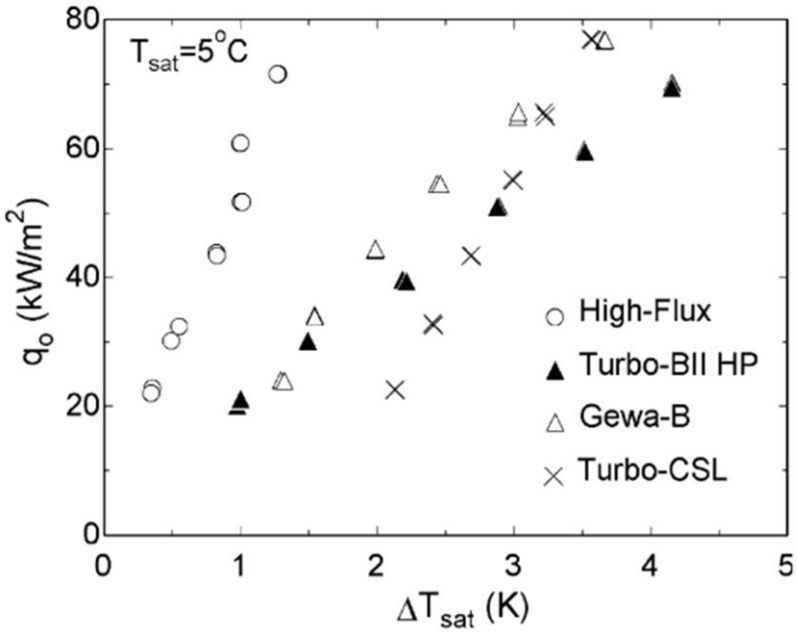

Figure 7: Boiling curves for various enhanced tubes as seen by Ribatski and Thome [10]

2.3 Surface Roughness and Tube Orientation

Surface roughness and tube orientation have shown to have a small effect on the heat transfer enhancement and has been studied by a few researchers. Studies were conducted by Hsieh and Yang [23] and Ribatski and Jabardo [28] by varying the average surface roughness on the boiling surface. Their experimental results showed slight enhancements in the heat transfer performance for higher average roughness surfaces due to an increase in the wetted surface area. The orientation of the heated surface in the pool boiling setup has shown to affect the heat transfer rates in the system. A few researchers have studied the various surfaces in the horizontal and vertical orientations. Kang [29] performed a series of experiments by varying the tube inclination from 0° to 90° in the steps of 15°. His experiments were conducted using water as the working fluid over a stainless steel heated surface. At an inclination of 15° with the horizontal, he observed greater heat transfer rates compared to other inclinations. His results showed enhancements up to 1.25 – 1.4 times, depending on the tube diameter and the wall superheat. He concluded that the main reason for this enhancement was the reduced bubble slug formation on the underside of the tube due to the slight inclination. Chien and Webb [12] also achieved a better heat transfer performance in the horizontal orientation compared to the vertical orientation.

2.4 Open Microchannels/Integral Fins

Microchannel or grooved tubes and finned tubes have been studied for their heat transfer performance over the past several years. They have broadly shown good enhancements in the heat transfer performance over plain tubes. Many researchers [3-5, 7-9, 11] have tested these integral finned tubes with various working fluids, and achieved heat transfer enhancement factors in the range of 2 – 3. Saidi et al. [30] tested microchannel grooves over a copper tube

with R123. They tested two tubes, one with higher channel density and one with lower channel density, with both having nearly similar channel depths. These tubes were tested over a heat flux range of 1.5 – 70 kW/m^2, and their results showed a stable enhancement factor of up to 2.4 times with the higher density channeled tube over the entire heat flux range. The heat transfer coefficients results obtained for the high and low density tubes tested by them are shown in Figure 8.

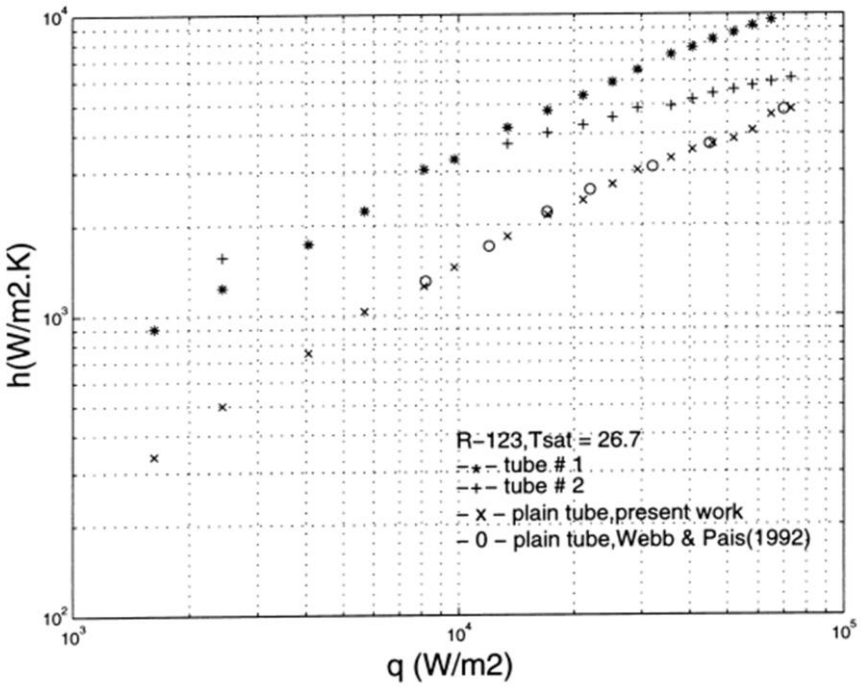

Figure 8: Heat transfer coefficient results for high and low density tubes [30]

Cooke and Kandlikar [31, 32] used open microchannels over a flat silicon and copper surface and achieved significant enhancement in the heat transfer coefficients. Their experimental testing was performed with water as the working fluid. A plot of the boiling curves for all their tested open microchannel surfaces is shown in Figure 9. They conducted a parametric study of the channel depth, channel width, and the fin width. The results of their parametric study showed wider and deeper channels with thinner fins performed comparatively

better. Their results showed heat transfer coefficients as high as 269 kW/m^2·K at a heat flux of 2440 kW/m^2.

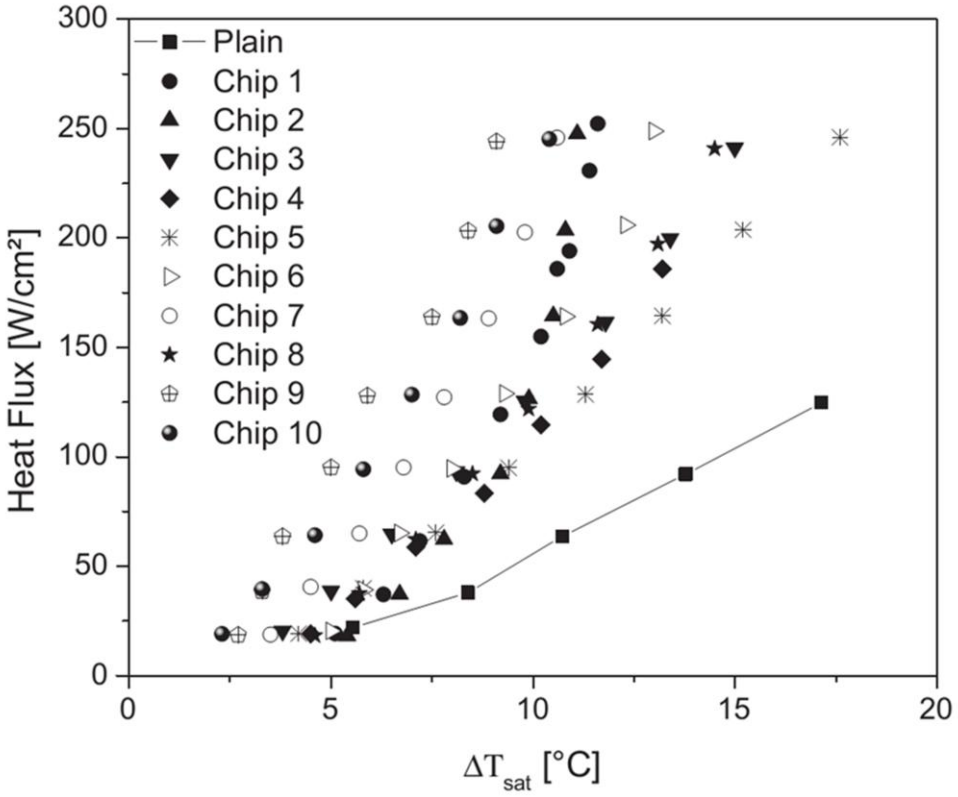

Figure 9: Boiling curves for all the open microchannel over copper test surfaces generated by Cooke and Kandlikar [32]

2.5 Bubble Dynamics

The microchannel enhancement technique employed by Cooke and Kandlikar [31, 32] showed superior heat transfer performance over flat boiling surfaces. They concluded that the re-wetting of the heated surfaces through the open microchannels was indirectly responsible for the superior heat transfer performance. A representative schematic showing the vapor generation and rewetting from their study is shown in Figure 10. The interactions of bubbles nucleating and growing, in and over the microchannel surfaces, were also partially responsible for the

performance enhancement. The pinning of the bubble on the fins of the microchannels, aided in the dissipation of heat from the surface, thereby lowering the wall superheat. In their study they obtained much lower surface temperatures with microchannel surfaces than that observed with plain surfaces.

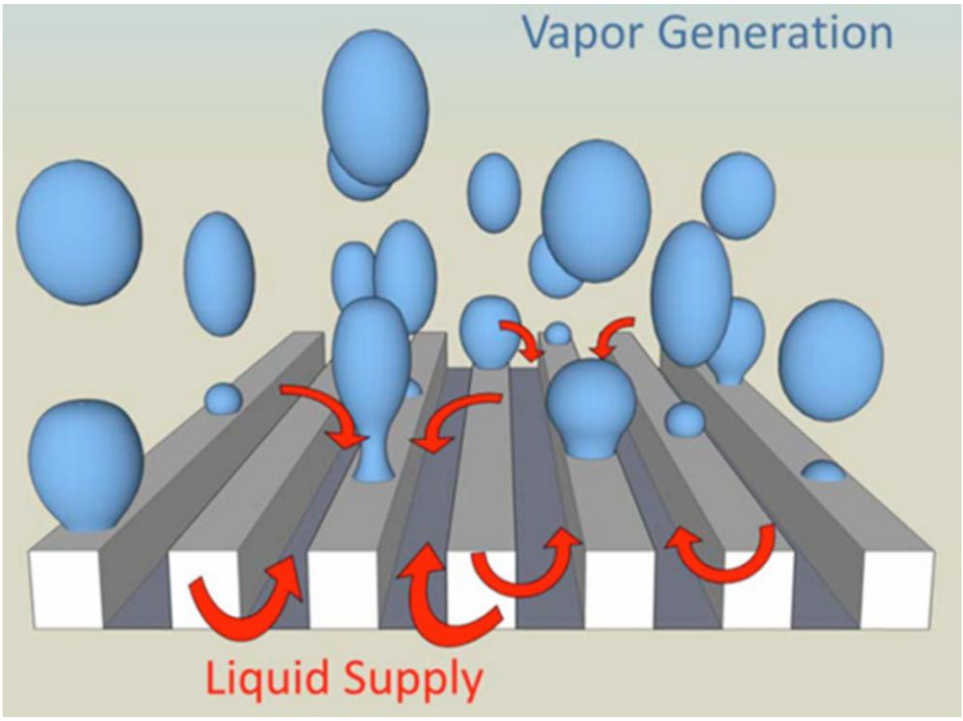

Figure 10: Proposed bubble dynamics mechanism by Cooke and Kandlikar [31]

The bubble dynamics over the modified surfaces have been observed and analyzed by a few researchers with the development of digital high-speed cameras in the past several years. In 1998, Chien and Webb [12] conducted experiments to visualize nucleate boiling using high-speed videography. As described earlier, in their study they used tubes consisting of sub-surface tunnels and surface pores. Their experiments at lower heat fluxes revealed mostly vapor filled tunnels, except for the channel corners which were filled with liquid menisci, which aided in replenishing the tunnels with the working fluid as shown in Figure 11. Kulenovic et al. [17] performed experiments on re-entrant cavity tubes, and similarly visualized the bubble dynamics

using high-speed camera systems. Using Fourier analyses and other correlation techniques, they determined the bubble generation frequency and quantified the upward bubble flow velocity. Chen et al. [18] studied the bubble dynamics over the heated surface and observed higher bubble growth rates and larger departure diameters over the enhanced tubes. Also from their observations they concluded that the enhancements recorded, were due to the evaporation of the liquid film inside the tunnels of their modified test surfaces.

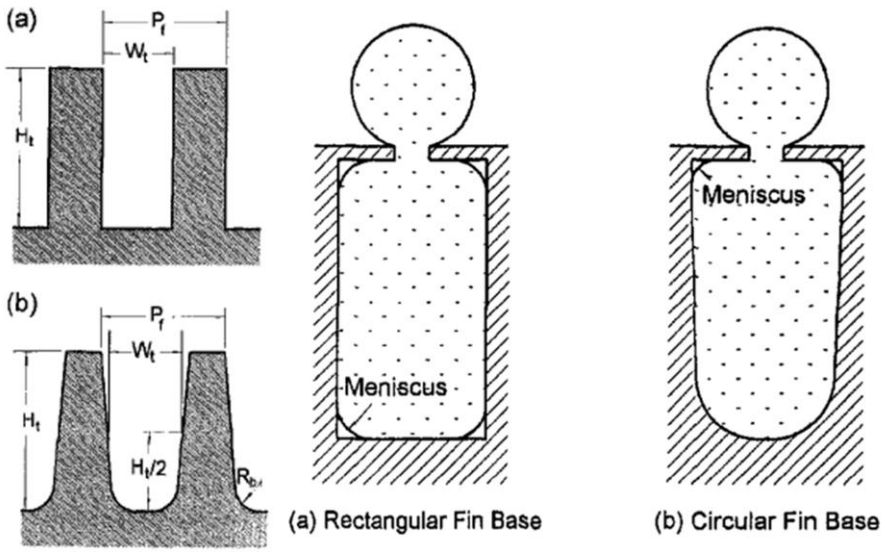

Figure 11: Tunnel cross-sections and liquid menisci as seen by Chien and Webb [12-14]

Hsieh and Yang [23] used tubes with porous coatings and spirally wrapped wires around them, with saturated R-134a and R-600a. They performed visualization studies at low and medium heat flux conditions. Their results revealed a linear increase in the bubbling frequency with increasing heat fluxes. They also observed a slight drop in the bubble departure diameters with an increase in the heat flux. Kim et al. [25] studied the boiling behavior over a wire coated with a microporous later. They observed an increase in the nucleation site density due to microporous layer coating, as the increase in the latent heat transfer augmented the performance. Kang [29] performed work on the effects of inclination of the tube in a pool boiling system as

mentioned earlier. In his study, he used photographs at different tube inclinations to compare the bubble formation and density at various heat flux conditions. He observed an increase in the bubble size with increasing heat flux, differing from the observation made by Hsieh and Yang [23], who used tubes with porous coatings. Since Kang purely studied the effects of tube inclination on performance, the lower number of nucleation sites on the surface necessitated larger bubble departure diameters at high heat flux conditions. As the inclination angle was increased from horizontal to vertical, the generated bubbles were seen to coalesce on the underside of the tubes, and slide off as a large bubble slug. The literature on the bubble dynamics does not clearly focus on the bubble nucleation and grow inside the microchannel groove.

2.6 Literature Review Summary

The literature of re-entrant cavities and porous surface tubes shows significant enhancements in the heat transfer coefficient at low heat flux conditions. But in most cases the enhancement factors sharply decrease as the heat flux increases. Also the heat transfer coefficients observed in literature using these enhancements are in the range of 10 – 50 $kW/m^2 \cdot K$. It has also been observed that none of these enhancement techniques aid in extending the critical heat flux limit for the surface. In literature most of the modifications on the cylindrical tubes were only in the circumferential orientation. Some researchers observed increased heat transfer performance in the horizontal orientation compared to the vertical orientation. Significant performance enhancements were observed with open microchannels over flat surfaces at high heat fluxes, the following research was conducted for similar open microchannels over cylindrical tubes. Also from the visualization studies performed by few of the researchers it was seen that the sharp corners and rewetting phenomenon were partially responsible for the overall heat transfer performance enhancements of the modified surfaces.

Author / Year	*Material / Working Fluid*	*Diameter* (mm) / *Length* (mm)	*Enhancement Technique*	*Enhancement Details*	*Heat Flux Range* (kW/m^2)	*Enhance-ment Factor*	*Conclusions and Comments*
Webb and Pais [3] / 1992	Copper / R11, R12, R22, R123, R134a	17.5 and 19.1 / 152.4	Open microchannels / Integral fins Re-entrant cavities	GEWA K26 GEWA TX19, GEWA SE, TURBO-B	3 – 80	1.4 – 2 1.4 – 2	• Heat transfer coefficients increased at a given heat flux with increase in the saturation temperature of the working fluid. • The data for alternate refrigerants was within 10% of the values of the traditional refrigerants for all the tubes. • Refrigerant R11 showed much better performance with TURBO-B tube when compared to any other tubes in their study.
Memory et al. [4] / 1995	Copper / R114, R114 oil mixtures	15.9 / 190	Open microchannels / Integral fins Re-entrant cavities Porous surface	GEWA K19, GEWA K26 GEWA T19, GEWA T26, GEWA YX26, THERMOEX CEL-HE, TURBO-B HIGHFLUX	0.5 – 100	1.7 – 4 2 – 20 3.6 – 18	• Re-entrant cavity tubes showed enhancements of more than 10 times at low heat fluxes and decreased significantly at high heat fluxes. Steady performance drop was observed for all re-entrant cavity tubes and porous layer tubes with increasing heat fluxes. • Enhancements of up to 4 times were recorded for typical low integral-fin tubes. • Higher enhancements observed with re-entrant tubes are due to the higher density of nucleation sites.
Huebner and Kuenstler [5] / 1997	Copper / n-Hexane, Propane	14.55-15.81 / 200	Open microchannels / Integral fins Re-entrant cavities	GEWA K19, GEWA K36 GEWA T19, GEWA TX19, GEWA YX26	2 – 30	1.6 2.4 – 4	• Compared to plain tubes, integral fins showed improved performance but the T-shaped and Y-shaped fins showed even better performance. • T-shaped and Y-shaped have best performance at intermediate heat fluxes. At higher heat fluxes their performance augmentation is reduced.

Author / Year	***Material / Working Fluid***	***Diameter* (mm) / *Length* (mm)**	***Enhancement Technique***	***Enhancement Details***	***Heat Flux Range* (kW/m^2)**	***Enhance-ment Factor***	***Conclusions and Comments***
Tatara and Payvar [6] / 2000	Copper / R134a	19.05 / 211.51	Re-entrant cavities	TURBO-BII-HP	8 – 41	4.9 – 7.9	• An enhancement of 60 – 90% was observed using the Turbo-BII-HP tube over the standard Turbo-B tube with R134a. • They concluded that at elevated heat fluxes, the liquid is unable to replenish the boiling cavities through the narrow mouth opening.
Rajulu et al. [7] / 2004	Brass / Isopropanol, Ethanol, Acetone, Water	33 / 218	Re-entrant cavities	Cavity mouth width: 0.5, 0.4, 0.3, 0.25 and 0.2 mm Cavity depth: 0.5 mm Cavity width: 0.5 mm	11 – 42	1.2 – 2.65	• The enhancement factor for all the tubes increased very slightly with the increase in the heat flux over the given range. • Finned tube (without re-entrant cavities) showed sharper increase in the enhancement factor compared to other re-entrant cavity tubes. • They concluded that the enhancement factor was a stronger function of the number of cavities on the test surface. • Acetone and isopropanol performed well on the tubes having cavity mouth width of 0.3 mm, whereas ethanol and water performed well on the tubes having cavity mouth width of 0.2 mm.
Jung et al. [8] / 2004	Copper / R22, R134a, R125, R32	18.6-18.8 / 152	Open microchannels / Integral fins Re-entrant cavities	Low fin TURBO-B, THERMOEXCEL-E	10 – 80	1.09 – 1.68 1.64 – 8.77	• In their study, THERMOEXCEL-E tube showed the highest heat transfer coefficients. Also re-entrant cavity tubes showed better performance when compared to the microchanneled tubes. • They concluded that the blockage of the cold liquid entering the pores and tunnels by the departing vapor bubbles restricted the high flux performance.

Author / Year	***Material / Working Fluid***	***Diameter* (mm) / *Length* (mm)**	***Enhancement Technique***	***Enhancement Details***	***Heat Flux Range* (kW/m^2)**	***Enhance-ment Factor***	***Conclusions and Comments***
Jung et al. [9] / 2005	Copper / R1270, R290, R600, R600a, RE170	18.6-18.8 / 152	Open microchannels / Integral fins Re-entrant cavities	Low fin TURBO-B, THERMOEX CEL-E	10 – 80	1.2 – 2.4 2 – 9.4	• Their experimental data for flammable refrigerants showed that the heat transfer coefficient increased with increasing vapor pressure. • Enhancements using flammable refrigerants were up to 40% greater than that for the halogenated refrigerants. • They concluded that refrigerants having lower reduced pressures such as dimethylether, iso-butane, and butane took greater advantage of the heat transfer enhancement mechanism than those having higher reduced pressures.
Ribatski and Thome [10] / 2006	Copper / R134a	19.05 / 554	Re-entrant cavities Porous surface	GEWA-B, TURBO-CSL, TURBO-BII HP HIGHFLUX	20 – 70	1.8 – 7 4.9 – 21.3	• They observed a negligible effect of the saturation temperature on the heat transfer coefficient. • At low heat fluxes the HIGHFLUX tubes showed great enhancements but at higher heat fluxes the performance was poor and similar to other tubes.
Ji et al. [11] / 2010	- / R134a	18.50-19.09 / 1088-1100	Open microchannels / Integral fins Re-entrant cavities	Lubricant mass fraction percentage: 0.25, 0.5, 1, 2, 3, 5, 7 and 10	9 – 90	1.6 4	• Re-entrant cavity tubes with narrower mouth widths performed well at lower heat fluxes whereas the tubes with wider mouth widths performed well at higher heat fluxes. • The boiling heat transfer rate increases for fluids up to a lubrication mass fraction of 3%, and thereafter it decreases drastically.

Author / Year	***Material / Working Fluid***	***Diameter* (mm) / *Length* (mm)**	***Enhancement Technique***	***Enhancement Details***	***Heat Flux Range* (kW/m^2)**	***Enhance-ment Factor***	***Conclusions and Comments***
Chien and Webb [12] / 1998	Copper / Methanol	18-19.5 / 140	Re-entrant cavities Pored foil Tube orientation	1575 fins/m (40 fins/in.) Fin height: 0 .8 mm Foil pore diameter: 0.23 mm Foil pore pitch: 1.5 mm over each tunnel	2 – 70	2.5 (approx.)	• Testing was performed in horizontal and vertical orientations. They recorded 10-20% lower heat transfer performance in the vertical orientation compared to the horizontal orientation. • Transparent plastic foil 0.02 mm thick was used for visualization of bubbles and fluid movement in the subsurface tunnels. They observed that 70-90% of the tunnels were filled with vapor. • Testing was also performed with 0.05 mm thick copper foil. Copper covers showed better performance compared to the plastic covers. • They concluded the heat transfer mechanism in the subsurface tunnels was due to the evaporation of the menisci in the corners.
Chien and Webb [13] / 1998	Copper / R11, R123	19.1 / 140	Re-entrant cavities Pored foil	1378 – 1969 fins/m Tunnel width: 0.25 – 0.4 mm Fin height: 0.5 – 1.5 mm	2 – 70	-	• They concluded greater tunnel height and smaller tunnel pitch were preferred for achieving greater heat transfer enhancements. They also concluded that the effect of the fin pitch on the boiling performance wasn't significant. • They also noted that tunnels with sharp rectangular corners showed better performance compared to circular corners because of evaporation of the menisci in the corners at the base.

Author / Year	***Material / Working Fluid***	***Diameter* (mm) / *Length* (mm)**	***Enhancement Technique***	***Enhancement Details***	***Heat Flux Range* (kW/m^2)**	***Enhance-ment Factor***	***Conclusions and Comments***
Chien and Webb [14] / 1998	Copper / R11, R123	19.1 / 140	Re-entrant cavities Pored foil	1378 – 1969 fins/m Foil pore diameter: 0.12, 0.18, 0.23, 0.28 mm Foil pore pitch: 0.75, 1.5, 3.0 mm	2 – 70	-	• They observed dry-out in the tunnels at certain heat fluxes and termed it dry-out heat fluxes (DHF). It was defined as the maximum heat transfer coefficient, which occurred when the liquid in the tunnels was depleted. The DHF limit increased with an increase in the total open area over the heat transfer surface. • The boiling heat transfer rate was observed to decrease as the fin height was reduced. They recommended a fin height of 0.7 – 1.0 mm. They concluded that the boiling performance can be optimized for different working fluids by selecting the proper combination of pore diameter and pore pitch.
Chien and Webb [15] / 2001	Copper / R134a, R22	18.5-19.1 / 140	Re-entrant cavities Pored foil	1575 and 1968 fins/m Fin bases (corner radius): Circular (0.15 – 0.19 mm) Rectangular (0.01 mm)	2 – 80	-	• Sharp rectangular corners at the tunnel base provided better performance over circular bases. R22 yielded 100% greater enhancement with rectangular fins bases compared to circular fin bases. • Higher fin heights, greater fin density, and smaller fin base radius were preferred.

Author / Year	***Material / Working Fluid***	***Diameter* (mm) / *Length* (mm)**	***Enhancement Technique***	***Enhancement Details***	***Heat Flux Range* (kW/m^2)**	***Enhance-ment Factor***	***Conclusions and Comments***
Kim and Choi [16] / 2001	Copper / R11, R123, R134a	18.8 / 170	Re-entrant cavities Pores and connecting gaps	Pore pitch: 0.71 mm over each gap Pore diameter: 0.2, 0.23, 0.27 mm	1 – 50	5 – 6.5	• The maximum heat transfer coefficient for a pore size of 0.27 mm was observed with R134a, whereas pore size 0.23 mm showed better performance with R11 and R123. • They concluded that the connected gaps acted as an additional route for the liquid supply and delayed the dry-outs in the tunnel.
Kulenovic et al. [17] / 2002	Copper / Propane	19 / 115	Re-entrant cavities Structured pores	Pore diameter: 0.01 – 0.5 mm	Up to 100	2 – 3	• Enhanced tubes showed distinct improvements in the heat transfer coefficients especially in the low to medium heat flux ranges. • They concluded that this was due to the deactivation of the re-entrant cavities at high heat fluxes as the vapor could not leave the internal structure fast enough through the small opening.
Chen et al. [18] / 2004	Carbon steel / Propane, Iso-butane	19 /115	Re-entrant cavities Elliptical pores and subsurface tunnels	Elliptical pores: 0.01 – 0.1 mm X 0.15 – 1.5 mm Channel width: 0.05 – 0.2 mm	2 – 30	2 – 4	• They conducted studies to visualize the bubble dynamics using high-speed cameras. • They concluded that the heat transfer enhancements observed where mainly due to the evaporation of the liquid film inside the tunnels.

Author / Year	*Material / Working Fluid*	*Diameter* (mm) / *Length* (mm)	*Enhancement Technique*	*Enhancement Details*	*Heat Flux Range* (kW/m^2)	*Enhance-ment Factor*	*Conclusions and Comments*
Chien and Huang [19] / 2009	Copper / R134a	19 / 100	Re-entrant cavities Wire mesh	1067 – 1524 fins/m Fin height: 0.2 – 0.4 mm Mesh size: 80, 100, 120 meshes/inch Mesh material: Brass and Copper	Up to 55	7 – 8	• In their work, they wrapped a brass or a copper mesh around a finned tube and observed enhanced boiling heat transfer performance. • Good performance was observed on a tube with 0.4 mm fin height wrapped with a size 100 mesh. • They also observed an increase in the heat transfer coefficients with an increase in the fin density and the fin height.
Kotthoff et al. [20] / 2006	Copper / R134a, 2-Propanol, Propane	25.4 / -	Re-entrant cavities Micro and macro cavities	Secondary structure: 0.2 mm X 0.1 mm X 0.05 mm Main structure: Reduced cavity mouth width	Up to 100	1.35 – 1.45	• In their study, they observed circumferential temperature distribution at higher heat fluxes whereas at lower heat fluxes the circumferential temperature was uniform. Higher temperatures were observed on the top of the tube compared to the bottom of the tube. • Developed a new optimized structure for enhancing performance by reducing the cavity mouth width.
Gorenflo et al. [21] / 2010	Copper / R125	25 / - /	Re-entrant cavities Micro and macro cavities	Secondary structure: 0.2 mm X 0.1 mm X 0.05 mm Main structure: Reduced cavity mouth width	Up to 100	-	• They observed that the motion of the fluid around the superheated boundary layer influences and causes a circumferential temperature variation. • In the horizontal orientation the bottom of the tube experienced lower wall superheats compared to the top of the tube. This effect was absent at lower heat flux conditions.

Author / Year	***Material / Working Fluid***	***Diameter* (mm) / *Length* (mm)**	***Enhancement Technique***	***Enhancement Details***	***Heat Flux Range* (kW/m^2)**	***Enhance-ment Factor***	***Conclusions and Comments***
Gorenflo et al.[22] / 2010	Copper / R125	25 / - /	Re-entrant cavities Micro and macro cavities	Secondary structure: 0.2 mm X 0.1 mm X 0.05 mm Main structure: Reduced cavity mouth width	Up to 100	-	• A minimum superheat developed on the lower part of the wall which was related to the additional evaporation into the upward sliding bubbles in close contact with the wall.
Hsieh and Yang [23] / 2001	Copper / R134a, R600a	20 / 210	Porous surface Surface roughness and wrapped helical wire	Polished with emery paper (No. 500). Porous layer deposition method: Plasma spraying of copper or molybdenum. Copper wire 0.1 mm diameter was helically wrapped around the tube. Total 8 different test surfaces were produced.	0.1 – 30	1.2 – 2.3	• They conducted a parametric study of coating thickness, porosity, wrapped helical angle, and wire pitch. The boiling characteristics and bubble dynamics were also studied. • They achieved 2.3 times higher heat transfer coefficients using enhanced surfaces with R600a. • Bubble departure diameter and bubble generation frequency were found to increase linearly with heat flux. • Bubble departure diameter was comparatively smaller in R134a whereas the bubble frequency was lower in R600a. • Photographs qualitatively and quantitatively indicated more active and stable nucleation sites on enhanced surfaces. • They concluded that the nucleation and vaporization took place inside the porous matrix and heat transfer performance was affected by porous layer thickness.

Author / Year	***Material / Working Fluid***	***Diameter* (mm) / *Length* (mm)**	***Enhancement Technique***	***Enhancement Details***	***Heat Flux Range* (kW/m^2)**	***Enhance-ment Factor***	***Conclusions and Comments***
Cieslinski [24] / 2002	Stainless steel / Distilled Water	7.88-23.57 / 250	Porous surface Surface roughness	Porous layer deposition methods: Electrolytic treatment, plasma spraying, gas-flame spraying and modified gas-flame spraying Coating materials: Aluminum, copper, molybdenum, zinc, brass Coatings thicknesses: 0.08 to 2 mm	20 – 1030	2.6 (approx.)	• In their study they observed that boiling commenced at much lower wall superheats of 0.1K. • The heat transfer coefficient decreased with an increase in the heat flux. • Aluminum deposited surfaces showed superior results over other materials. Thickness and porosity of the coating were seen to majorly influence the heat transfer enhancement. Good metallic contact between the porous matrix and the substrate was found to be highly important. • Inverted boiling crisis was observed with porous layer coated surfaces. • For some coated surfaces strong hysteresis phenomenon was also observed over the entire nucleate boiling regime.
Kim et al. [25] / 2002	Platinum / FC72	0.39 / 40	Porous surface	DOM (0.008 mm - 0.012 mm synthetic Diamond particles / Omegabond 101 epoxy binder / Methyl-ethyl-keytone carrier) microporous coating.	Up to 400	6 (approx.)	• They performed measurements of bubble size, frequency, and vapor flow rate from a plain and microporous coated platinum wire. • Results showed microporous coating augmented the nucleate boiling performance through increased latent heat transfer at low heat fluxes and through convective heat transfer at high heat fluxes. • They also observed some extension in the critical heat flux limit with the application of the microporous layer.

Author / Year	***Material / Working Fluid***	***Diameter* (mm) / *Length* (mm)**	***Enhancement Technique***	***Enhancement Details***	***Heat Flux Range* (kW/m^2)**	***Enhance-ment Factor***	***Conclusions and Comments***
Dominiczak and Cieslinski [26] / 2008	Stainless steel / Distilled Water, R141b	8.15-23.60 / 250	Porous surface	The application of the coating was applied only on top $1/3^{rd}$ of the tube surface. Coating material: Aluminum	0.1 – 100	-	• They conducted a study to reduce the effect of circumferential temperature distribution while boiling over a horizontally oriented tube. • In case of smooth tubes the maximum and minimum temperatures were observed in the upper and the lower regions of the tube. They observed up to 4 K difference between the maximum and the minimum temperatures. • In their work they observed higher temperature differences with larger diameter tubes. • They concluded that the porous layer coating aided in alleviating and smoothing the circumferential temperature distribution. They also concluded that the porous layer also reduced the average wall temperature.
McNeil et al. [27] / 2002	Copper alloy (90Cu:10 Ni) / Pentane	19 / 56	Porous surface	HIGHFLUX	10 – 50	5	• In their study, they observed enhancements of up to 5 times with HIGHFLUX tubes.

Author / Year	***Material / Working Fluid***	***Diameter* (mm) / *Length* (mm)**	***Enhancement Technique***	***Enhancement Details***	***Heat Flux Range* (kW/m^2)**	***Enhance-ment Factor***	***Conclusions and Comments***
Ribatski and Jabardo [28] / 2003	Copper, Brass, Stainless steel / R11, R12, R22, R123, R134a	19 / 255	Surface roughness	Average surface roughness was in the range from 0.02 µm to 3.3 µm.	0.6 – 120	-	• They observed higher active nucleation sites on the top surface of the tube compared to the bottom. They concluded that the natural convection might be the responsible for such nucleation behavior. They clearly observed this phenomenon with stainless steel and brass and concluded that the lower thermal conductivity of these materials enhanced the temperature difference between the top and the bottom surface of the tubes. • They concluded that the heat transfer coefficients for higher pressure refrigerants (R12, R22 and R134a) are higher compared to that of lower pressure refrigerants (R11 and R123). • Heat transfer is intensely affected at reduced pressures and surface roughness. • The boiling curve is a function of the surface material and the working fluid combination.
Kang [29] / 2003	Stainless steel / Water	12.7-19.1 / 540	Tube inclination angle	Angles: 0, 15, 30, 45, 60, 75, 90	15 – 90	1.25 – 1.4 (approx.)	• They studied the effects of the inclination angle on the heat transfer performance. • They observed better heat transfer performance at inclinations of 15° and 30° from the horizontal. • They also observed a decrease in bubble slug formation at the bottom of the tube and concluded that the inclination was partially responsible.

Author / Year	***Material / Working Fluid***	***Diameter* (mm) / *Length* (mm)**	***Enhancement Technique***	***Enhancement Details***	***Heat Flux Range* (kW/m^2)**	***Enhance-ment Factor***	***Conclusions and Comments***
Saidi et al. [30] / 1999	Copper / R123	17.1 / 554	Open microchannels / Integral fins	Micro cavity: 1923 fins/m Fin width: 0.4 mm Fin pitch: 0.52 mm Macro cavity: 752 fins/m Fin width: 0.9 mm Fin pitch: 1.33 mm	1.5 – 70	2.2 – 2.4 1.3 – 2.4	• They studied two microchannel geometries and analyzed their boiling heat transfer performance. • They observed a decline in the performance enhancement of the macro cavity geometry tube when compared to the plain tube as the heat flux increased to 70 kW/m^2. • The micro cavity geometry tube showed a steady performance enhancement over the entire heat flux range. • From their results, they concluded that the higher density micro cavity tubes showed comparatively better performance.

Table 2: Comprehensive summary detailing the available literature on the various pool boiling heat transfer enhancement techniques over cylindrical surfaces

3. Objectives

The literature review shows that microchannel enhancement is the only surface modification technique that resulted in significant enhancement in heat transfer performance at high heat fluxes. The objective of this work was thus set to develop high performance microchannel surfaces over cylindrical tubes to efficiently transfer or remove large quantities of heat during pool boiling of water. In order to develop these enhanced microchannel surfaces, a systematic experimental study analyzing the effects of various microchannel geometric parameters was conducted. The effects of the circumferential and axial microchannel grooves on the cylindrical test tubes were also studied. These test sections were tested in the horizontal and vertical orientation, and their influence on the heat transfer performance was analyzed. In order to evaluate the critical heat flux limits of these modified surfaces, they were to be tested up to very high heat flux conditions.

In many industrial and household pool boiling applications, safe operating conditions are limited by the critical heat flux limit of the surface, thereby reducing the overall efficiency of the system. Large scale production of simple microchanneled tubes for commercial applications is less complex compared to the fabrication of other high performance tube surfaces discussed in literature. Another important objective of this work was to generate clear high-speed videos of bubble nucleation, growth, and departure, from the microchannel surfaces to visualize and analyze the underlying mechanisms during pool boiling over these surfaces.

4. Approach

4.1 Design of Experimental Setup

An experimental setup to perform pool boiling over cylindrical tubular surfaces was designed and fabricated. One of the important design objectives for the experimental setup was to be able to test the tubes in both horizontal and vertical orientations. Water was chosen as the working fluid because of its well-known thermal properties and safety in handling compared to that of any refrigerants. The setup was designed to operate and test at atmospheric pressure and vents were provided for vapor escape. Large windows were incorporated in the setup to allow full visual access to the test section, so as to observe and record the bubble dynamics over the heated surface using high-speed cameras.

A schematic of the experimental setup in the horizontal orientation is shown in Figure 12. This system schematic helps identify some of the key components in the setup. Two power supplies of 3.3 kW and 1.5 kW from TDK-Lambda having independent controls were used to drive the primary and the auxiliary heaters, respectively during the experiments. The primary heater inserted inside the test section tube was used to directly supply heat to the test section. The auxiliary heater was used to maintain the water at a saturation temperature of 100°C, and compensate for any heat losses to the surrounding from the experimental setup. The heaters used in the setup were FIREROD® cartridge heaters from Watlow®. The highest heat output per unit area cartridge heater commercially available was selected as the primary heater. This heater was rated for 400 W at 120 V whereas a lower power auxiliary heater was rated for 200 W at 120 V. To achieve the desired heat fluxes the primary heater was operated at 190 V to deliver the total power of 1000 W. Since the temperature of the heater was maintained in its operating range it

was possible to push the heater to its limit without observing any failure. The primary heater had a diameter of 9.53 mm and a heated length of 19.05 mm. The schematic also shows the five thermocouple sensors which were used for gathering the temperature data during experimentation. Four of these sensors were located inside the test section and one was immersed in the pool of water was shown in the figure. The details of these sensors are further discussed in Section 4.3.

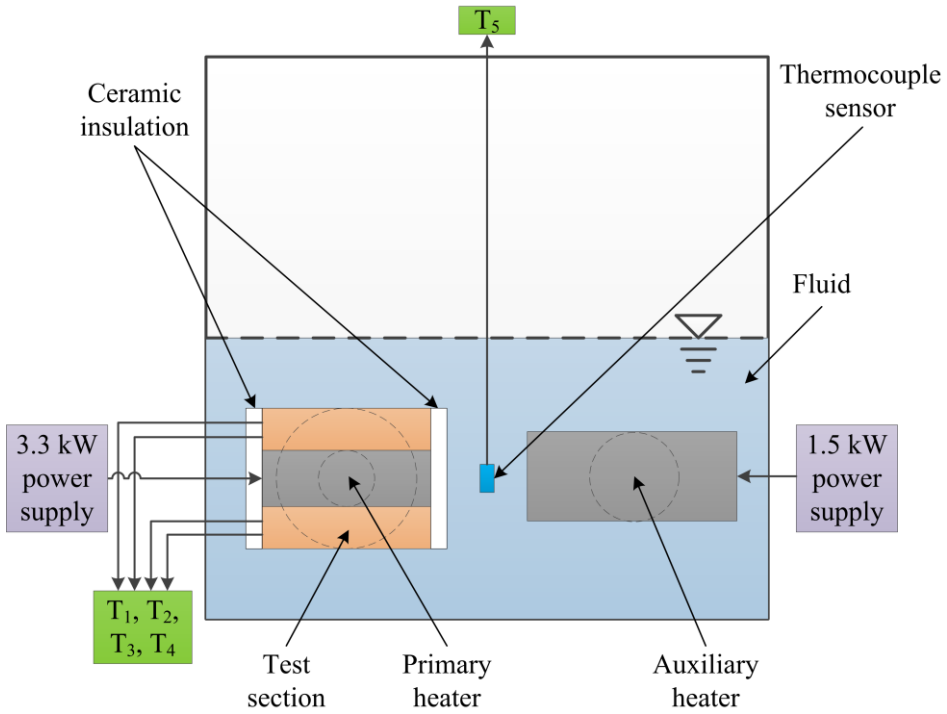

Figure 12: Schematic of the experimental setup in the horizontal orientation

SolidWorks® 3D CAD modeling software was used to model every individual component used in the experimental setup. These parts were assembled within the modeling software to eliminate any dimensional inaccuracies or part interferences while in the design phase. An assembled CAD model of the entire experimental setup is shown in Figure 13. The overall dimensions of the setup were 200 mm × 200 mm × 125 mm. The figure shows the relative position of various components, such as the test section assembly and the auxiliary

heater in its vertical orientation. The experimental setup consists of a central block, windows, compression plates, gaskets, auxiliary heater and the test section assembly. The windows used were 9.5 mm thick, and were made of high temperature resistant borosilicate glass to ensure safety while conducting the experiments, and withstand numerous thermal load cycles. The glass windows were held in place by laterally compressing them against the central block, using the aluminum compression plates and ten M10 fasteners as shown in the figure. Silicone gaskets were used on either side of the glass windows to ensure a leak free setup, and reduce the localized stresses generated during compression of the setup. Technical drawings for these parts were prepared for the purpose of manufacturing. A technical drawing detailing some of the important dimensions for the experimental setup assembly is given in Figure 42 in the Appendix.

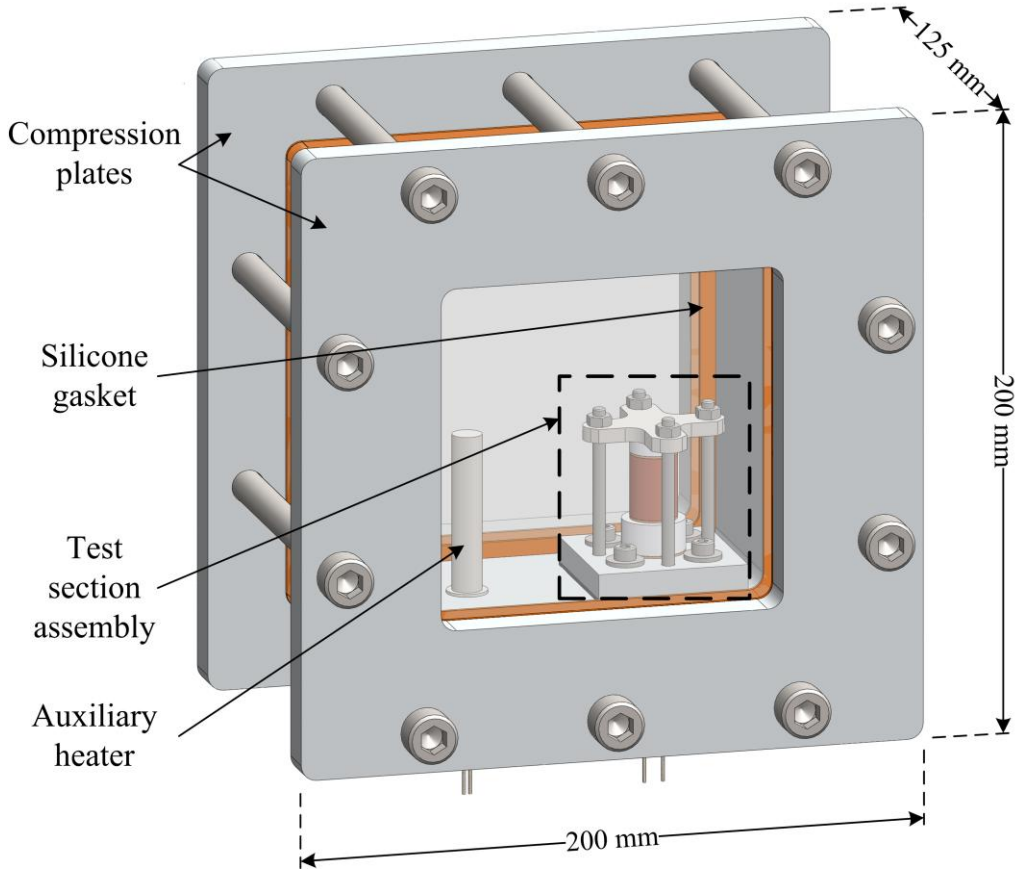

Figure 13: CAD model of the assembled setup in the vertical orientation

The test section was designed keeping in mind the primary heater dimensions so as to maximize heat transfer. Also the test section outer diameter was kept to a minimum so as to increase the highest attainable heat flux values at the outer surface. An exploded view of the test section assembly is shown in Figure 14. The assembly consists of the test section tube, primary heater, thermal insulations, sealing gaskets and holding fixtures. Copper alloy 101, which has a thermal conductivity of 391 W/m·K at 20°C was used to manufacture the test sections. The plain test section was designed to be 20 mm long so as to closely match the 19 mm heated length of the primary heater. The inner and the outer diameter for the test section were accurately machined to 9.53 mm and 15 mm respectively. A technical drawing providing further dimensional details for the plain test section (P0) is given in Figure 43 in the Appendix.

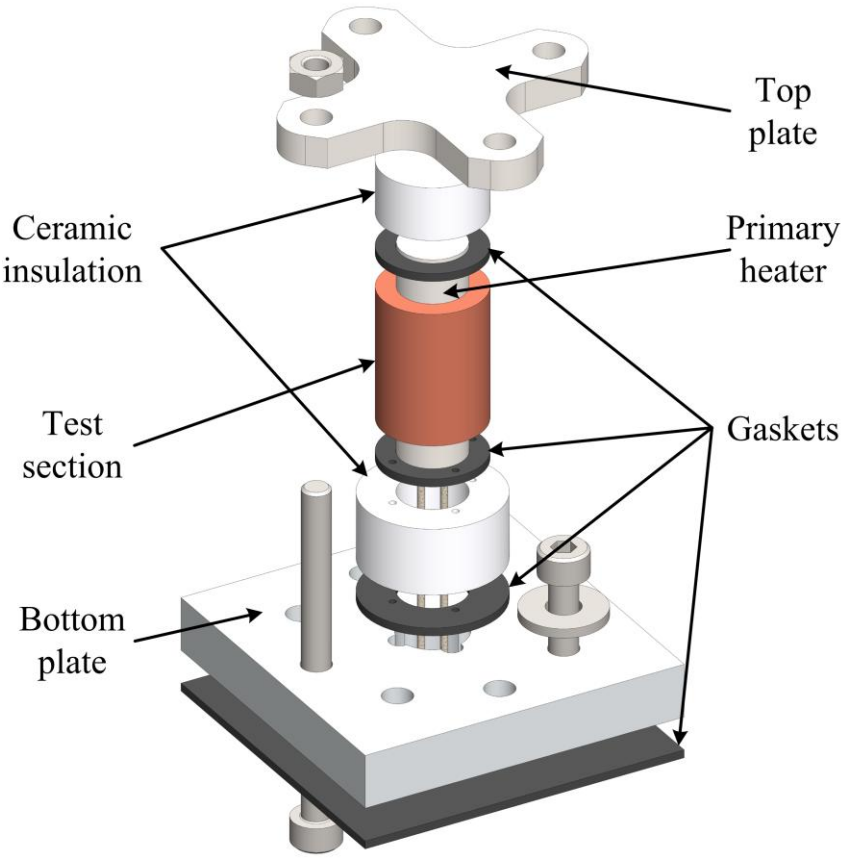

Figure 14: Exploded view of the test section assembly

In the test section assembly, the primary heater was inserted inside the test section tube as shown in Figure 14. In order to improve heat transfer in the radial direction and to ensure good thermal contact, high density polysynthetic silver thermal compound from Artic Silver® was applied between the two. Thermally insulating high temperature ceramic spacers were used on either side of the test section to ensure minimal heat losses in the axial direction. The assembly was axially compressed between the top and bottom aluminum plate using M4 fasteners to hold the test section and the insulating spacers in places as shown in Figure 14. Gaskets were inserted between the components to ensure a leak free setup as shown in the figure. The bottom plate was also used to fasten the test section assembly to the central block of the experimental setup. A technical drawing detailing some of the important dimensions for the test section assembly is given in Figure 44 in the Appendix. All the components required for the experimental setup were machined and assembled using RIT's in-house machine shop facilities and assistance from the machine shop staff.

4.2 Design of Test Surfaces

As discussed earlier, surface modifications are very effectively in passively enhancing the heat transfer performance. In this work, microchannel grooves enhancement technique was employed. The surface of a plain test section described in the previous sub-section was further machined to incorporate the desired microchannel geometry. Twenty dissimilar test sections were designed and fabricated by varying the orientation of the microchannel grooves and dimensions of the geometric parameters. The grooves on the test section surface were oriented either circumferentially or axially as shown in Figure 15. Rectangular and V-groove cross-section geometries were employed for generating these microchannel grooves over the test section surfaces.

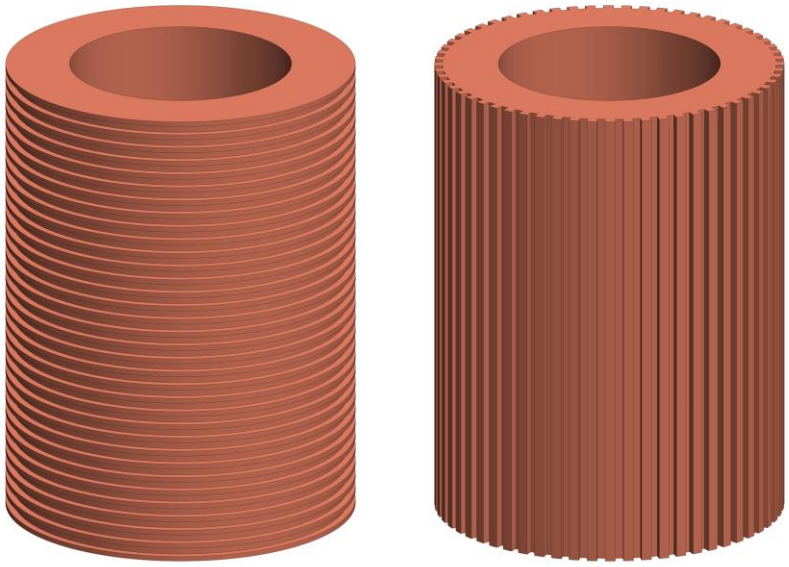

Figure 15: (a) Circumferentially oriented microchannels, (b) Axially oriented microchannels

The circumferentially oriented microchannels with the rectangular cross-section geometry were defined and differentiated by their depth, channel width and fin width as shown in Figure 16(a). The other circumferentially grooved test surfaces consisted of the V-groove cross-section geometries which were defined by their included channel angle, depth and pitch as shown in Figure 16(b). The rectangular cross-section geometry was also used to manufacture the axially oriented microchannels on the test sections. The axially grooved test sections were differentiated based on the depth, width and the angular pitch of the channels as shown in Figure 16(c). These enhanced test sections were broadly categorized into three primary groups, namely, Circumferential Rectangular Microchannels (CRM), Circumferential V-groove Microchannels (CVM) and Axial Rectangular Microchannels (ARM). Eight CRM, six CVM and six ARM test sections were generated to conduct the parametric study, to analyze the effects of geometric

parameters on the heat transfer performance. The dimensional details for the various geometric parameters of the all the different types of test sections are provided in Table 3. Detailed technical drawings for the test sections CRM1, CVM1, and ARM1 are given in Figure 45, Figure 46, and Figure 47, respectively, in the Appendix. Surface modification on the test sections resulted in an increased total wetted surface area. This increase was defined by the area enhancement factor, which is the ratio of the total wetted surface area of the microchannel test section to that of the plain test section at their outer diameters.

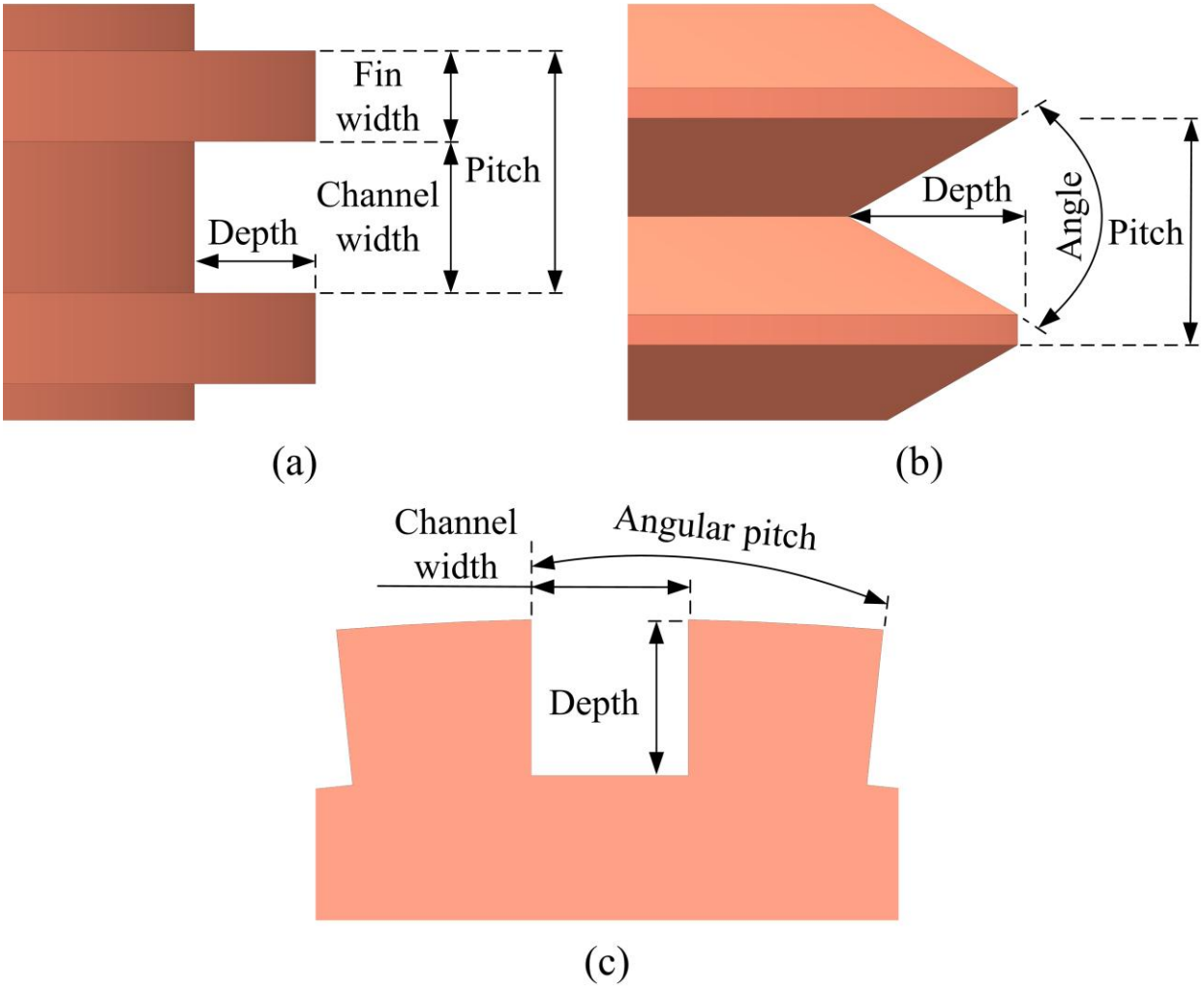

Figure 16: (a) Schematic showing the key geometric parameters required to define the (a) CRM, (b) CVM, and (c) ARM test sections

Test Section	*Depth* (mm)	*Pitch* (mm) / *Angular Pitch* (°)	*Channel Width* (mm)	*Fin Width* (mm)	*Included Angle* (°)	*No. of Channels*	*Wetted Surface Area* (mm^2)	*Area Enhancement Factor*
P0	-	-	-	-	-	-	940	1.00
CRM1	0.29	0.59	0.38	0.21	-	33	1830	1.95
CRM2	0.38	0.59	0.36	0.23	-	33	2050	2.18
CRM3	0.25	0.70	0.38	0.32	-	28	1570	1.67
CRM4	0.41	0.70	0.40	0.30	-	28	1940	2.06
CRM5	0.30	0.50	0.29	0.21	-	39	2000	2.13
CRM6	0.37	0.50	0.28	0.22	-	39	2260	2.40
CRM7	0.26	0.60	0.30	0.30	-	33	1690	1.80
CRM8	0.36	0.59	0.30	0.29	-	33	1990	2.11
CVM1	0.24	0.39	-	-	60	49	1590	1.68
CVM2	0.31	0.55	-	-	60	36	1510	1.60
CVM3	0.37	0.54	-	-	60	36	1640	1.74
CVM4	0.43	0.70	-	-	60	28	1550	1.65
CVM5	0.32	0.40	-	-	45	49	1910	2.03
CVM6	0.46	0.55	-	-	45	36	1910	2.03
ARM1	0.22	6	0.40	-	-	60	1480	1.57
ARM2	0.39	6	0.40	-	-	60	1840	1.95
ARM3	0.22	6	0.52	-	-	60	1470	1.56
ARM4	0.22	8	0.54	-	-	45	1340	1.42
ARM5	0.37	8	0.53	-	-	45	1610	1.71
ARM6	0.51	8	0.53	-	-	45	1830	1.95

Table 3: Dimensional details of geometric parameters for the CRM, CVM and ARM test sections.

These test sections were machined in RIT's machine shop using the Proto TRAK™ CNC lathe and mill to achieve high accuracy in the microchannels dimensions. The manufacturing was carried out with dimensional tolerances as low as ±15 μm. Every test section machined was dimensionally analyzed using a confocal laser scanning microscope from Keyence® to verify the

dimensions of the produced geometries. The investigation showed an average dimensional variation of less than ±10 µm. Figure 17 shows 3D surface profiles generated by the microscope for the circumferentially oriented rectangular and V-groove microchannel test sections.

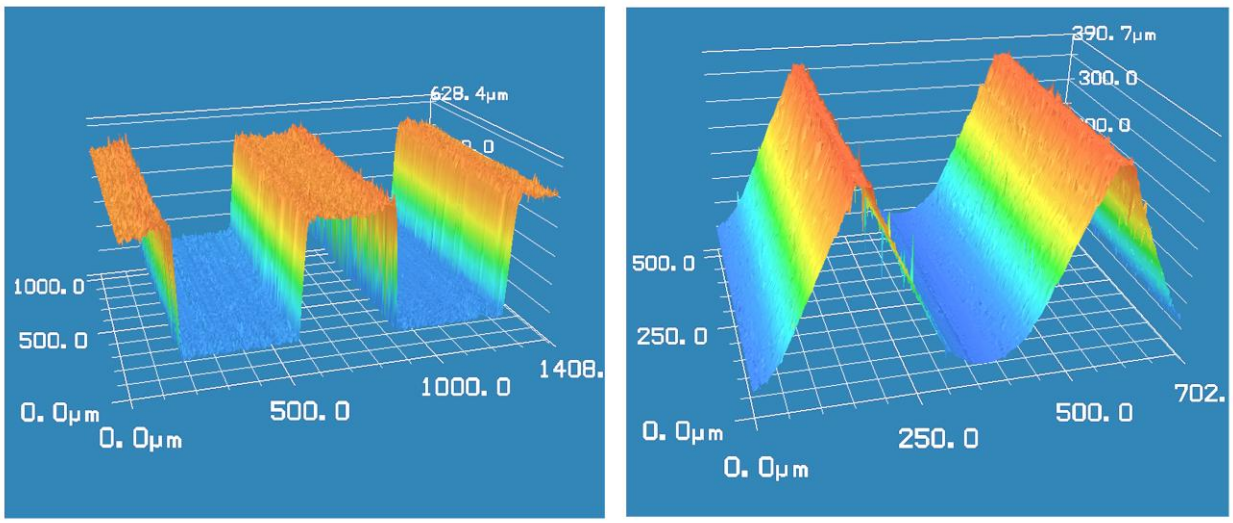

(a) (b)

Figure 17: 3D surface profile of (a) CRM4 and (b) CVM5, test sections generated using a confocal laser scanning microscope

4.3 Data Acquisition

The experimental setup consisted of five thermocouples for measuring the temperatures of the test section and the pool of water while testing. A data acquisition system from National Instruments™ was used to read and record the generated data. Thermocouple input module NI-9213 was used with NI cDAQ-9172 USB chassis to interface with the controller. Five probe style T-type thermocouples from OMEGA® were used for temperature measurement. These thermocouples had a diameter of 0.8 mm and were sheathed and grounded probes. Thermocouples $T_1 - T_4$ were positioned circumferentially at a radial distance of 6 mm and a depth of 10mm inside the test sections. A translucent CAD model showing their approximate

locations is shown in Figure 18. An average temperature inside the test section at a radius of 6 mm was evaluated using the measurements from these thermocouples. The fifth thermocouple T_5 was immersed in the pool of water to measure the bulk fluid temperature while testing.

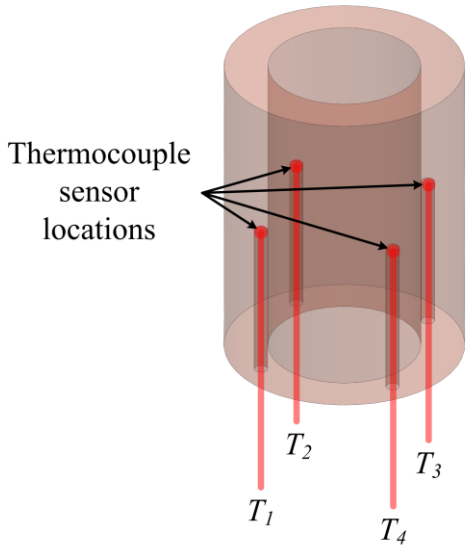

Figure 18: Translucent CAD model of the test section showing the thermocouple locations

A LabVIEW® virtual instrument program was created to read and record the data. This program was also designed to indicate the realization of steady state conditions for the test section and the pool of water while experimentation. Steady state conditions were assumed when the fluctuations in temperature readings from all the thermocouples were continuously within ±0.1°C for a period of at least 10 minutes. The temperature data was recorded at a sampling rate of 5 Hz. The program graphically displayed the temperature data from all the five thermocouples sensors in real-time. The voltage applied across the primary heater and the current supplied were inputted into the program, and were used to evaluate and display in real-time, the heat flux, the wall superheat, and the heat transfer coefficient, derived using the equations described in Section 4.4. A screen shot of the LabVIEW® program developed and used is shown in Figure 19.

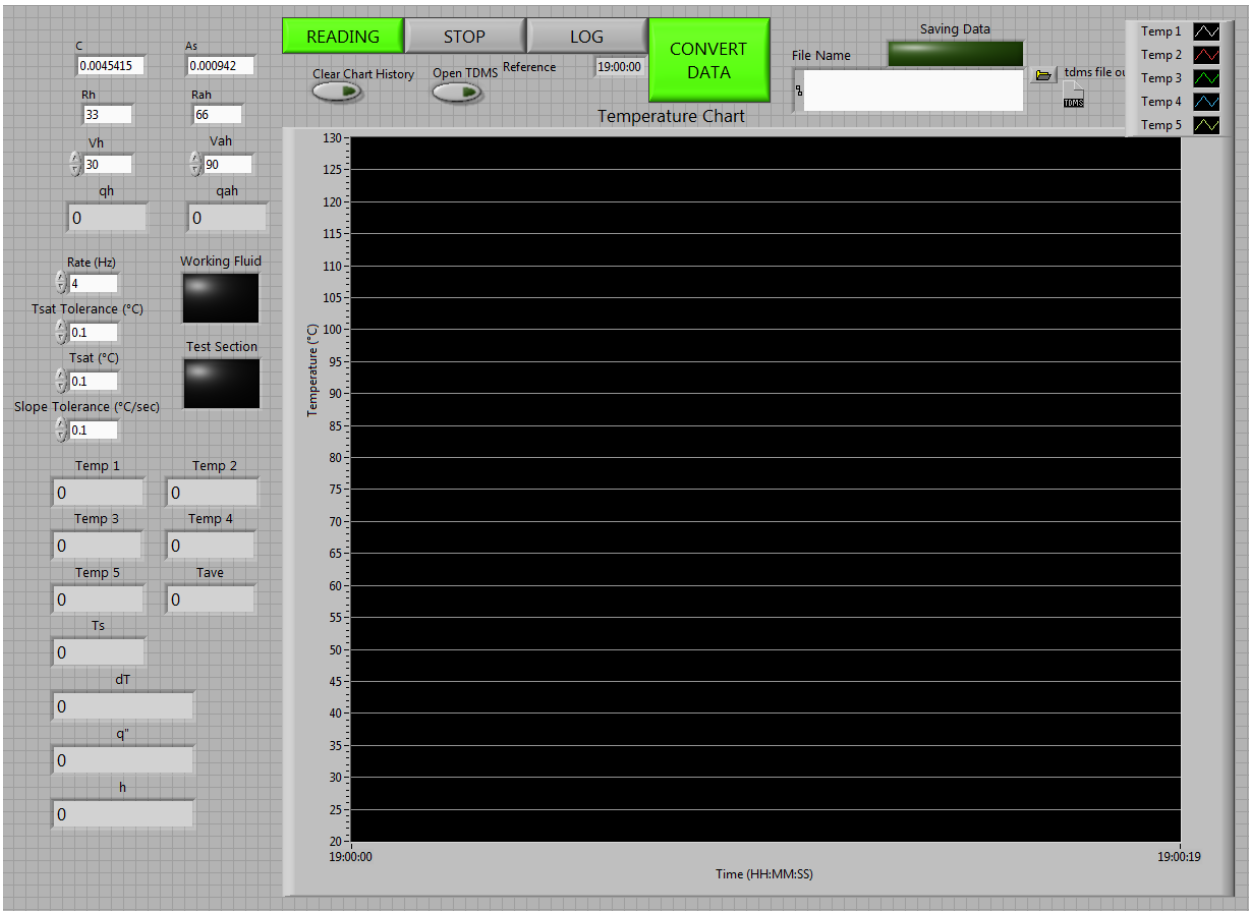

Figure 19: Screenshot of the LabVIEW® program developed for the data acquisition

4.4 Data Reduction

In this section, the various equations used for obtaining the heat transfer coefficient at the outer surface of the test section are given and explained. The heat supplied to the test section was controlled by varying the voltage V applied across the primary heater. The current I supplied to the primary heater was measured at the heater junction and was recorded to determine the total heat imputed q_h to the test section and is given by Equation (1).

$$q_h = V \times I \tag{1}$$

As described in Section 4.2, the test section assembly was designed such that maximum heat supplied was conducted through the test section to the outer wall. The design also incorporated thermally insulating ceramic spacers on the top and the bottom faces of the test section, to reduce the heat losses in the axial direction. In order to account for these minimal heat losses, a computational heat loss study was conducted using the COMSOL Multiphysics® software. The model was computationally solved at every heat flux condition for a given test section to determine the corresponding axial heat losses $q_{a,l}$. Table 4 shows the average percentage heat losses computed at the lowest and highest total heat input q_h conditions for the test section P0 and test section sets of CRM, CVM and ARM in their horizontal and vertical orientations. From this table it was concluded that the total heat losses from the top and the bottom interfaces of the test sections, at high heat flux conditions were negligible. Table 9 in the Section Heat Loss Study Results of the Appendix provides details for the total axial heat losses evaluated in each test section at its lowest and highest total heat input conditions.

Test Section	***Average Percentage Axial Heat Loss***			
	Horizontal Orientation		**Vertical Orientation**	
	At lowest q_h	At highest q_h	At lowest q_h	At highest q_h
P0	2.0 %	0.4 %	1.9 %	0.4 %
CRM	1.9 %	0.2 %	1.8 %	0.2 %
CVM	1.9 %	0.2 %	1.8 %	0.2 %
ARM	1.6 %	0.2 %	1.3 %	0.2 %

Table 4: Average percentage heat loss in the axial direction, at minimum and maximum heat input conditions, for the test sections in the horizontal and vertical orientations

The resultant heat outputted in the radial direction q_r was evaluated using Equation (2). Figure 20(a) shows a cross-section schematic detailing the heat transfer surfaces and their respective directions.

$$q_r = q_h - q_{a,l}$$

(2)

In order to plot the heat transfer performance curves, it was required to evaluate the surface temperature of the test section. The steady state one dimensional radial heat conduction equation for cylindrical cross-section was used for this purpose. The average temperature T_{ave} inside the test section at a radius r_1 as shown in Figure 20(b), was calculated using the temperature readings from the four thermocouples and is given by Equation (3).

$$T_{ave} = \frac{T_1 + T_2 + T_3 + T_4}{4}$$

(3)

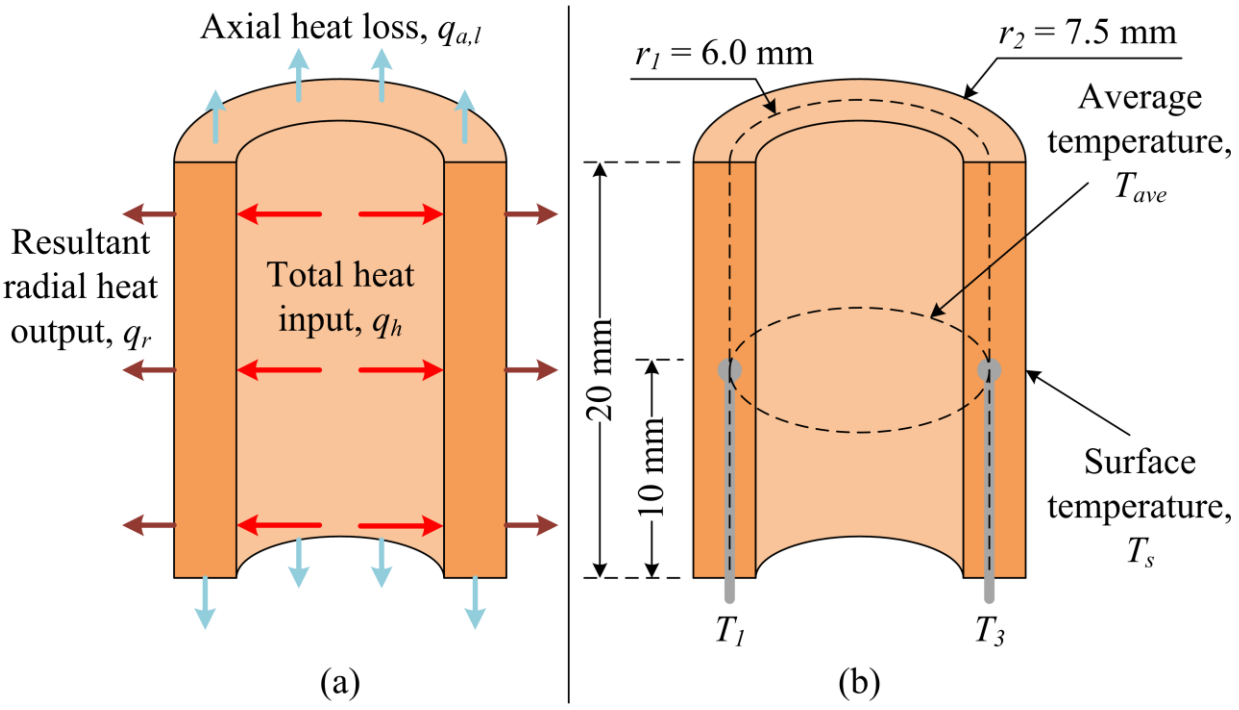

Figure 20: (a) Sketch showing heat input and output surfaces, (b) Sketch indicating the radii for average and surface temperatures, with the thermocouple locations

In the horizontal orientation, circumferential temperature variation was observed around the test section. Slightly higher temperatures were recorded on the top surfaces compared to those recorded on the underside of the tubes. The variation in temperature was negligible at low heat flux conditions, but with an increase in the heat flux the temperature variation between the top and the bottom surfaces of the tubes ranged between 0.5 – 2°C. The temperature readings on the side of the tubes were fairly similar and approximately equal to average of the top and the bottom temperature readings. In order to account for this circumferential temperature variation observed around the tube, the simple average for the temperature recorded inside the test section was calculated as explained above. In the vertical orientation, the circumferential temperature distribution around the tube was absent over the entire heat flux range. Only the nominal fluctuations of ±0.1°C in the temperature readings were observed at the steady state conditions.

The surface temperature T_s was evaluated at the outer radius r_2 as shown in Figure 20(b). As described in Section 4.2, the outer diameter for all the test sections was accurately machined to 15 mm. The surface temperature T_s was determined using the average temperature T_{ave} and the resultant radial heat output q_r, by solving the derived one dimensional radial heat conduction equation as given in Equation (4).

$$T_s = T_{ave} - \left(q_r \times \frac{ln(r_2/r_1)}{2\,\pi\,k\,L} \right) \tag{4}$$

Where,

$$r_1 = 6 \times 10^{-3}\ \text{m} \qquad \text{and} \qquad r_2 = 7.5 \times 10^{-3}\ \text{m}$$

$$k = 391\ \text{W/m} \cdot \text{K} \qquad \text{and} \qquad L = 20 \times 10^{-3}\text{m}$$

The resultant radial heat flux q_r'' over the project surface area A_s at the outer diameter of the test section was evaluated using Equation (5).

$$q_r'' = \frac{q_r}{A_s} \tag{5}$$

The bulk water temperature recorded using the thermocouple sensor T_5 was used to evaluate the wall superheat ΔT as described in Section 1.3. The heat transfer coefficient h at different heat flux conditions was calculated using Equation (6). The reduced data was used to plot the performance curves for the different test sections under various testing conditions.

$$h = \frac{q_r''}{(T_s - T_5)} \tag{6}$$

4.5 Uncertainty Analysis

A small percentage of uncertainty is always associated with any experimentally retrieved parameter. In this section the details of the uncertainties in the various experimentally obtained parameters and the derived parameters are presented. An uncertainty analysis was carefully performed by considering the propagation of errors from these parameters into the final results. An estimate of the total uncertainty that was evaluated in the final results for the different test sections are also presented in this section.

The experimental uncertainty value for temperature measurement at a point using a T-type thermocouple was estimated to be ±0.1°C after careful calibration at different temperatures under steady state conditions. Uncertainties in the geometric parameters were small, since tight

tolerances were used while manufacturing. An uncertainty in the total heat supplied from the power supply was estimated to ±0.1 % using the power supply calibration data. The uncertainty in the thermal conductivity of copper alloy 101 for the given operating temperature range was estimated to be ±1 %. The method of partial sums was employed to calculate the uncertainties in the various derived parameters. Equation (7) gives the general equation used to determine the uncertainty, U_p in any derived parameter and U_{a_i}, represents the uncertainties in all the experimentally measured parameters.

$$U_p = \sqrt{\sum_{i=1}^{n} \left(\frac{\partial p}{\partial a_i} u_{a_i}\right)^2} \tag{7}$$

The equation for uncertainty in the surface temperature at the outer diameter of the test section was derived from Equation (4) and is given by Equation (8). The evaluated percentage uncertainty in the surface temperature for all the test sections at different heat flux conditions was in close proximity of ±0.61%. Similarly, Equation (9) was used to evaluate the percentage uncertainty in the resultant radial heat flux at the test sections outer diameter. An uncertainty of ±0.72% was calculated in the resultant radial heat flux.

$$\frac{U_{T_s}}{T_s} = \left[\left(\frac{U_{T_{ave}}}{T_{ave}}\right)^2 + \frac{1}{2\,\pi} \cdot \left\{\left(\frac{U_{q_r}}{q_r}\right)^2 + \left(\frac{U_{\left(\frac{r_2}{r_1}\right)}}{\left(\frac{r_2}{r_1}\right) \times ln\left(\frac{r_2}{r_1}\right)}\right)^2 + \left(\frac{U_k}{k}\right)^2 + \left(\frac{U_L}{L}\right)^2\right\}\right]^{1/2} \tag{8}$$

$$\frac{U_{q_r''}}{q_r''} = \left[\left(\frac{U_{q_r}}{q_r}\right)^2 + \left(\frac{U_{r_2}}{r_2}\right)^2 + \left(\frac{U_L}{L}\right)^2\right]^{1/2}$$

(9)

The equation for the heat transfer coefficient was used to derive its uncertainty equation and is given by Equation (10). The various uncertainty equations along with the comprehensive derivations for Equation (8), Equation (9) and Equation (10) are given in the Uncertainty Analysis: Equations and Derivations of the Appendix.

$$\frac{U_h}{h} = \Bigg[\left(\frac{U_{q_r}}{q_r}\right)^2 + \left(\frac{U_{r_2}}{r_2}\right)^2 + \left(\frac{U_L}{L}\right)^2 + \frac{(T_s)^2}{(T_s - T_5)^2} \cdot \left\{\left(\frac{U_{T_{ave}}}{T_{ave}}\right)^2 + \frac{1}{2\,\pi} \cdot \left\{\left(\frac{U_{q_r}}{q_r}\right)^2 + \left(\frac{U_{\left(\frac{r_2}{r_1}\right)}}{\left(\frac{r_2}{r_1}\right) \times ln\left(\frac{r_2}{r_1}\right)}\right)^2 + \left(\frac{U_k}{k}\right)^2 + \left(\frac{U_L}{L}\right)^2\right\}\right\} + \left(\frac{U_{T_5}}{T_s - T_5}\right)^2\Bigg]^{1/2}$$

(10)

The uncertainty calculations for the heat transfer coefficients showed a reduction in the percentage uncertainty in the range from low to high heat fluxes. The uncertainties in the heat transfer coefficients in the horizontal and vertical orientation for different test sections at their respective highest heat flux conditions are detailed in Table 5. The uncertainties in the heat

transfer coefficients were in an acceptable range, since the performance was mainly evaluated at high heat flux conditions, where the errors were relatively small.

Test Section	*Uncertainty in Heat Transfer Coefficients h at maximum q''_r*			
	Horizontal Orientation		**Vertical Orientation**	
	$kW/m^2 \cdot K$	%	$kW/m^2 \cdot K$	%
P0	1.55	4.1	1.41	4.0
CRM1	6.20	6.3	5.89	6.2
CRM2	6.33	6.3	5.21	5.8
CRM3	10.22	7.9	7.43	6.8
CRM4	7.29	6.8	5.32	5.8
CRM5	7.94	7.1	6.83	6.6
CRM6	7.88	7.1	5.57	6.0
CRM7	6.71	6.5	3.92	5.1
CRM8	5.66	6.0	4.85	5.6
CVM1	4.80	5.6	3.63	4.9
CVM2	5.49	6.7	4.79	5.9
CVM3	5.18	5.8	3.79	5.0
CVM4	4.98	5.7	3.92	5.1
CVM5	3.17	4.6	3.43	4.8
CVM6	4.69	5.5	4.39	5.4
ARM1	4.33	5.4	5.22	5.8
ARM2	5.06	5.7	5.94	6.2
ARM3	3.36	4.8	3.77	5.0
ARM4	3.70	5.0	3.99	5.1
ARM5	3.52	4.9	4.76	5.6
ARM6	3.23	4.7	5.05	5.7

Table 5: Uncertainties in the heat transfer coefficients for all the test sections in the horizontal and vertical orientation, at their respective maximum heat flux conditions

4.6 Experimental Procedure

In this section a step by step procedure used for conducting the experiment is described. In order to successfully perform an experiment, the entire setup was assembled with the desired test section and thoroughly inspected for any leaks. Distilled water was used for conducting the experiments to avoid any effects of impurities on the results. Once the setup was leak proof the five thermocouple sensors were inserted in place to read and record the temperature data. For all the test sections, the experiment was first carried out in the horizontal orientation and then in the vertical orientation. The primary and the auxiliary heaters were initially operated at high heat flux conditions to raise the temperature of water to its saturation condition. After reaching the saturation temperature, water was allowed to boil for at least fifteen minutes so as to degas the dissolved gasses present in the water. After boiling the water for 15 – 30 minutes at saturation conditions the experimental setup was ready to commence testing.

The power supplied to the test section heater was adjusted to deliver the desired total heat input to the test section. Once the heat input to the test section was set, the setup was maintained at those conditions until the LabVIEW® program indicated that the test section and the working fluid had attained steady state conditions. The applied voltage across the primary heater and the current supplied were inputted into the program for recording and further calculations. The data was logged for an interval of 20 seconds at a sampling rate of 5 Hz. The voltage across the primary heater was incremented and the same procedure was followed for recording the data at the next heat input condition. The temperature data was only recorded after attaining steady state conditions at the given heat input conditions. These steps are repeated to generate temperature for a given test section over a wide range of heat flux conditions. For safe operation of the setup, the experiments were conducted only up to a radial heat flux of approximately 1100 kW/m^2.

Thereafter the power supplied to the heater was decremented in a similar fashion so as to check for any hysteresis that might be observed in the results. Once the entire experiment was conducted by incrementing and decrementing the heat input to the test section in the horizontal orientation, the setup was re-oriented so as to conduct the experiment for the same test section, but in the vertical orientation. The same procedure was followed and the data generated during the experiments was saved for further processing. A picture of the experimental setup just before commencing testing in the horizontal orientation is shown in Figure 21.

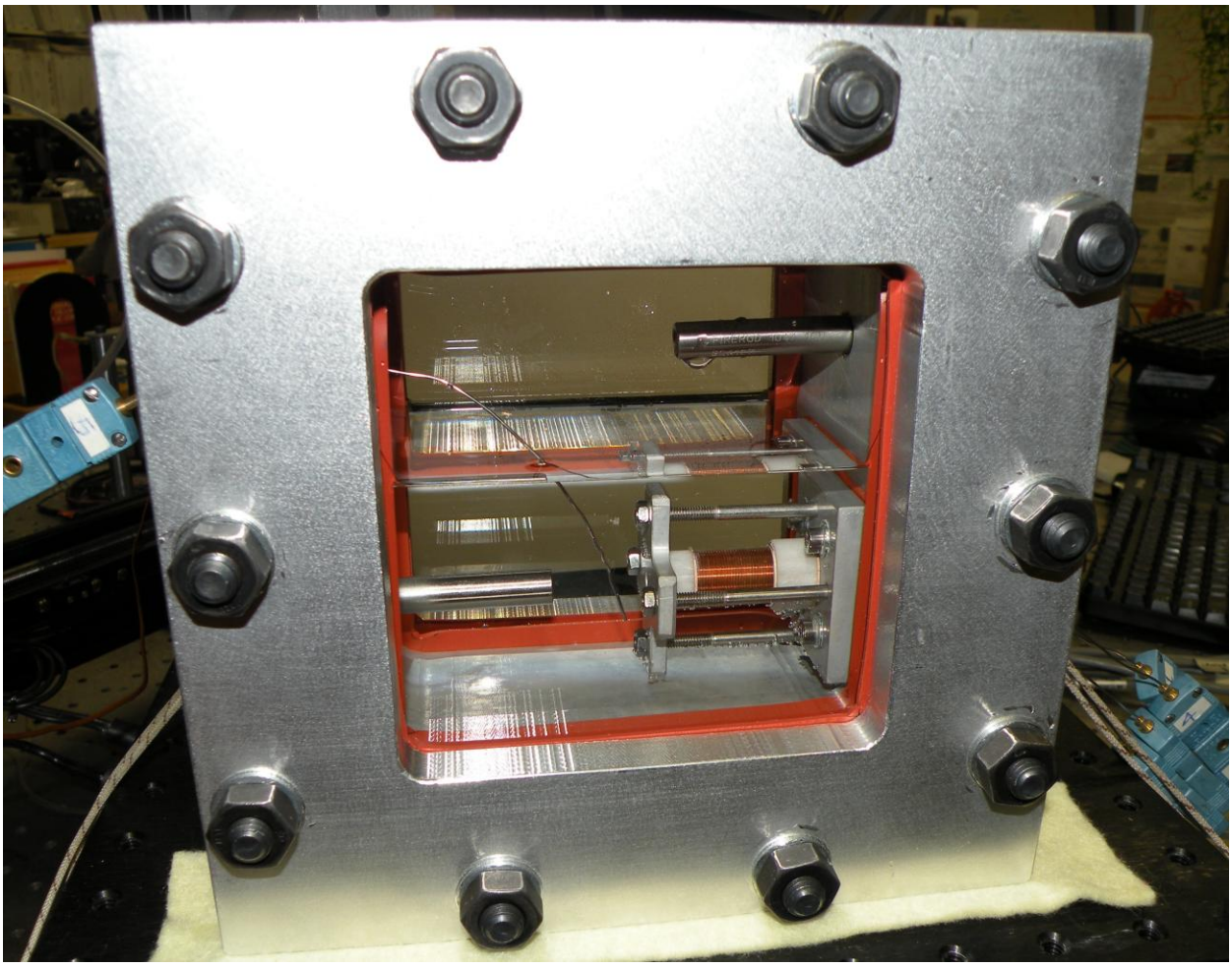

Figure 21: Picture of the assembled experimental setup with the test section in the horizontal orientation

At heat flux above 900 kW/m^2, care was taken while increasing the heat supplied to the test section so as not to exceed the CHF condition for a given surface. Necessary precautions were taken to check for the CHF condition by closely and continuously monitoring the bubble growth and departure mechanism from the test section surface through the large windowed regions while increasing the heat flux. If the CHF condition was reached the power supplied to the primary heater was immediately shut off and sub-cooled water was injected over the test section to break the vapor film encapsulating the heat transfer surface. Under CHF conditions the temperature of the test section spikes to around 400 – 500°C in a few seconds. This was because under the film boiling conditions the heat transfer rates are greatly diminished and the continuous heat input to the test section further raises its temperature. It was important to avoid the CHF condition since it may lead to the failure and destruction of the test section and the experimental setup.

5. Results and Discussions

The testing for twenty microchannel test sections and a plain surface was conducted in this study. Temperature data obtained from the experimentation under different conditions was used to evaluate the heat transfer coefficients for that surface using the various equations described in Section 4.4. All the test sections developed were tested in the horizontal as well as the vertical orientation to study the tube orientation effects on the heat transfer performance. In this section, comprehensive discussions on the results obtained for the CRM, CVM and ARM test sections are presented. The videos of the bubble interactions over the microchannel test sections captured using a high-speed camera are analyzed and discussed below in this section.

5.1 Circumferential Rectangular Microchannels (CRM)

In this sub-section the experimental results for the circumferentially grooved rectangular cross-section microchannels are presented. The heat transfer performance results for eight unique CRM test sections tested are presented in the form of their respective boiling curves. The overall enhancements factors achieved with these surfaces in the heat transfer coefficients are also presented. The effects of the different microchannel geometric parameters for these test sections on the heat transfer performance were analyzed and are discussed below.

5.1.1 Experimental Results and Heat Transfer Performance

The results obtained for the CRM test section surfaces show significant enhancements in the performance compared to a plain surface. The plain test section (P0) was tested only up to a maximum heat flux of 667 kW/m^2, where it attained a wall superheat of 17.8 K and yielded a nominal heat transfer coefficient of just 37.5 kW/m^2·K in the horizontal orientation. The results for the plain surface in the vertical orientation under the same heat flux conditions, were slightly

poorer, and yielded a heat transfer coefficient of 35.5 kW/m^2·K while attaining a wall superheat of 18.8 K. The boiling curves obtained for the plain test section in the horizontal and vertical orientations is shown in Figure 48 in the Appendix. The plain surface reached its critical heat flux limit at an approximate heat flux of 700 kW/m^2, and transitioned into the film boiling regime as described in Section 1.3.4. Hence the testing with P0 was limited to a heat flux of 667 kW/m^2, to ensure safe operation of the experimental setup. Whereas the CRM test sections were successfully tested up to an approximate heat flux of 1100 kW/m^2, and even at such high heat fluxes, none of the CRM test sections reached their CHF limits. The heat flux conditions to which the microchanneled test sections were tested up to, was restricted by the attainable output of the primary heater.

The boiling curves generated for the CRM test sections from the results obtained in the horizontal orientation, are plotted on a graph of heat flux versus the wall superheat and shown in Figure 22. The heat transfer performances of CRM1 – CRM8 are compared to that of P0, revealing the significant enhancements obtained. Test section CRM3 achieved the best overall heat transfer performance in the horizontal orientation. At a heat flux of 1095 kW/m^2, it attained a wall superheat of just 8.5 K and, yielded a heat transfer coefficient of 129.1 kW/m^2·K. This is the highest heat transfer coefficient achieved for pool boiling of water over a modified cylindrical surface from all the literature reviewed in this work. The heat transfer coefficients obtained for the other CRM surfaces were in the range of 94.0 – 111.7 kW/m^2·K, at an approximate heat flux of 1100 kW/m^2. While delivering such high heat transfer performances, these surfaces maintained the wall superheat in the range of 9.6 – 11.5 K.

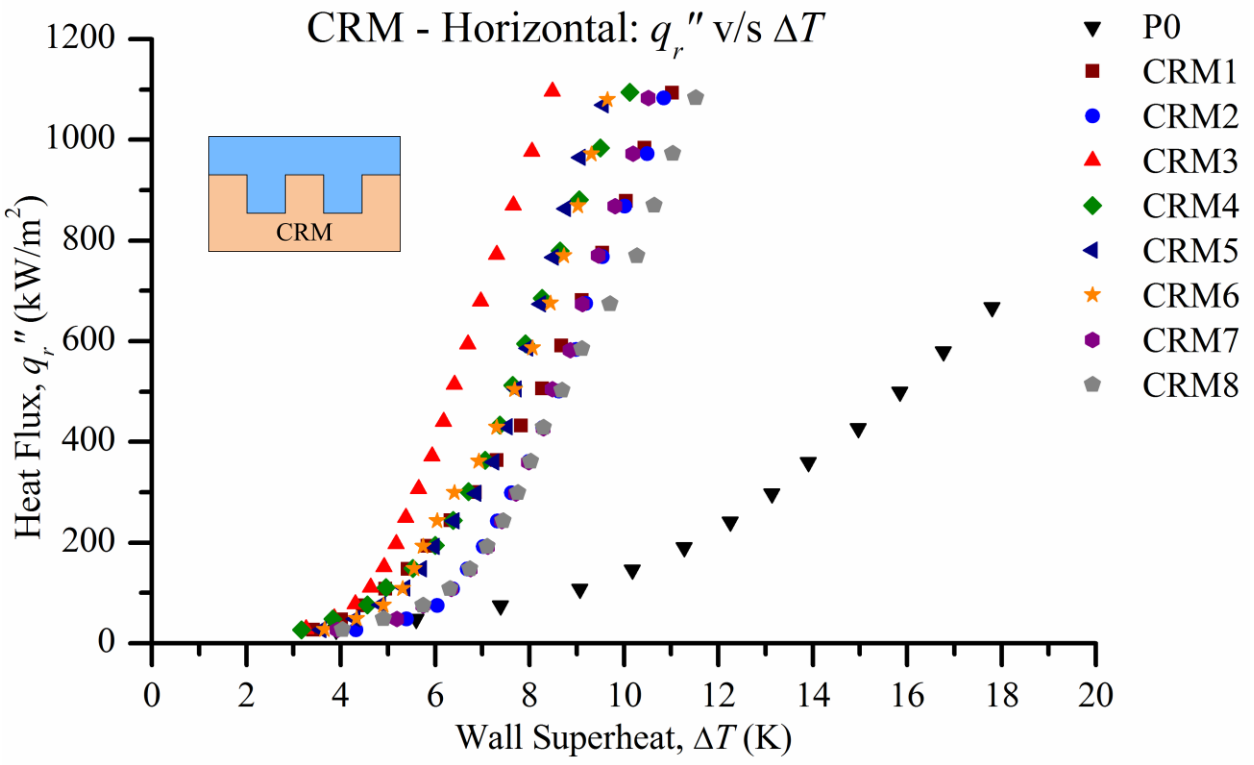

Figure 22: Boiling curves for the CRM test sections in the horizontal orientation

In the vertical orientation also CRM3 outperformed other test sections, delivering a heat transfer coefficient of 109.1 kW/m^2·K at a heat flux of 1093 kW/m^2, while maintaining the wall superheat at 10.0 K. The boiling curves for the experimental results in the vertical orientation are shown in Figure 23. The heat transfer coefficients obtained for other CRM test sections were in the range of 77.3 – 103.2 kW/m^2·K at an approximate heat flux of 1100 kW/m^2. The results obtained for the test sections CRM1 – CRM8, in both orientations are given in Table 6 for further reference. The table details the highest heat flux condition up to which, each test section was tested, and its corresponding wall superheat, and the achieved heat transfer coefficient. Compared to the performance in the horizontal orientation, poorer performance was observed in the vertical orientation and is further discussed in Section 0.

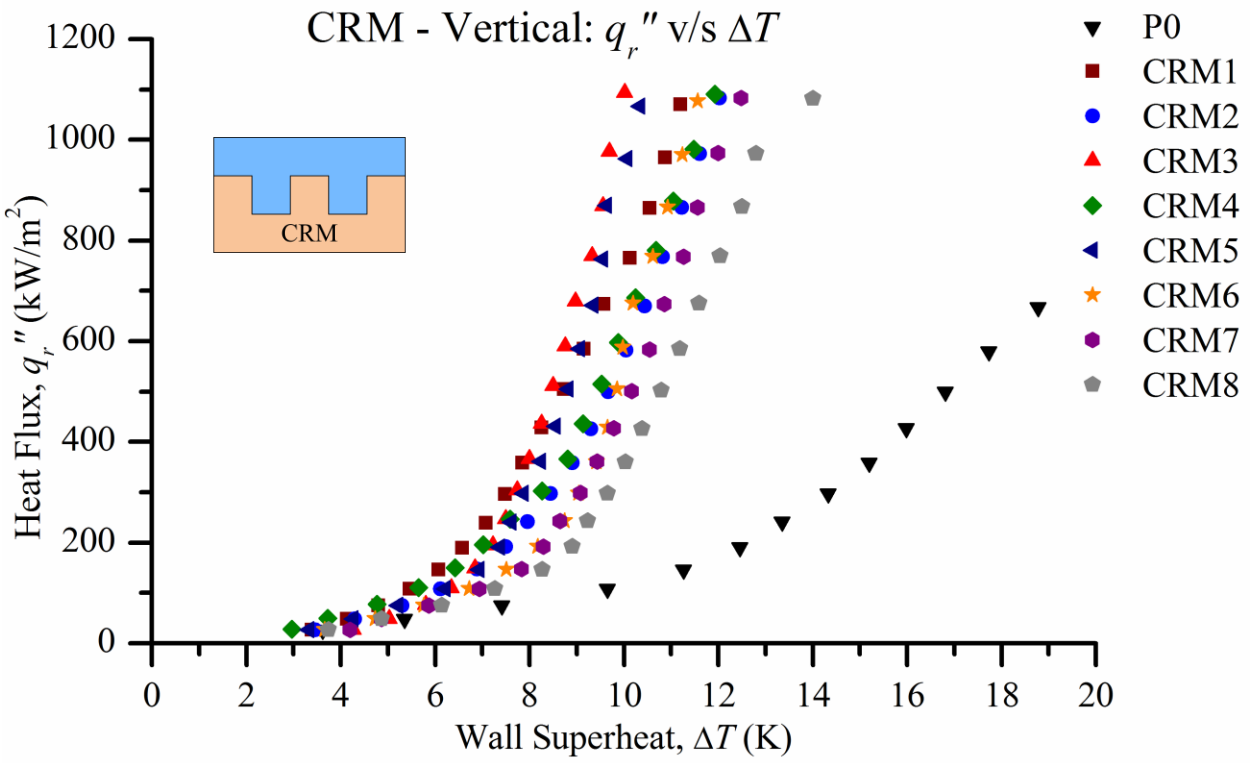

Figure 23: Boiling curves for the CRM test sections in the vertical orientation

Test Section	*Horizontal Orientation*				*Vertical Orientation*			
	q_r'' kW/m^2	ΔT K	h kW/m^2·K	h_{CRM}/h_{P0} -	q_r'' kW/m^2	ΔT K	h kW/m^2·K	h_{CRM}/h_{P0} -
P0	667	17.8	38	-	667	18.8	36	-
CRM1	1093	11.0	99	2.6	1071	11.2	96	2.7
CRM2	1083	10.9	100	2.7	1083	12.0	90	2.5
CRM3	1095	8.5	129	3.4	1093	10.0	109	3.1
CRM4	1095	10.1	108	2.9	1091	11.9	91	2.6
CRM5	1069	9.6	112	3.0	1067	10.3	103	2.9
CRM6	1079	9.7	112	3.0	1077	11.6	93	2.6
CRM7	1083	10.5	103	2.8	1083	12.5	87	2.4
CRM8	1083	11.5	94	2.5	1082	14.0	77	2.2

Table 6: Experimental results for CRM test sections in the horizontal and vertical orientation at their respective highest heat flux conditions

In literature it has been observed that the heat transfer coefficient enhancement factor for most of the re-entrant cavity and porous layer surfaces steeply decreases with an increase in the heat flux condition. The results obtained for the microchannel surfaces in this study, show a steady increase in the heat transfer coefficient with an increase in the heat flux condition. Figure 24 shows a plot of the heat transfer coefficient against the heat flux, and represents the performance of the CRM test sections in the horizontal orientation. At an approximate heat flux of 670 kW/m^2, enhancement factors of 1.9 – 2.6 in the heat transfer coefficients were observed for the CRM surfaces in the horizontal orientation when compared to the performance of the plain test section. The enhancement factors obtained in the vertical orientation were in the range of 1.6 – 2.1, and the vertical orientation plot is given in Figure 49 in the Appendix

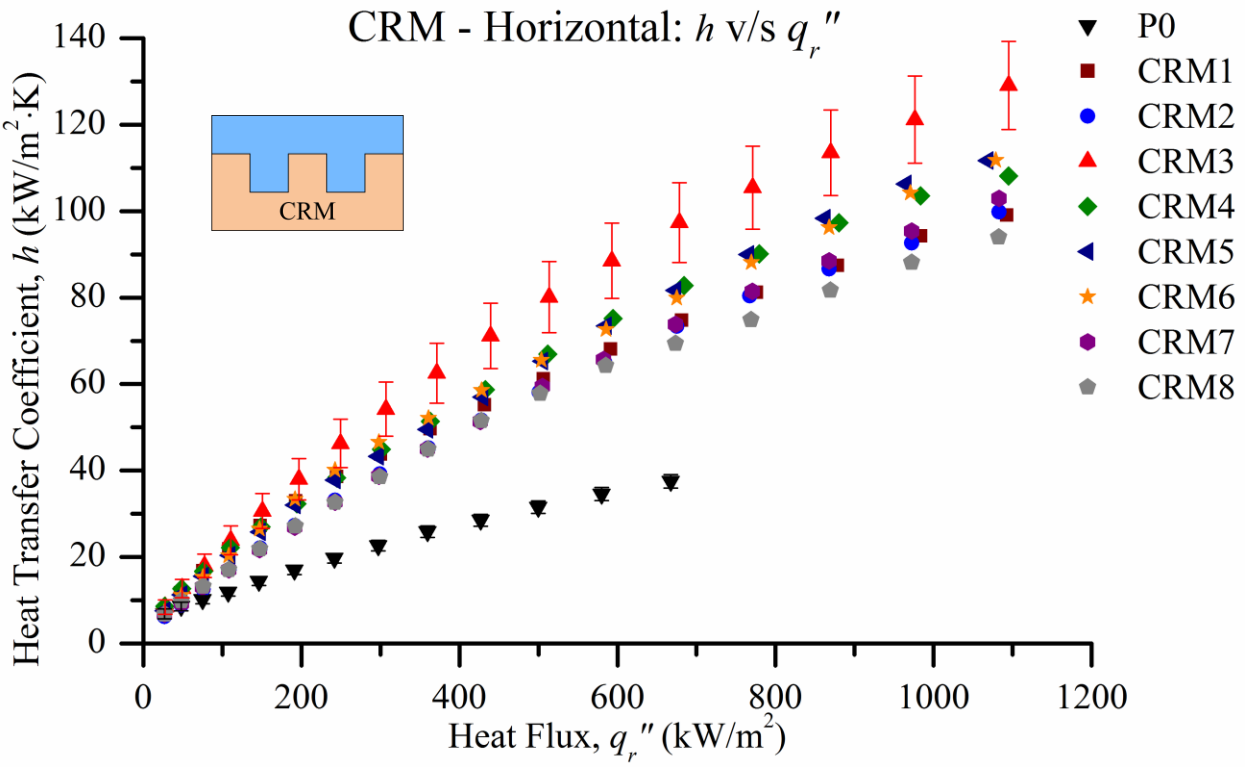

Figure 24: Plot of the heat transfer coefficient against the heat flux, comparing the CRM test section results in the horizontal orientation

The enhancement factors discussed above do not take into account the higher heat flux conditions up to which the CRM surfaces were tested. In order to consider the improvement in the heat flux limits, the overall enhancement factor was defined as the ratio of the heat transfer coefficient of the modified surface to that of the plain surface, but at their respective maximum heat flux conditions. Overall enhancement factors of 2.5 – 3.4 were achieved in the horizontal orientation, whereas in the vertical orientation the enhancement factors were in the range of 2.2 – 3.1. These enhancement factors for individual CRM test sections are detailed in Table 6. Figure 24 also represents the uncertainty observed in the heat transfer coefficients for the plain test section and the best performing CRM3 test section. An estimated uncertainty of ±19.5% was evaluated at the lowest heat flux condition for the CRM3 test section. Whereas at the highest heat flux condition the estimated uncertainty decreases to just ±7.9%. Since the performance of the surface was important at higher heat flux conditions, the estimated uncertainty in the heat transfer coefficient was in an acceptable range. Also noticeable in the figure is the extension of the critical heat flux limit with the use of open microchannels over the cylindrical surface. As mentioned earlier, P0 reached its CHF conditions at an approximate heat flux of 700 kW/m^2, whereas the open microchannel surfaces were successfully tested up to an approximate heat flux of 1100 kW/m^2, without attaining their CHF limits. Hence it is important to the note that the CHF limit was extended by a factor of at least 1.6 over that of a plain surface.

5.1.2 Effects of Microchannel Geometric Parameters

The microchannel geometries on the CRM test sections were designed so as to conduct a parametric study to analyze the effects of channel depth, channel width and fin width on the boiling heat transfer performance. Figure 25 compares the boiling curves of a few CRM test sections to analyze the effects of the microchannel depth on the performance of the surface. The

boiling curves for CRM3 and CRM4 having channel depths of 0.25 mm and 0.41 mm, respectively, are plotted in the figure. Boiling curves for the test sections CRM7 and CRM8 having channel depths of 0.26 mm and 0.36 mm, respectively, are also presented in the figure. All the other dimensions on these two test section pairs were fairly similar and hence a direct comparison between their boiling curves would determine the effects of the channel depth. The heat transfer performance obtained with CRM3 was relatively better than that obtained for CRM4 in both, horizontal and vertical orientations. Similarly the performance obtained with CRM7 was comparatively better than CRM8. Hence it was seen that the circumferentially oriented, rectangular base microchannel geometries with shallower grooves yielded better heat transfer performance compared to deeper grooves.

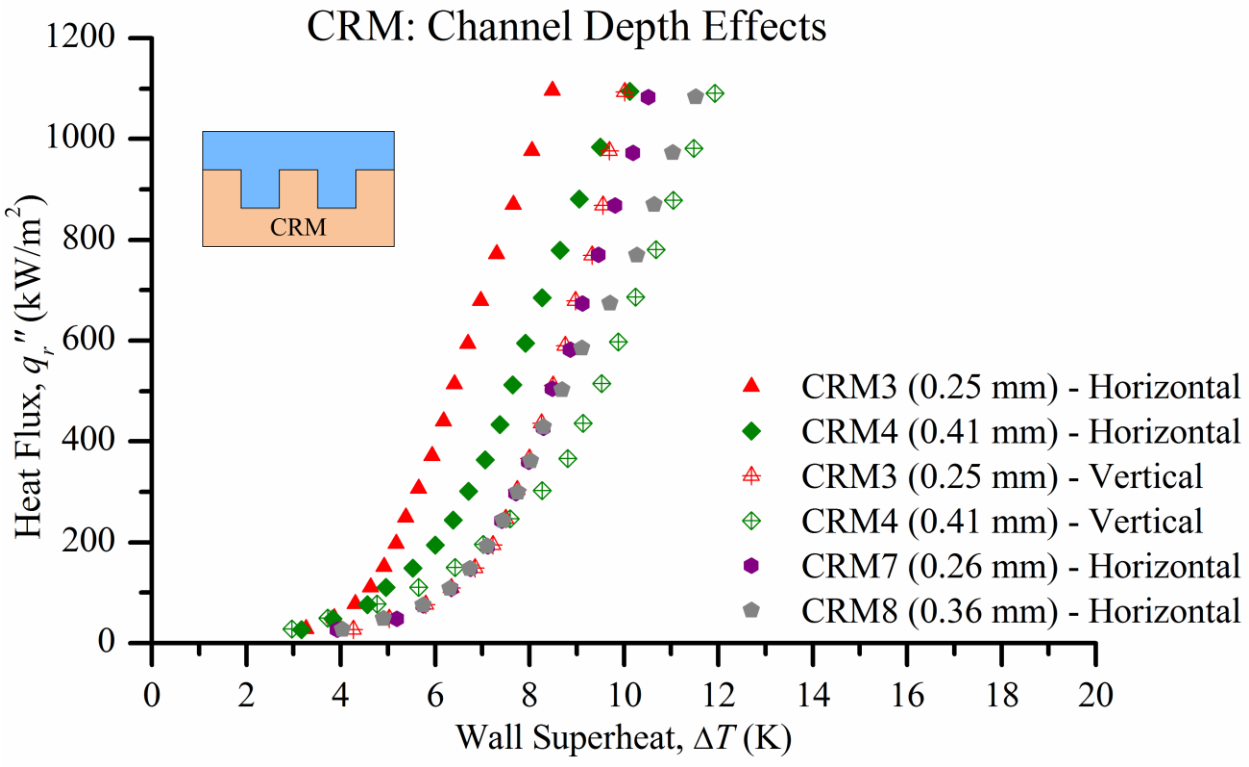

Figure 25: Boiling curve comparison to analyze the effects of the channel depth

The channel width effects for the CRM test section surfaces on the heat transfer performance are discussed using the graph shown in Figure 26. Performance curves for CRM1 and CRM5 having channel widths of 0.38 mm and 0.29 mm, respectively, are presented for comparison. Also presented are the boiling curves for test sections CRM2 and CRM6 having channel widths of 0.36 mm and 0.28 mm, respectively, to analyze the effects if channel width on the heat transfer performance. From these results, it was seen that narrower microchannels showed good enhancements in the heat transfer performance, but their effects were only prominent at higher heat flux conditions as can be seen in the figure.

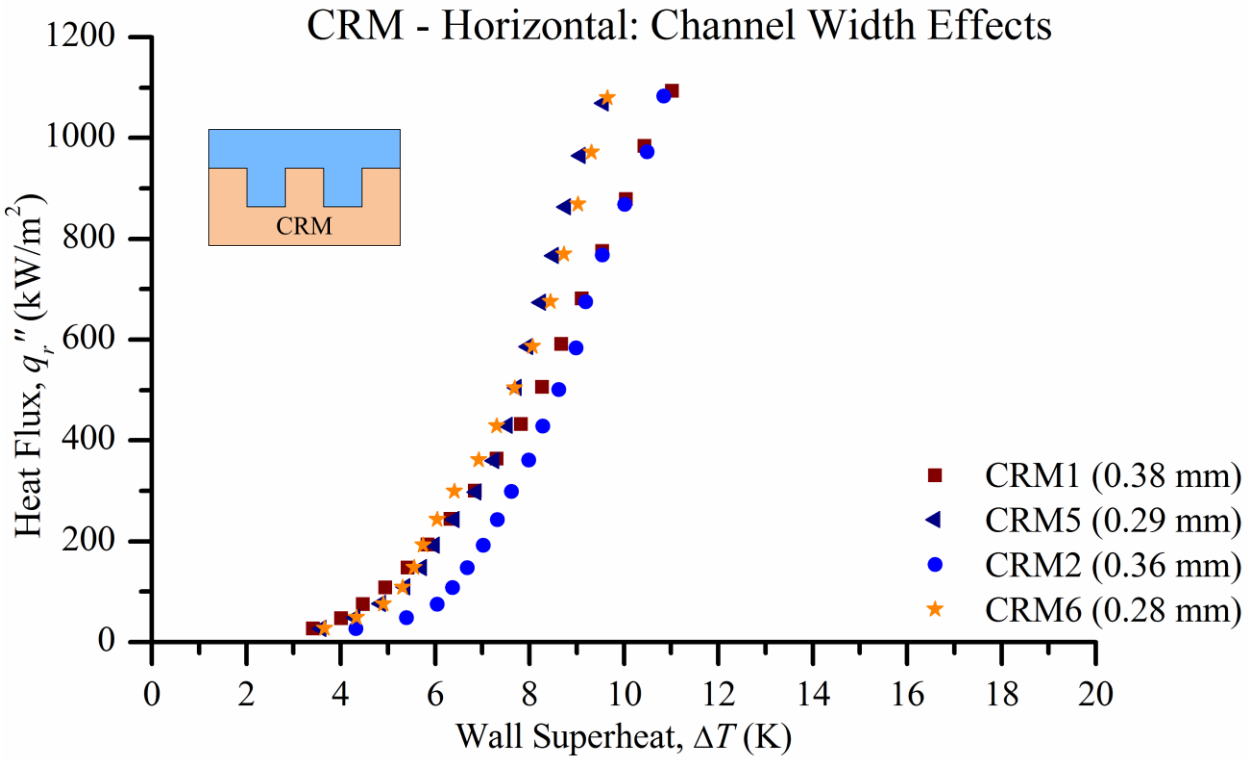

Figure 26: Boiling curve comparison to analyze the effects of the channel width

Figure 18 shows the boiling curves for test sections CRM2 and CRM4 having fin widths of 0.23 mm and 0.3 mm, respectively, to compare and analyze the effects of the fin width on the heat transfer performance. From the results, it was observed that CRM4 microchannels

consisting of slightly wider fins performed better than CRM2. Similar trend was observed with CRM1 and CRM3 having fin widths of 0.21 mm and 0.32 mm, respectively. Their boiling curves in the horizontal and the vertical orientation can be compared using Figure 22 and Figure 23, respectively. This figure also represents the hysteresis observed in the experimental results between the increasing and decreasing heat flux conditions. Small hysteresis was observed for the experiments conducted in the horizontal orientation for all the CRM test sections. However in the vertical orientation the hysteresis observed was negligible.

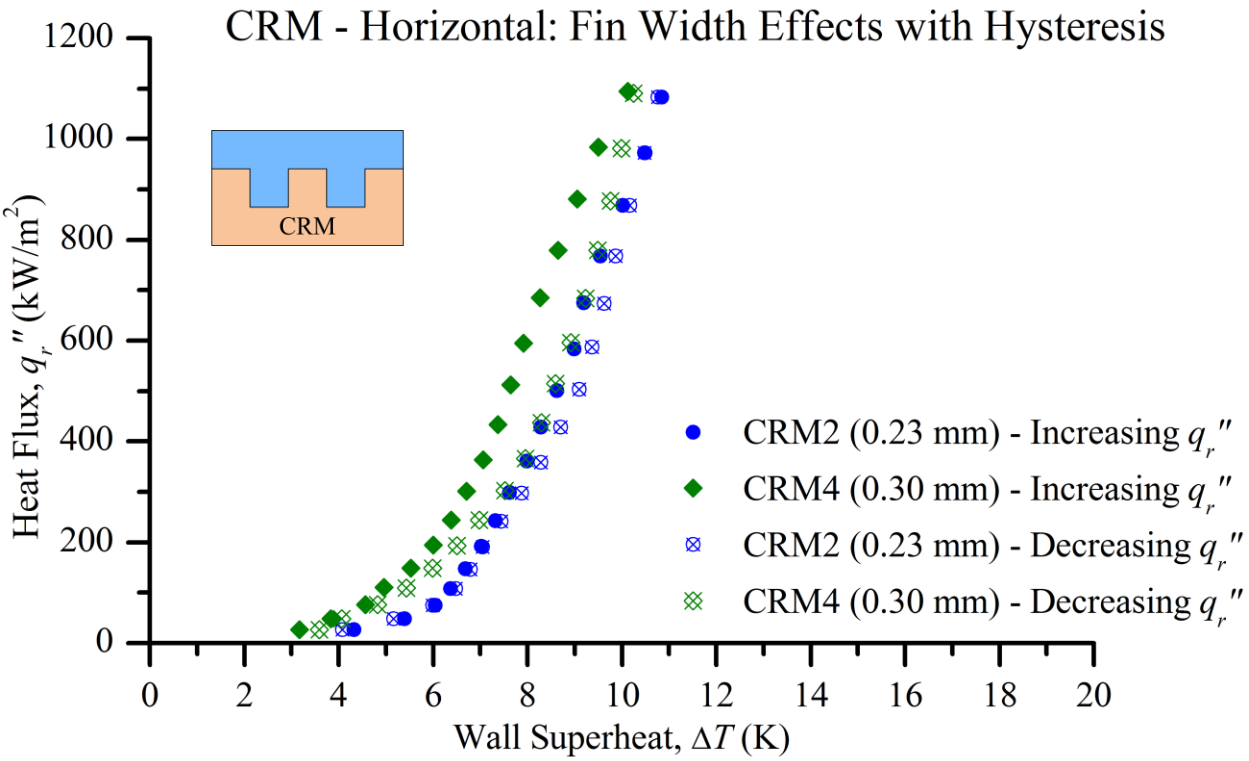

Figure 27: Boiling curve comparison to analyze the effects of the fin width

5.1.3 Area Normalized Heat Transfer Results

The heat fluxes described in all the results presented above were evaluated using the projected surface area at the outer diameter of the test sections. As described in Section 4.2, any modification on the surface has a direct impact on the total wetted surface area. The increase in

this wetted surface area was defined by the area enhancement factor. As seen in literature, number of these studies concentrated on enhancing the available surface area for heat transfer, to ultimately enhance the heat transfer performance. In order to explore the effects of other factors responsible for the better performance, the heat fluxes were recalculated using the total wetted surface area for the CRM test sections. The boiling curves thus obtained for the test sections in the horizontal orientation are given in Figure 28. Even though a large quantity of heat was supplied to the test section, the resulting heat flux at the outer surface was greatly diminished compared to the heat flux discussed earlier. Nevertheless the area normalized results still showed better heat transfer performance compared to the results of the plain surface. Area normalized results for CRM surfaces in the vertical orientation are given in Figure 50 in the Appendix.

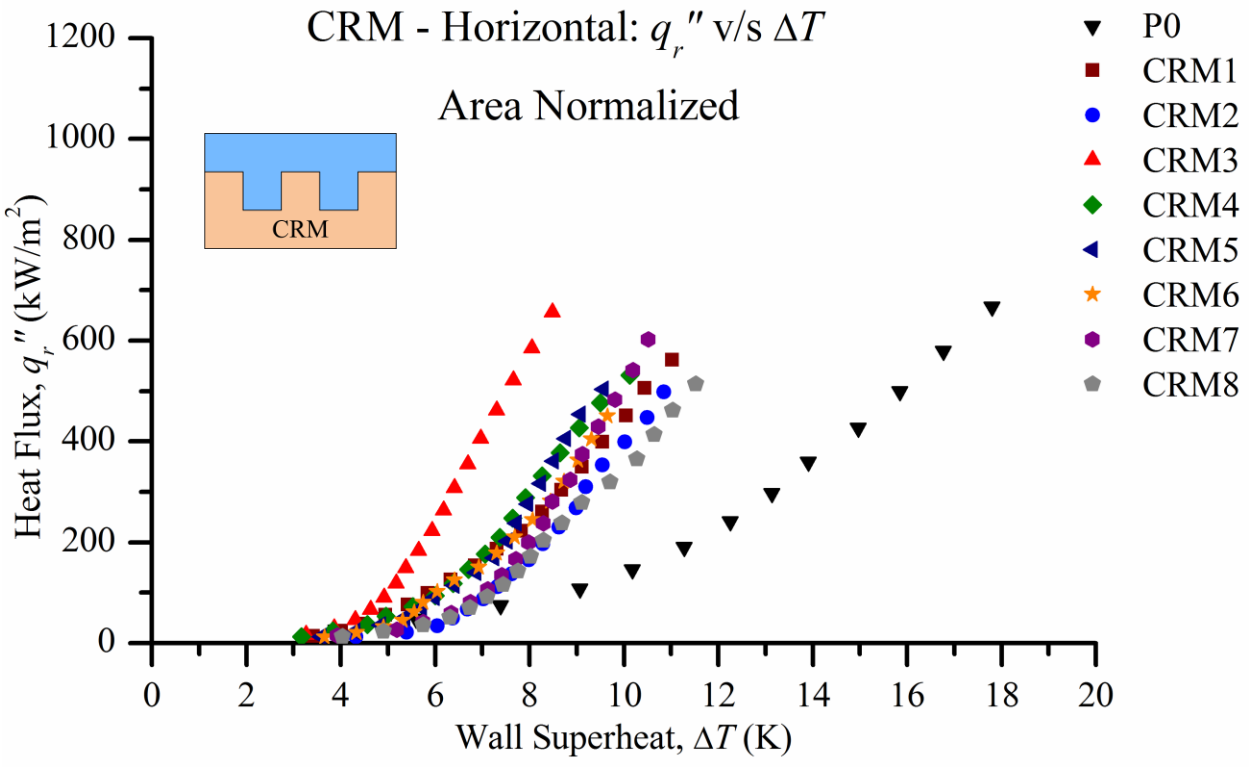

Figure 28: Boiling curves based on area normalized heat fluxes for the CRM test sections in the horizontal orientation

It is important to note that the best performing surface had the smallest area enhancement factor among all the CRM test sections. Thereby showing significant enhancement in performance in-spite of the results being area normalized. From these results it was determined that factors other than surface area augmentation were responsible for the improved performance with microchannel test sections. The microchannel geometry played an important role in enhancing the overall heat transfer performance for these modified surfaces. Cooke and Kandlikar [31, 32] in their studies have analyzed the bubble nucleation and growth over the microchannels on a flat surface, and concluded that the rewetting phenomenon was one of the major factors responsible for the enhancement in performance. The bubble dynamics and the rewetting of the heated surface were studied in detail over the cylindrical surfaces, and are described in Section 5.5 of this work. High-speed videos of bubbles nucleating, growing and departing from the microchannel surface are presented and discussed in that section.

5.2 Circumferential V-groove Microchannels (CVM)

The results for the circumferential V-groove microchannel test sections are presented and discussed in this sub-section. Six CVM test sections were tested to study the enhancements that can be obtained using V-groove microchannel geometries. The generated data was represented in the form of their respective boiling curves. Area normalized results for these test sections are also reported in this section.

5.2.1 Experimental Results and Heat Transfer Performance

The heat transfer performance results in the horizontal orientation for the plain test section and the six CVM test sections are shown in Figure 29. Similarly the vertical orientation performance results are shown Figure 51 in the Appendix for further reference. As described

earlier the test section P0 was tested up to a heat flux of 667 kW/m^2, at which it yielded heat transfer coefficients of 37.5 kW/m^2·K and 35.5 kW/m^2·K in the horizontal and vertical orientations, respectively. The CVM surfaces showed good enhancements in the heat transfer performance over that of the plain surface. Test section CVM2 reached its CHF limit at a heat flux slightly over 900 kW/m^2, in the horizontal orientation. In this entire study, CVM2 was the only modified surface to reach its CHF limit and transition into the film boiling regime. In the vertical orientation, CVM2 was only tested up to an approximate heat flux of 970 kW/m^2 in order to ensure safety while testing. The performance curve obtained for CVM5 in the horizontal orientation was significantly poor compared to the other CVM test sections. It was assumed that the 45° sharp V-groove angle coupled with the small channel pitch, and fairly shallow grooves were responsible for such poor performance over the entire heat flux range.

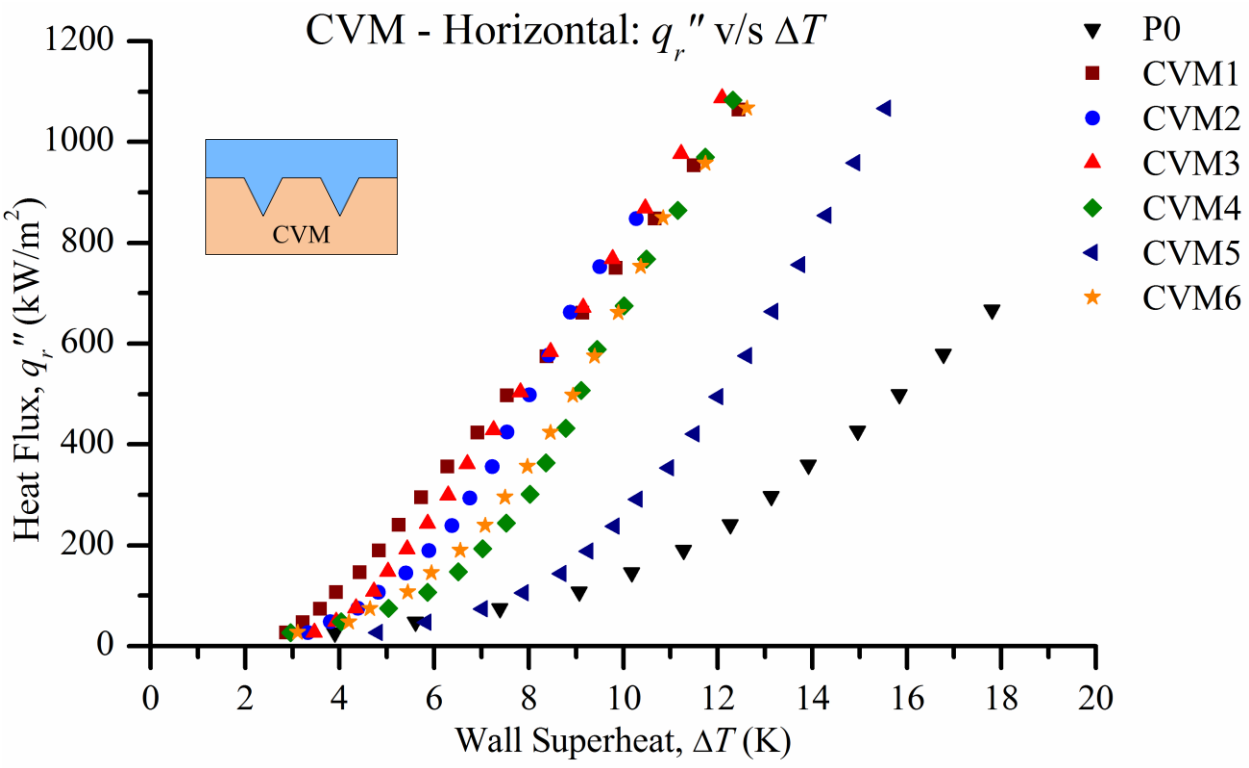

Figure 29: Boiling curves for the CVM test sections in the horizontal orientation

All other CVM test sections were successfully tested up to a heat flux of approximately 1070 kW/m^2. The results for four of the six CVM test sections at higher heat flux conditions produced very similar results. For these test sections heat transfer coefficients in the range of 84.5 – 89.9 kW/m^2·K with the wall superheats in the range of 12.1 – 12.6 K were obtained in the horizontal orientation. Similarly in the vertical orientation, heat transfer coefficients in the range of 73.7 – 81.7 kW/m^2·K with wall superheats in the range of 13.1 – 14.5 K were obtained at an approximate heat flux of 1070 kW/m^2. From these very similar results, it was difficult to factor out the effects of individual geometric parameters on the heat transfer performance. The heat transfer coefficients and the overall enhancement factors achieved for the different CVM test sections at their respective highest heat flux conditions in the horizontal and vertical orientations are detailed in Table 7 for further reference.

Test Section	***Horizontal Orientation***				***Vertical Orientation***			
	q_r'' kW/m^2	ΔT K	h kW/m^2·K	h_{CVM}/h_{P0} -	q_r'' kW/m^2	ΔT K	h kW/m^2·K	h_{CVM}/h_{P0} -
P0	667	17.8	38	-	667	18.8	36	-
CVM1	1065	12.5	86	2.3	1066.2	14.5	74	2.1
CVM2	848	10.3	83	2.2	966.4	11.8	82	2.3
CVM3	1087	12.1	90	2.4	1086.4	14.3	76	2.1
CVM4	1083	12.3	88	2.3	1082.4	14.0	77	2.2
CVM5	1066	15.6	69	1.8	1066.1	14.9	72	2.0
CVM6	1067	12.6	85	2.3	1066.4	13.1	82	2.3

Table 7: Experimental results for CVM test sections in the horizontal and vertical orientation at their respective highest heat flux conditions

A plot of heat transfer coefficient against heat flux, showing the performance of the CVM test sections in the horizontal orientation is given in Figure 30. The overall heat transfer enhancement factors of 1.8 – 2.4 were obtained for the CVM test sections in the horizontal

orientation. The uncertainties in the heat transfer coefficients of test sections CVM3 and P0 are also shown in the figure as error bars. Similarly, vertical orientation results are shown in Figure 52 in the Appendix, and the overall enhancement factors obtained were in the range of 2.0 – 2.3.

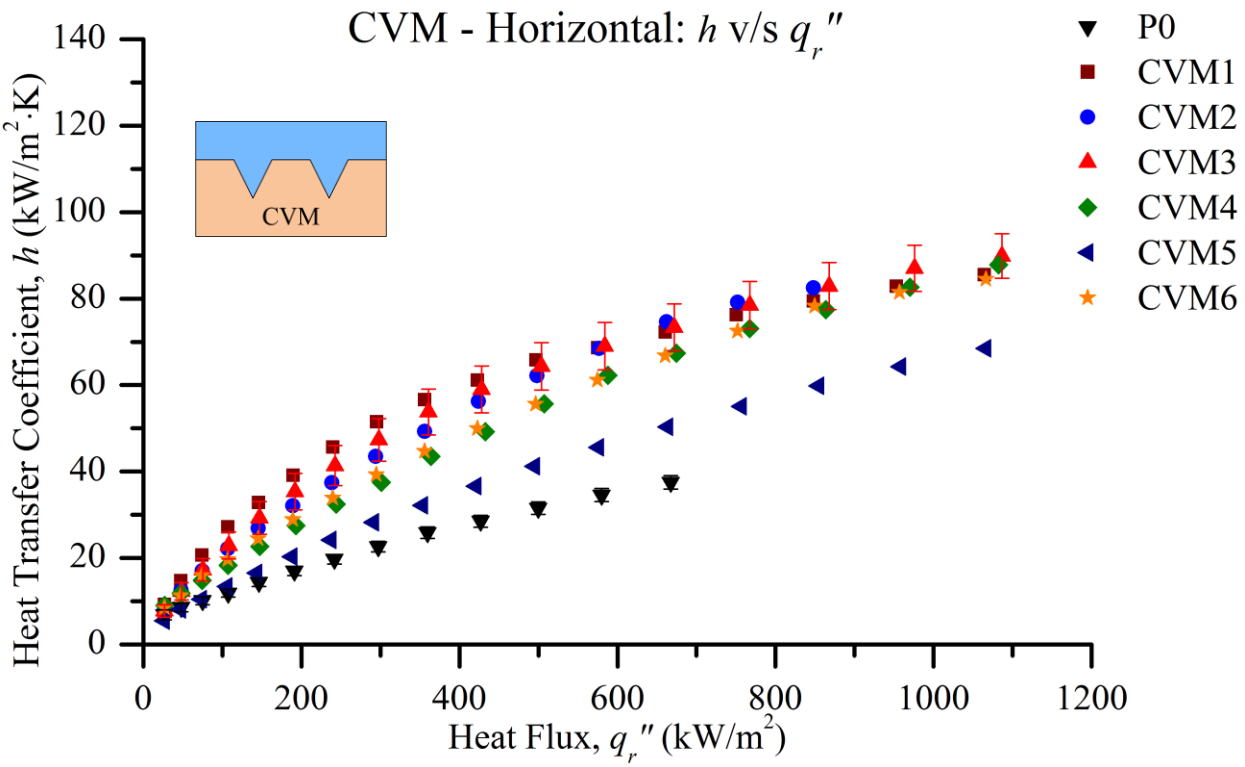

Figure 30: Plot of the heat transfer coefficient against the heat flux, comparing the CVM test section results in the horizontal orientation

5.2.2 Area Normalized Heat Transfer Results

In this sub-section, the area normalized results obtained for the CVM test sections are presented. The area normalized boiling curves for the horizontal orientation experiments are shown in Figure 31. From these heat transfer results it was seen that the performance of the CVM test sections other than CVM5 still showed some enhancements. As discussed earlier, the unique microchannel geometries on each of these surfaces played an important role in enhancing the overall heat transfer performances and were partially responsible for the observed

enhancements. Similarly the area normalized results for these surfaces in the vertical orientation are shown in Figure 53 in the Appendix.

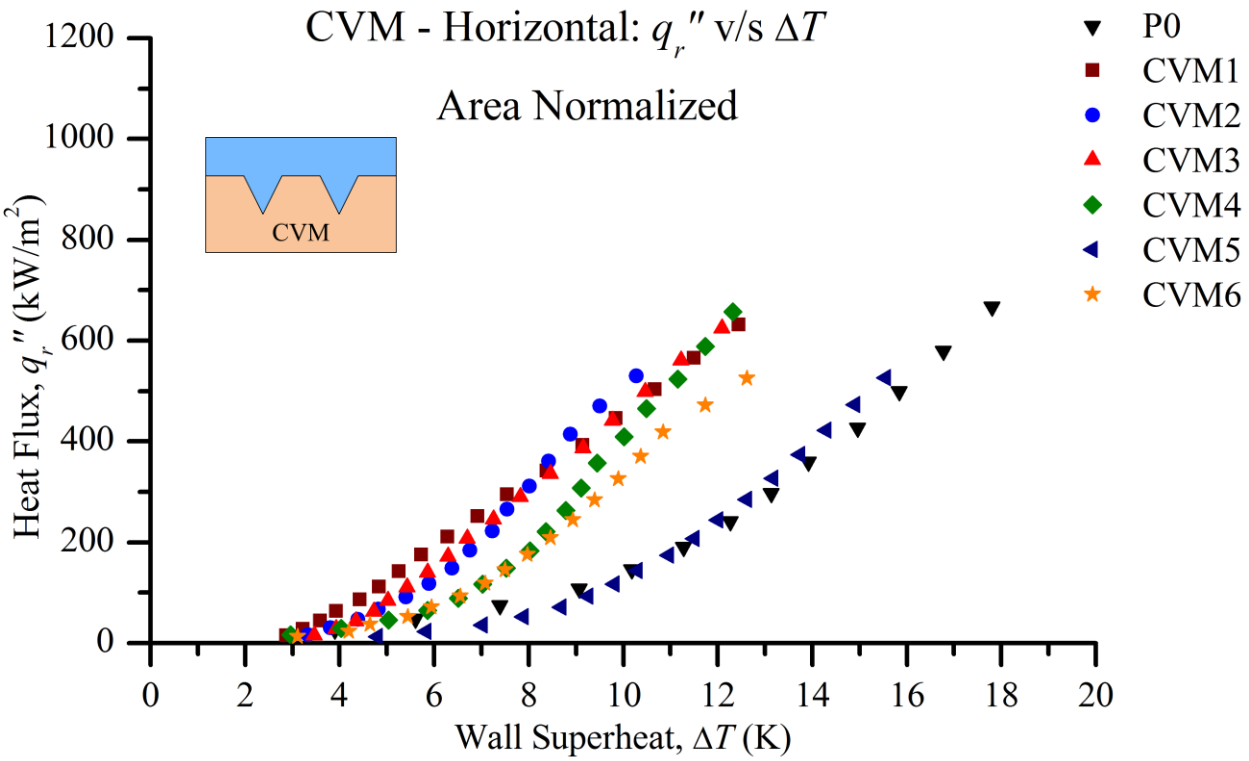

Figure 31: Boiling curves based on area normalized heat fluxes for the CVM test sections in the horizontal orientation

5.3 Axial Rectangular Microchannels (ARM)

Six ARM test section surfaces having distinctive microchannel geometries were tested, and the experimental results for these are presented in this sub-section. The effects of the microchannel geometric parameters on the heat transfer performance of the surface were analyzed. The obtained results were also area normalized, and their overall influence on the performance of the ARM test sections are also discussed in this section.

5.3.1 Experimental Results and Heat Transfer Performance

The results obtained for the ARM test sections in both orientations show great enhancements in the overall heat transfer performance compared to the plain surface. These test sections were also successfully tested up to an approximate heat flux of 1070 kW/m^2 in both, horizontal and vertical orientations. None of the ARM surfaces reached their respective critical heat flux condition. The performance curves were evaluated from the generated experimental data in the vertical and horizontal orientations, and are shown in Figure 32 and Figure 33, respectively. Test section ARM2 produced the best heat transfer performance among all the ARM surfaces. In the vertical orientation, ARM2 yielded a heat transfer coefficient of 95.9 kW/m^2·K while maintaining a wall superheat of 11.1 K, whereas in the horizontal orientation, a heat transfer coefficient of 88.1 kW/m^2·K was achieved at a wall superheat of 12.1 K.

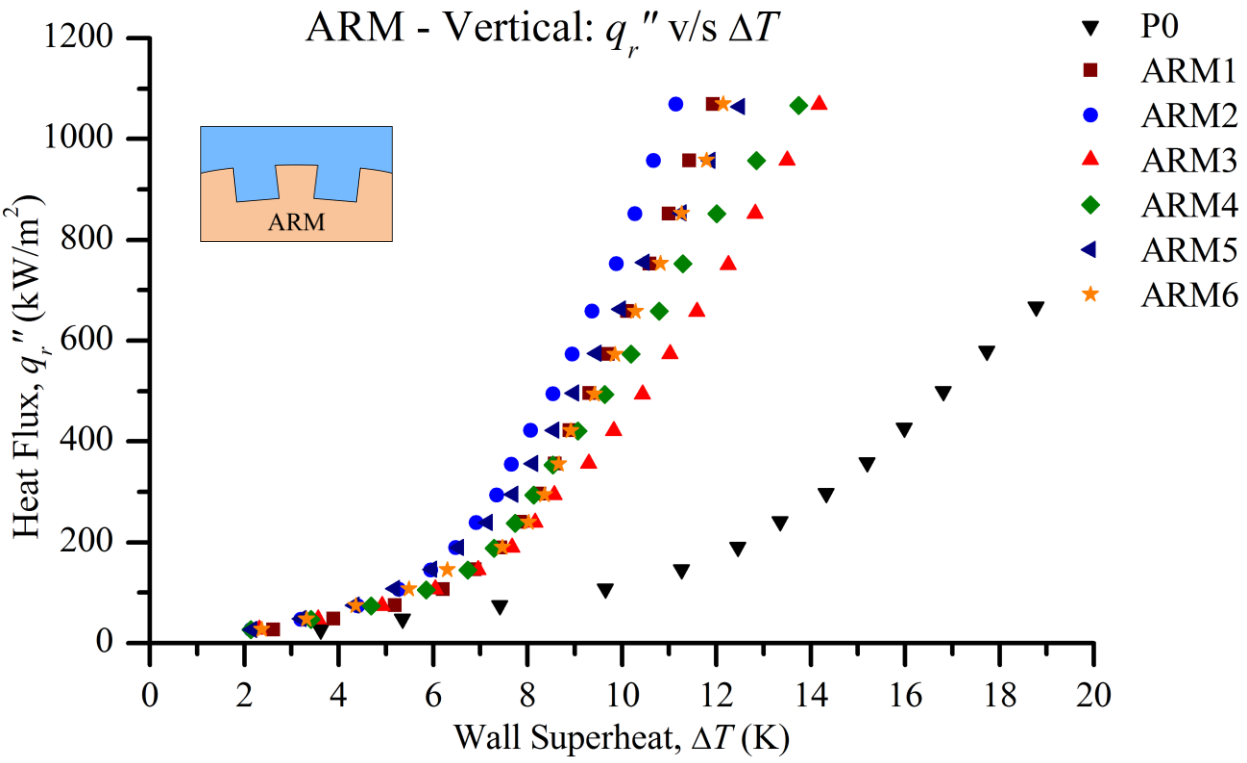

Figure 32: Boiling curves for the ARM test sections in the vertical orientation

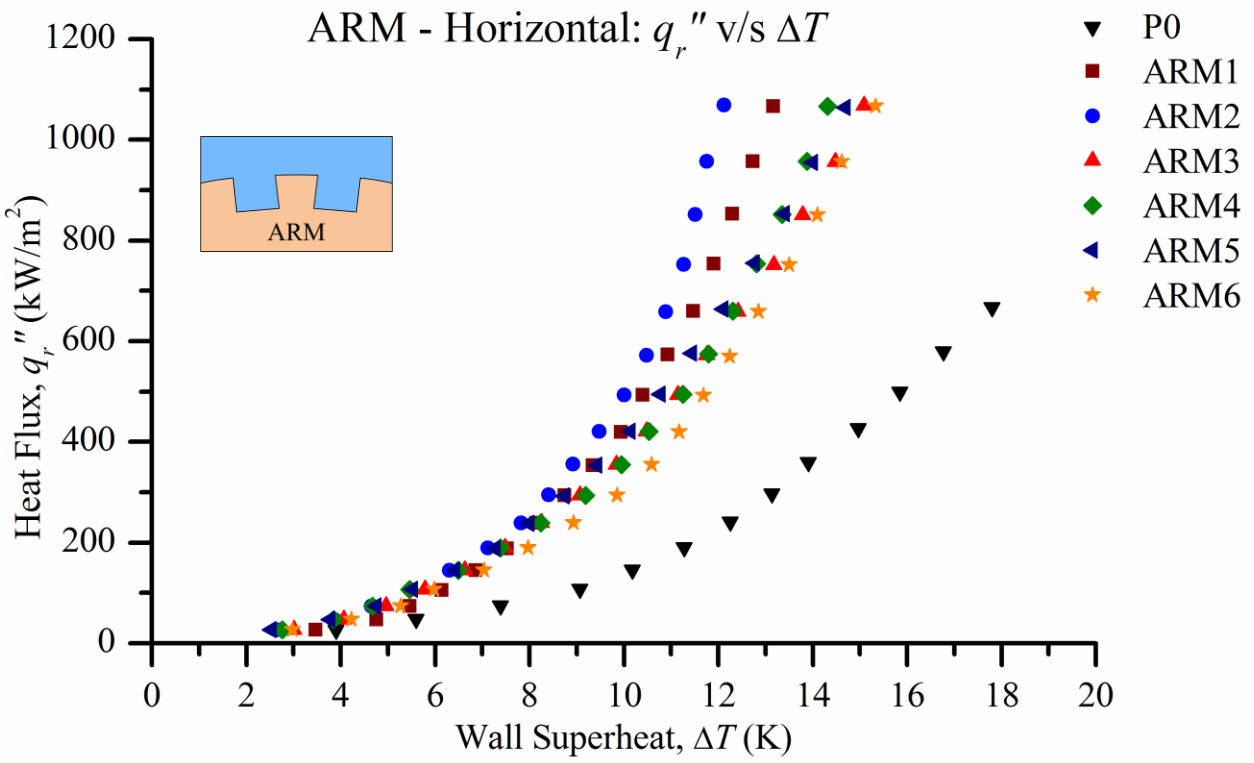

Figure 33: Boiling curves for the ARM test sections in the horizontal orientation

The heat transfer coefficients obtained for other ARM test sections in the vertical orientation, were in the range of 75.3 – 89.5 kW/m^2·K while maintaining the wall superheat in range of 11.9 – 14.2 K, at an approximate heat flux of 1070 kW/m^2. Similarly in the horizontal orientation, the heat transfer coefficients obtained were in the range of 69.5 – 81.0 kW/m^2·K with the wall superheat in the range of 13.2 – 15.3 K. Detailed results for the these test sections at their respective highest heat flux conditions are provided in Table 8 for further reference. The overall enhancement factors of 2.1 – 2.7 were achieved for the ARM test sections in the vertical orientation. Whereas in the horizontal orientation, the overall enhancement factors obtained were in the range of 1.9 – 2.3. After analyzing the results obtained for the ARM surface, it was observed that the performance in the vertical orientation was comparatively superior to that obtained in the horizontal orientation, and a discussion on the same is presented in Section 0.

Test Section	*Horizontal Orientation*				*Vertical Orientation*			
	q_r'' kW/m^2	ΔT K	h kW/m^2·K	h_{ARM}/h_{P0} -	q_r'' kW/m^2	ΔT K	h kW/m^2·K	h_{ARM}/h_{P0} -
P0	667	17.8	38	-	667	18.8	36	-
ARM1	1066	13.2	81	2.2	1069	11.9	90	2.5
ARM2	1069	12.1	88	2.3	1069	11.1	96	2.7
ARM3	1068	15.1	71	1.9	1068	14.2	75	2.1
ARM4	1066	14.3	74	2.0	1066	13.8	78	2.2
ARM5	1064	14.7	72	1.9	1064	12.5	85	2.4
ARM6	1066	15.3	70	1.9	1069	12.1	88	2.5

Table 8: Experimental results for ARM test sections in the horizontal and vertical orientation at their respective highest heat flux conditions

A steady increase in the heat transfer coefficient was observed with an increase in the heat flux condition, and a plot showing this trend is given in Figure 34. The critical heat flux limit was successfully extended from 700 kW/m^2 obtained for a plain surface, to a limit of at least 1070 kW/m^2 with the use of the ARM surfaces as shown in the figure. The uncertainty in the heat transfer coefficient results of the best performing ARM2 test section are also shown in the form of error bars in the plot. An uncertainty of just ±6.2% was observed in the achieved heat transfer coefficient for the ARM2 test section in the vertical orientation, at a heat flux of 1069 kW/m^2. Similar plot of heat transfer coefficient as a function of the heat flux for the ARM test sections in the horizontal orientation is shown in Figure 54 in the Appendix.

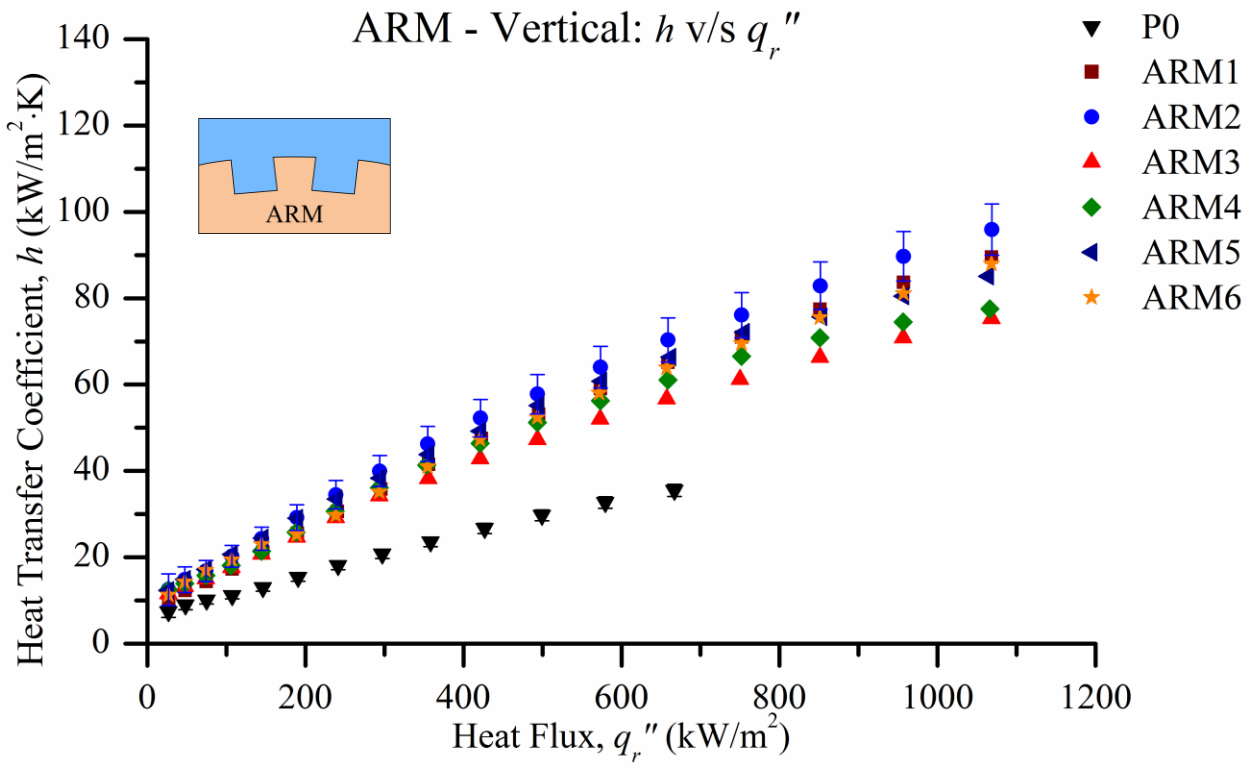

Figure 34: Plot of the heat transfer coefficient against the heat flux, comparing the ARM test section results in the vertical orientation

5.3.2 Effects of Microchannel Dimensions

The results obtained for the ARM test sections were distinct and comparable, and it was possible to analyze the effects of the microchannel geometric parameters on the heat transfer performance. The channel depth effects on the performance are explained using the plot shown in Figure 35, which presents the boiling curves for ARM1 and ARM2 having microchannel depths of 0.22 mm and 0.39 mm, respectively. Dimensions of the other geometric parameters were the same for this pair of test sections. ARM2 consisting of deeper microchannel grooves delivered relatively better heat transfer performance than ARM1. A similar comparison between ARM5 and ARM6 having channel depths of 0.37 mm and 0.51 mm, respectively was made, and their respective performance curves are also shown in the figure. At higher heat flux conditions,

ARM6 showed better heat transfer performance compared to ARM5. From these results it was concluded that the axially oriented grooves show greater enhancements in heat transfer performance with deeper microchannels.

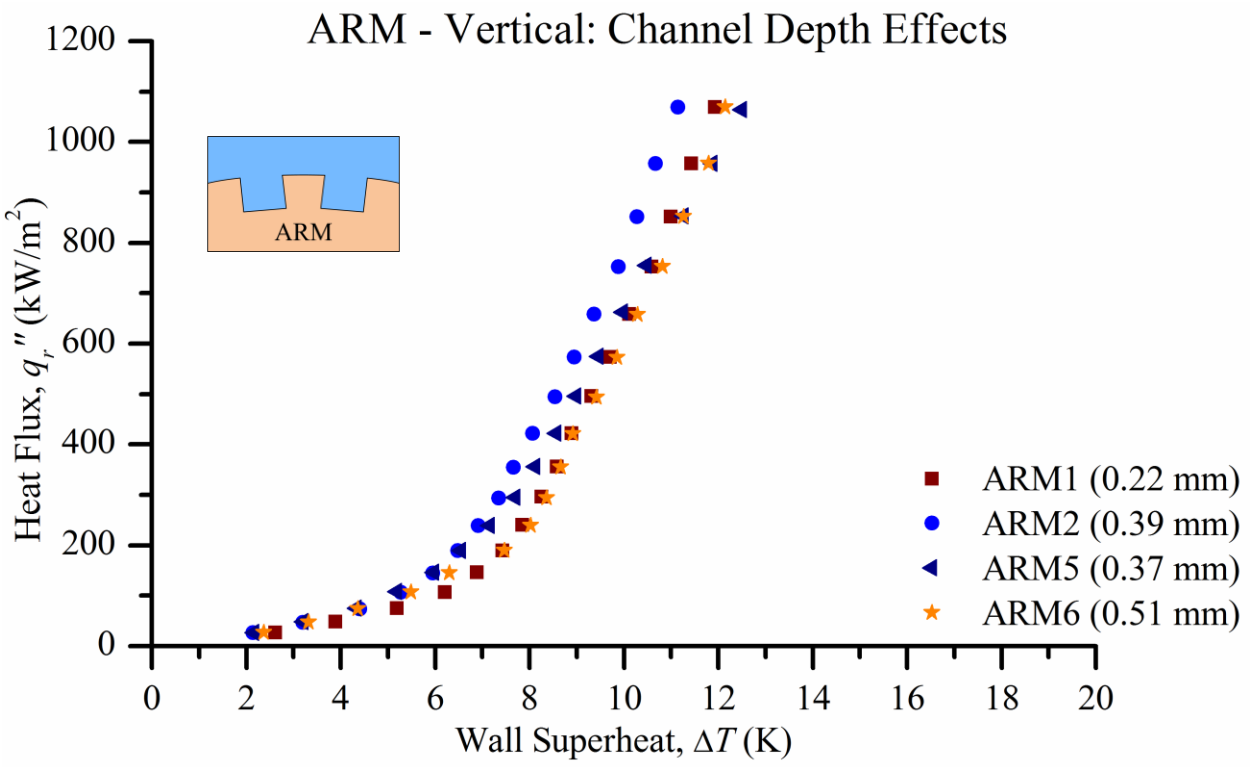

Figure 35: Boiling curve comparison to analyze the effects of the channel depth

The influence of the channel width on the heat transfer performance was more prominent than that of the channel depth for the ARM surfaces. The boiling curves for ARM1 and ARM3 having channel widths of 0.4 mm and 0.52 mm, respectively, were compared and analyzed for this purpose and are shown in Figure 36. From the comparison it was concluded that the surfaces with narrower microchannels yielded relatively better heat transfer performance. A similar trend was observed while comparing the boiling curves of test sections ARM2 and ARM5 having channel widths of 0.4 mm and 0.53 mm, respectively. At higher heat flux conditions, ARM2 surface consisting of narrower grooves produced significantly better heat transfer performance.

Hence for the axially oriented rectangular base microchannels, it was concluded that deeper and narrower grooves aided in enhancing the overall heat transfer performance and extending the critical heat flux limit for the surface

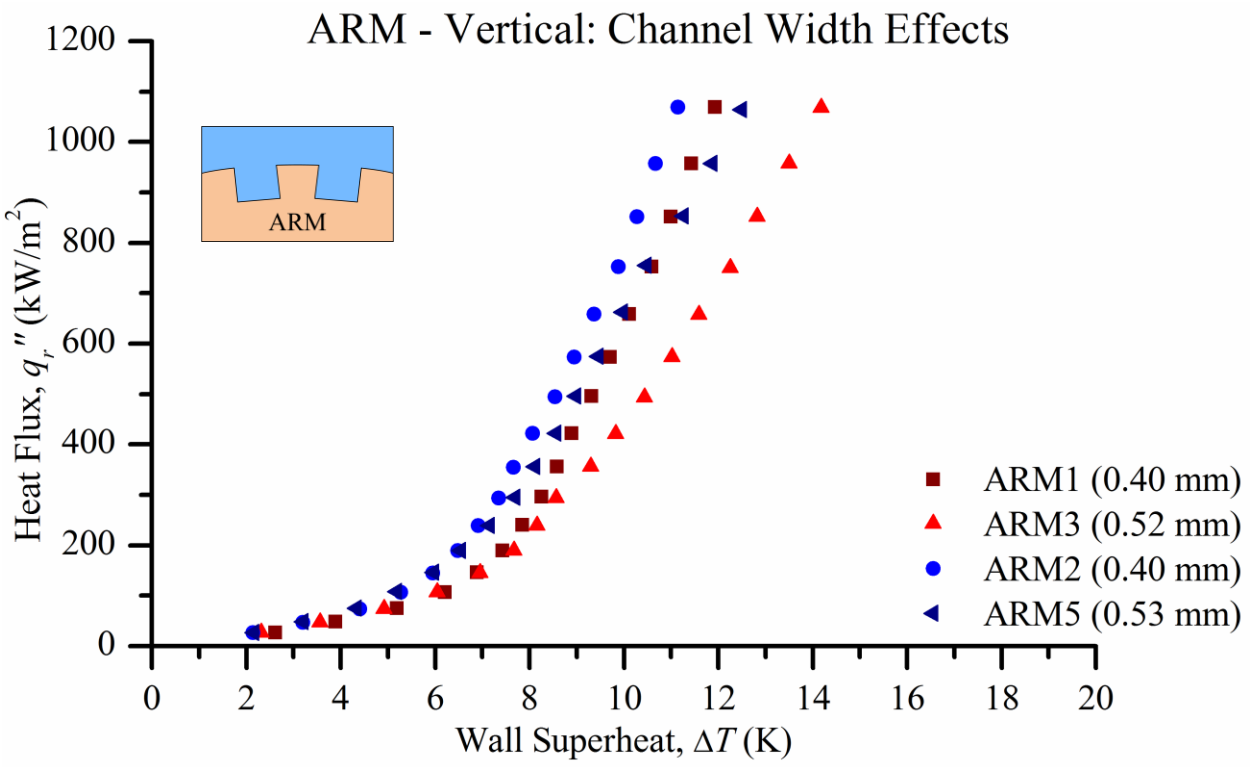

Figure 36: Boiling curve comparison to analyze the effects of the channel width

5.3.3 Area Normalized Heat Transfer Results

In this sub-section the area normalized results for the ARM test sections are presented and discussed. These results also showed good enhancement in the overall heat transfer performance as given in Figure 37. As discussed in Section 5.1.3, these results also indicated the influence of factors other than the area enhancement responsible in augmenting the overall performance of the surface. Comparing test sections, ARM1 and ARM3, having different channel widths of 0.4 mm and 0.52 mm, respectively, but the same channel depth, pitch, and area enhancement factor. As seen in the figure, the performance obtained with ARM1 was

significantly better than the performance obtained with ARM3, which indicated that narrower channels or wider fins were mainly responsible for the performance enhancements. In the case of ARM2 and ARM5, although the channel width of ARM2 is smaller than ARM5, the pitch is different resulting in a greater area enhancement factor for the ARM2 surface. These effects were seen to balance out, producing nearly the same performance for the two channel geometries in their area normalized results as shown in the figure. Similar plot of the area normalized results for the ARM test sections in the horizontal orientation is shown in Figure 55 in the Appendix for further reference.

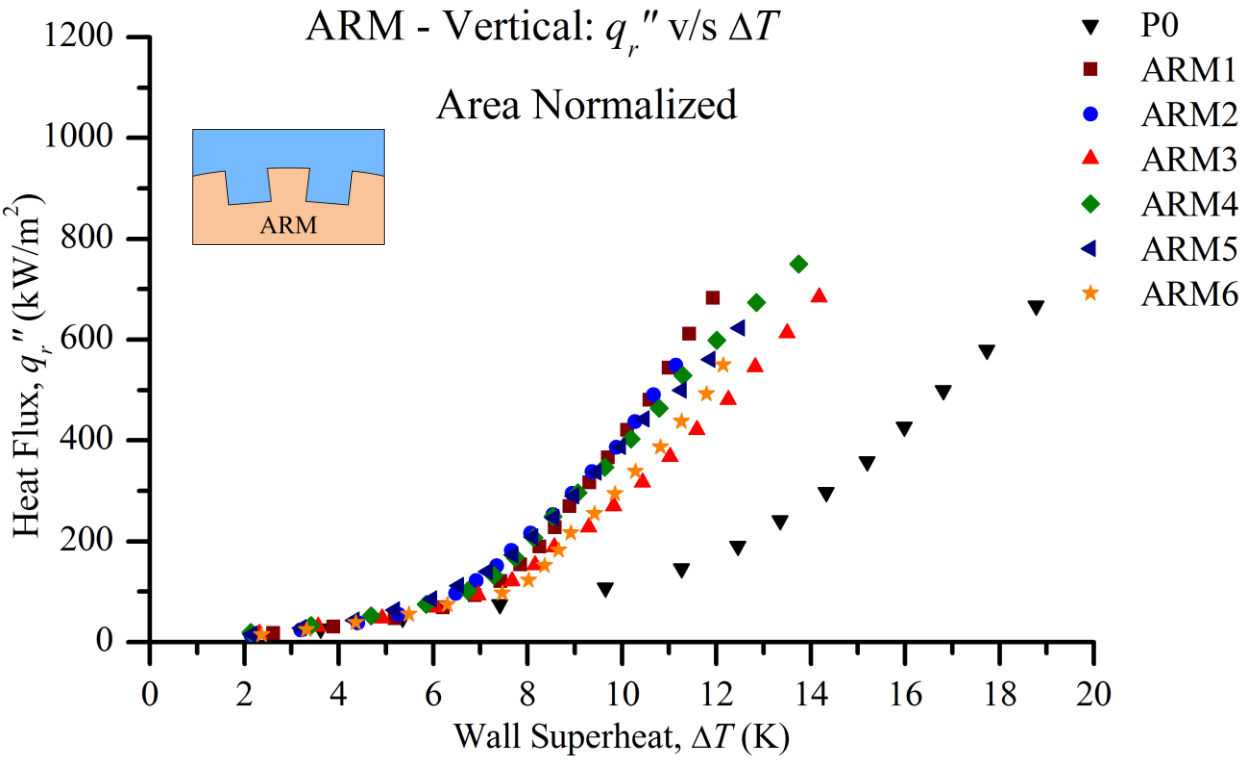

Figure 37: Boiling curves based on area normalized heat fluxes for the ARM test sections in the vertical orientation

5.4 Effects of Tube Orientation

As described in the previous sections, all the test sections were tested in the horizontal as well as the vertical orientation, to study the effects of tube orientation on the boiling heat transfer performance for the different surface geometries. Test section CRM3 yielded the highest heat transfer coefficient of 129.1 kW/m^2·K in the horizontal orientation. Whereas in the vertical orientation a heat transfer coefficient of only 109.1 kW/m^2·K was achieved with the same surface. The results for all the CRM test sections in the horizontal and vertical orientation are shown in the Figure 22 and Figure 23, respectively. Similarly comparing the performance curves for each test section in these figures, it was concluded that better heat transfer performance was achieved in the horizontal orientation. Also comparing the results detailed in the Table 6, an approximate enhancement of 10 – 20% in the horizontal orientation was observed over the performance in the vertical orientation for the CRM test sections. The results for the CVM test sections in the horizontal and vertical orientation are presented in the Figure 29 and Figure 51, respectively. Exactly the same conclusion of better heat transfer performance in the horizontal orientation was drawn from the results of these surfaces.

In the case of the axially grooved rectangular base microchannel test sections, it was noticeably observed that the performance in the vertical orientation was comparatively superior to that in the horizontal orientation. The results for the ARM rest section in the vertical and horizontal orientations are given in Figure 32 and Figure 33, respectively. Also the best performing ARM2 test section delivered a heat transfer coefficient of 95.9 kW/m^2·K in the vertical orientation compared to just 88.1 kW/m^2·K in the horizontal orientation. An approximate performance enhancement of 10 – 15% was observed for the ARM test section in the vertical orientation compared to the horizontal orientation under high heat flux conditions. These

experimental results clearly show a significant influence of the microchannel groove orientation on the performance of a test section in different tube orientations. Test sections with circumferentially grooved surfaces yielded better performance in the horizontal orientation, whereas for the axially grooved surfaces better performance was obtained in the vertical orientation. It was concluded that the bubble departure behavior from these circumferentially and axially oriented microchannels in the different tube orientations, influenced the overall heat transfer performance of the test sections. For the CRM and CVM test sections in the horizontal orientation, the bubbles generated on the underside of the tube were observed to slide on the side walls, thereby forcing the departure of the bubbles still growing on these walls. Similarly for the surfaces in the vertical orientation, the bubbles generated towards the bottom of the test section, were observed to slide upwards over the surface and force the departure of bubbles in its path. Hence it was concluded that the tube orientation preferentially enhanced the overall heat transfer performance depending on the microchannel orientation over the surface.

5.5 Bubble Dynamics

In order to better understand the heat transfer mechanism over the microchannel surface the experimental setup with the clear visual access to the heated surface was designed and developed as described in Section 4.1. A high-speed microscope camera was used to capture the bubble nucleation and growth on the modified cylindrical surfaces. Keyence® VW5000 motion analyzing microscope coupled with a VH-Z00R lens was used to record the videos at a magnification of 50X and a frame rate of 1000 or 4000 fps. Light from external sources was provided to improve the brightness and clarity of the videos obtained at higher frame rates. Videos were mainly recorded in the lower heat flux range, so as to generate videos without any interruptions from the bubbles nucleating and growing in the vicinity. In order to clearly

visualize and study the bubble activity inside the microchannel area, the videos were recorded with the circumferentially grooved test sections, on their top and bottom surfaces in the horizontal orientation. The bubble activities in the rectangular and V-groove cross-section geometries were recorded and analyzed. These generated videos are presented as image sequences and the bubble behavior over the microchannels are discussed below, in this section.

5.5.1 Low Heat Flux Condition

Sequential images of nucleation, growth and departure of bubbles from the top surface of CVM1 at a low heat flux near the onset of nucleate boiling, are shown in Figure 38. The video was recorded at a high frame rate of 4000 fps. In image (a), a large bubble is seen departing, while a new bubble nucleates inside the groove on the right wall of the microchannel. As this bubble grows inside the groove, it occupies the entire microchannel region, almost filling the entire V-groove, as shown in images (b) and (c). As this bubble reaches its departure diameter it is expelled from the groove, and then it initiates coalescing with the previously ejected bubble. At the end of 0.75 milliseconds from nucleation, complete coalescence of this bubble into the large bubble can be seen in image (d). This larger bubble pins to the fins at the outer surface and slowly grows, as shown in image (e). At 2.25 milliseconds another bubble nucleated inside the microchannel interacts with the larger bubble and can be seen coalescing with the larger bubble in image (f). Continuous departure of these large bubbles was observed because of the buoyancy forces acting on these bubbles forcing them to detach from the top surface.

Under similar heat flux conditions, a significantly lower bubble generation frequency was observed on the underside of the same test section surface. The bubbles nucleating inside the grooves on the bottom surface were initially seen to be ejected downwards out of the microchannel. Immediately after the ejection, buoyancy forces took over and were responsible

for the pinning of these bubbles on to the fins at the outer surface. None of these bubbles were seen to intrude or fill the groove area while pinning to the surface. After reaching an unstable diameter these bubbles were seen to slide around the test section and finally detach from the surface. After complete departure of the pinned bubble, a new bubble was seen to nucleate from the same cavity and a continuous cycle of bubble nucleation, growth, and departure was observed. Even while the bubbles were growing on the bottom surface, the grooves were flooded with the bulk liquid thereby enabling the rewetting of the heated surface. At these low heat flux conditions, the bubble generation frequency on the bottom surface was relatively much lower than that observed on the top surface. This was because of the dwelling and attachment of the bubbles on the bottom surface for longer time periods, making it difficult for new bubbles to nucleate. Also on the underside of the tube, lower wall superheats were observed, which was partially responsible for the lower generation rates on the bottom surface.

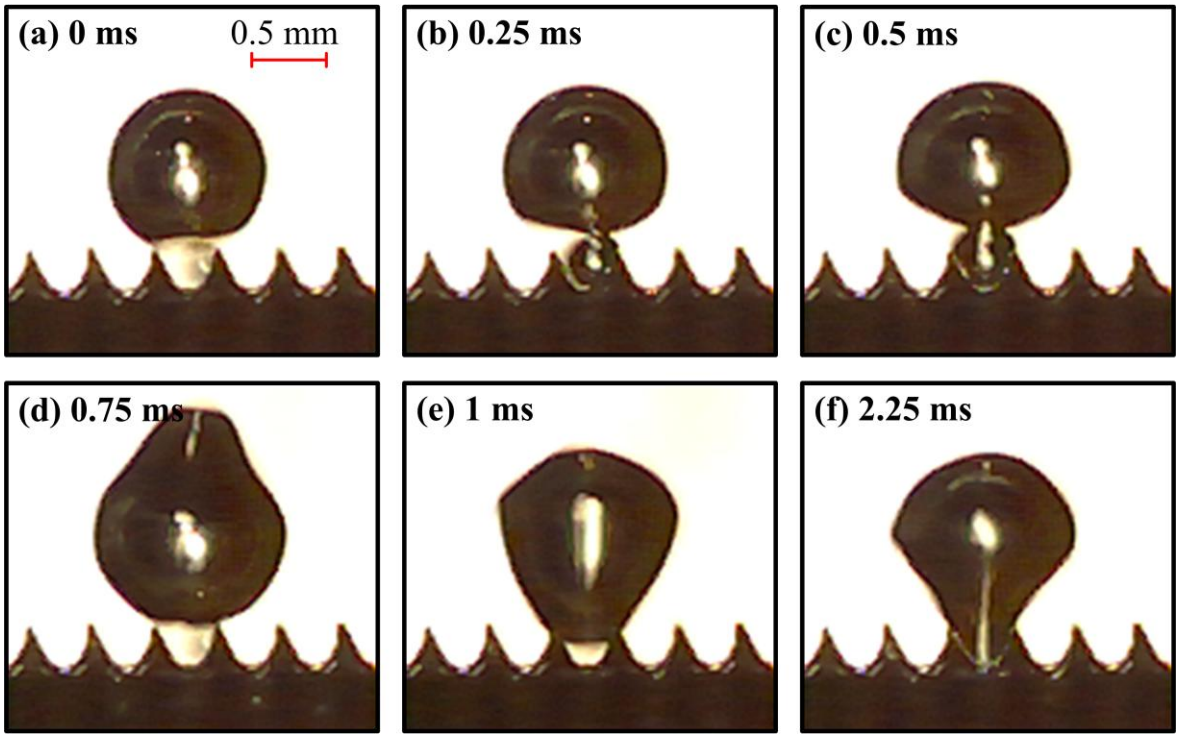

Figure 38: Bubble dynamics on the top surface of CVM1 at low heat flux conditions

5.5.2 Medium Heat Flux Condition

An image sequence of the bubble interactions observed on the bottom surface of CVM1 at a heat flux of 75 kW/m^2 is shown in Figure 39. The video for this image sequence was recorded at a frame rate of 1000 fps. Image (a) in the figure shows a bubble growing while attached to the microchannel fins. In less than a millisecond, this bubble initiates to detach from the surface and new bubble nucleates on the microchannel wall as seen in image (b). At 2 milliseconds, this second bubble grows inside the microchannel region while almost touching all the walls of the groove. At this point first bubble has completely detached from the surface and initiated its interaction with the large bubble present in the vicinity as seen in image(c).

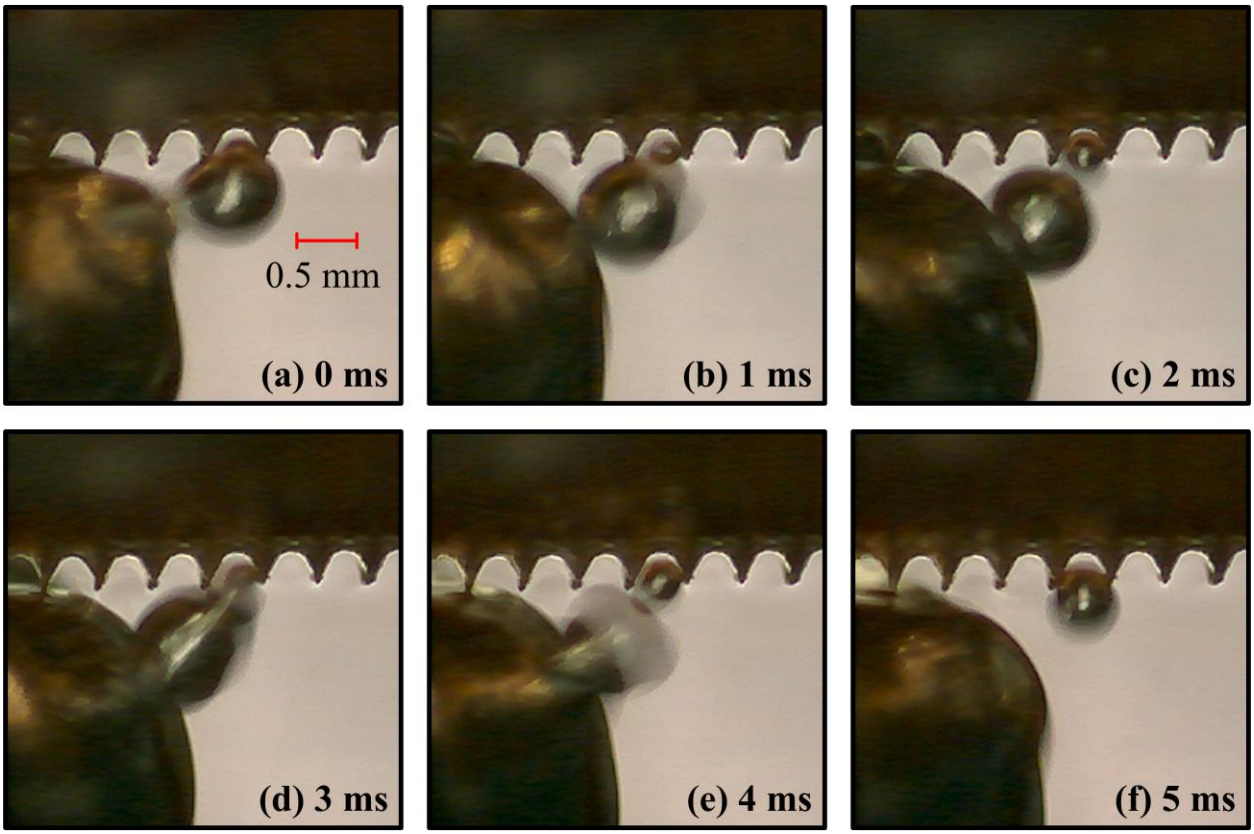

Figure 39: Bubble dynamics on the bottom surface of CVM1 at a heat flux of 75 kW/m^2

In less than a millisecond, the second bubble is also ejected from the microchannel and starts coalescing with the first bubble as seen in image (d). Immediately after the ejection of the second bubble, a third bubble is seen to nucleate. Images (e) and (f), show the coalescence of the first and second bubble, and their eventual merger into the large bubble at the end of 5 milliseconds. An important observation of micro bubbles feeding into a larger bubble was made from this video and other videos recorded at similar or higher heat flux conditions. Comparing the videos at different heat flux conditions, it was observed that the bubble generation frequency increased with an increase in the hear flux. Also simultaneous growth of numerous larger bubbles by the micro bubbles feeding mechanism was observed in these videos.

An image sequence of another video recorded on the top surface of CVM5 is shown in Figure 40. The important events from the video clearly showing the bubble feeding mechanism on the top surface are presented in this figure. The video was recorded at a similar heat flux of 80 kW/m^2, and at a frame rate of 4000 fps. Image (a) shows a bubble growing on the left wall of the central microchannel groove. This growing bubble was seen to attach to the microchannel fins, and interact with the previously departed bubble. At approximately 2.75 milliseconds after nucleation, these two bubbles coalesce and begin to detach from the surface as seen in image (b). In the next 0.25 milliseconds this bubble completely detaches from the surface. Immediately after that, a new bubble is seen to nucleate from a different cavity on the right wall of the microchannel as shown in image (c). This new bubble partially fills the microchannel area as it grows, as seen in image (d). This bubble was also seen to grow and similarly coalesce with the larger bubble after departing from the surface. Alternate activation of neighboring cavities for the generation of micro bubbles was observed in this video. The ejection of micro bubbles from multiple nucleation sites in close proximity, to feed a larger bubble was seen in this video.

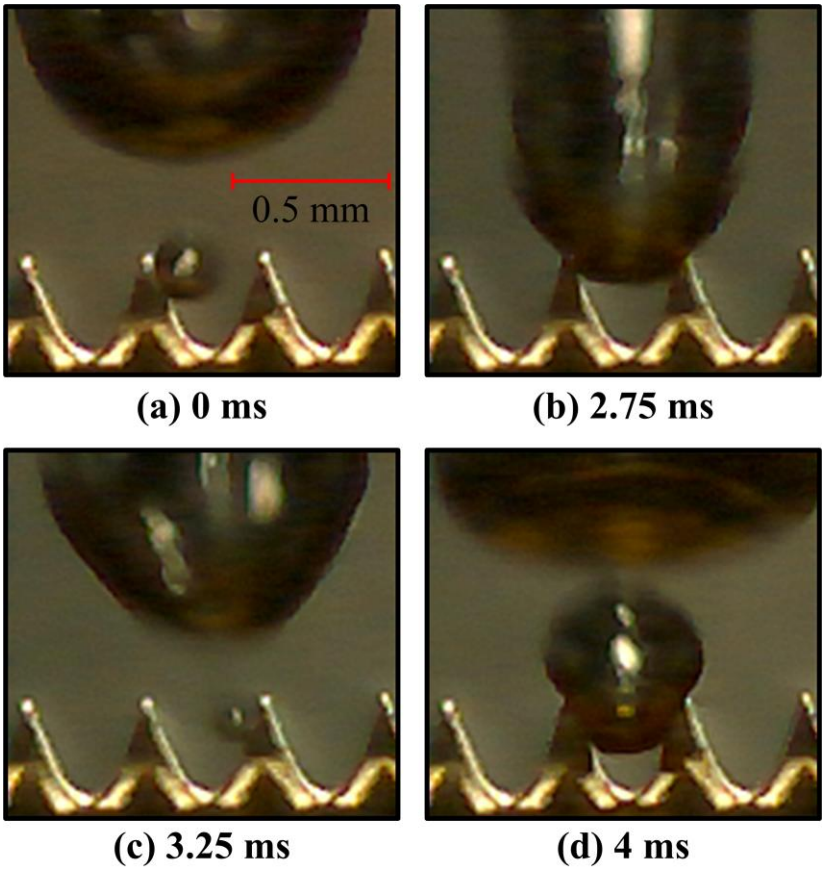

Figure 40: Bubble dynamics on the top surface of CVM5 at a heat flux of 80 kW/m^2

An important bubble growth mechanism was observed while analyzing the recorded videos at similar or higher heat flux conditions. Continuous nucleation and ejection of micro bubble from the grooves, aided in the growth of a larger bubble pinned to the surface, describes the bubble feeding mechanism during nucleate boiling. The generated micro bubbles were seen to be ejected out of the groove, in less than a millisecond, so as to make way for the bulk liquid to flood and rewet the heated surface.

5.5.3 High Heat Flux Condition

The best performing test section CRM3 was used to capture videos of bubble dynamics at a comparatively higher heat flux of 150 kW/m^2 than that discussed in the previous sub-sections.

At higher heat fluxes than this, it was difficult to record clear uninterrupted videos for these surfaces due to the extensive movement of the bubbles nucleating in the vicinity. Videos on the top and the bottom surfaces of this test section were recorded at a frame rate of 4000 fps. An image sequence of a video captured on the top surface of CRM3 is presented in Figure 41. In image (a), a bubble nucleating from an active cavity on the microchannel wall can be seen. In a time span of 2 milliseconds, the bubble grows inside the groove and pins to the fins at the outer surface. At 3 milliseconds, another micro bubble nucleated from the cavity is seen to feed into the first bubble as shown in image (c). Two additional micro bubbles were seen to coalesce into the first bubble, before it departs from the surface due to the increased buoyancy forces. Images (d) and (e) show a new bubble ejected from the active cavity and attaching to the opposite wall of the microchannel. Instantaneously after the ejection of this bubble, another bubble nucleates from the same cavity as seen in the image (e). Both these bubbles simultaneously grow on their respective walls, and ultimately coalesce with each other as seen in images (f) and (g). This coalesced bubble nearly fills the entire microchannel cross-section area as it grows.

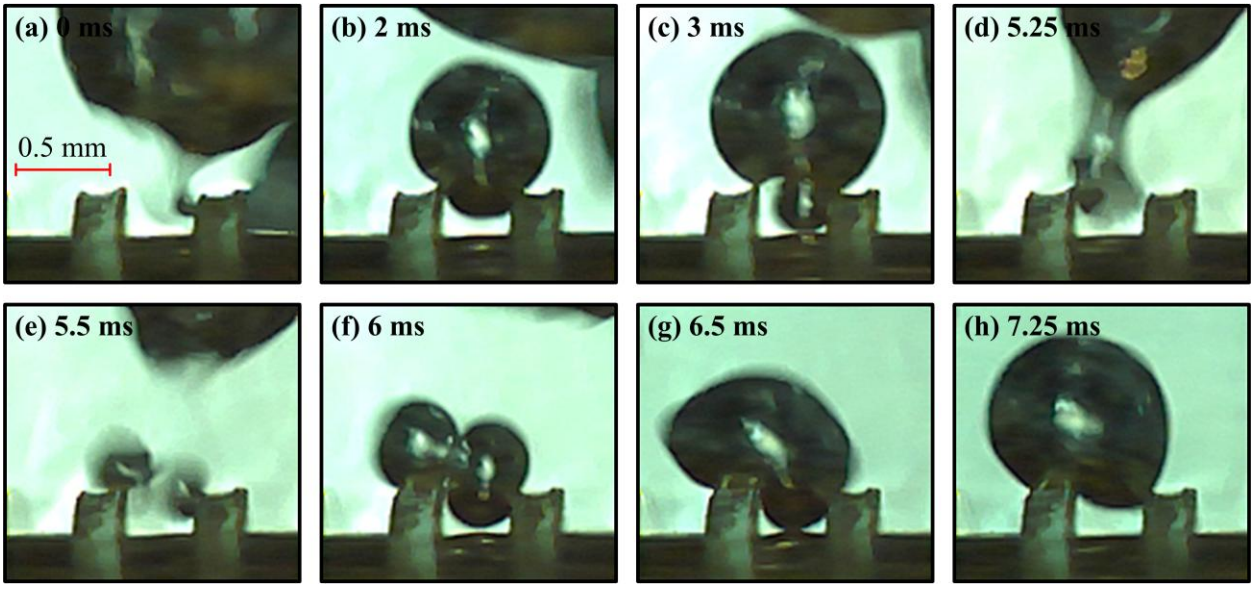

Figure 41: Bubble dynamics on the top surface of CRM3 at a heat flux of 150 kW/m^2

As seen in image (g) the rectangular base in these channels are highly advantageous, since the corner regions were always filled with the bulk fluid, allowing for the continuous supply of liquid to the active nucleation sites. As the bubble grows, it clears the microchannel area thereby providing more access to the bulk fluid to completely rewet the heated surface.

The rewetting phenomenon and the continuous liquid supply through the corners of the rectangular cross-section microchannels, aided in extending the critical heat flux limits and significantly enhancing the overall boiling heat transfer performances for the different surfaces. The extension in the critical heat flux limit was seen to be more prominent with the rectangular cross-section geometry than with the V-groove cross-section geometry, because of the continuous supply of liquid through the corners even at higher heat flux conditions. It was concluded that the corners of these rectangular base test sections weren't filled by the round bubbles while growing inside the channels, which gave uninterrupted access for the rewetting of the heated surface.

6. Conclusions

A pool boiling experimental investigation for water over cylindrical tubes with open microchannels was conducted in this study. Testing was performed with twenty distinct microchannel surfaces to characterize the effects of various parameters on the heat transfer performance. The microchannels on the cylindrical tube surface were manufactured either circumferentially around the test section or axially along the length. Rectangular and V-groove cross-section geometries were employed, and a parametric study to analyze the effects of the microchannel dimensions on the heat transfer performance was conducted. Testing was performed in both, horizontal and vertical orientation for all the fabricated test sections, to investigate the tube orientation effects. The results obtained for these surfaces show that the microchannel groove orientation, cross-section geometry, dimensions of microchannel geometry, and tube orientation of the test section, greatly influence the overall heat transfer performance. The following conclusions were drawn after analyzing the experimental results.

- A maximum heat transfer coefficient of 37.5 $kW/m^2 \cdot K$ was obtained with the plain surface test section in the horizontal orientation at a heat flux of 667 kW/m^2. The plain surface reached its critical heat flux condition at an approximate heat flux of 700 kW/m^2.
- Almost all the microchannel test sections were successfully tested up to an approximate heat flux of 1100 kW/m^2 without reaching their CHF limits. Hence an improvement of at least 1.6 times was achieved in the critical heat flux limit with the use of microchannel surfaces.
- The circumferentially grooved rectangular microchannel test sections showed significant enhancements in the heat transfer performance. In the horizontal orientation the overall enhancement factors achieved were in the range of 2.5 – 3.4, whereas in the vertical orientation the corresponding overall enhancement factors were in the range of 2.2 – 3.1.

- The highest heat transfer coefficient of 129 kW/m^2·K was achieved for test section CRM3 in the horizontal orientation, while maintaining the wall superheat of 8.5 K at a heat flux of 1095 kW/m^2. In the vertical orientation a maximum heat transfer coefficient of 109 kW/m^2·K was obtained with a corresponding wall superheat of 10.0 K.
- The microchannel geometric parameters show considerable influence on the heat transfer performance of the CRM surfaces tested in this study. Comparatively shallower and narrower microchannel grooves aid in enhancing the surface performance at higher heat flux conditions. Larger fin widths on the microchannel surfaces also yields relatively better performance.
- Good enhancements with the CVM test sections were obtained. Overall enhancement factors in the range of 1.8 – 2.4 were achieved in the horizontal orientation, and 2.0 – 2.3 were obtained in the vertical orientation
- CVM2 was the only microchannel test section to reach its critical heat flux condition at 900 kW/m^2, possibly due to the its low area enhancement factor. The parametric effects of the microchannel dimensions for the CVM test sections were inconclusive as fairly similar results were obtained for these surfaces.
- The overall enhancement factors in the horizontal orientation for the axially grooved rectangular base microchannel test sections were in the range of 1.9 – 2.3. However in the vertical orientations, the enhancement factors in range of 2.1 – 2.7 were achieved.
- ARM2 was the best performing axially grooved test section, achieving a heat transfer coefficient of 96 kW/m^2·K at a heat flux of 1069 kW/m^2 while maintaining a wall superheat of 11.1 K in the vertical orientation.

- The parametric study for the ARM surfaces show that deeper and narrower grooves aid in enhancing the overall heat transfer performance.
- The results obtained for the modified surfaces were normalized based on the total wetted surface area of each test section. These area normalized results clearly showed that other factors besides the surface influenced the heat transfer performance.
- The circumferentially grooved CRM and CVM test sections yield better heat transfer performances in the horizontal orientation, whereas the axially grooved ARM test sections yield better performances in the vertical orientation. The tube orientation preferentially enhances the surface performance depending on the orientation of the microchannel grooves.
- A comparison between the microchannel geometrical cross-sections showed superior performance with the rectangular grooves.

The bubble dynamics over the microchannel surfaces in the horizontal orientation was recorded and analyzed to reveal the underlying boiling heat transfer mechanisms. The conclusions derived based on the analysis of the captured videos are given below.

- At low heat flux conditions, the bubble generation frequency on the underside of the tube is comparatively lower than that on the top surface. This is due to the buoyancy forces acting on the growing bubbles. On the bottom surface these forces bind the bubble to the surface until it reaches an unstable diameter, making it difficult for new bubbles to nucleate. However on the top surface the growing bubbles are forced to detach and depart due to these forces, leading to continuous re-nucleation at the cavities.
- At medium and high heat flux conditions the bubble feeding mechanism in which the micro bubbles nucleating from the active cavities coalesce into a large bubble, aiding in its growth is observed. At higher heat fluxes, bubble nucleation from multiple cavities in close

proximity of each other feed the large bubble. Simultaneous growth of such large bubbles is observed over the entire surface as the heat fluxes are further increased.

- The bubbles nucleating inside the microchannels were seen to be ejected out rapidly in a fraction of a millisecond, clearing the groove area and allowing the rewetting of the heated surface. The rectangular cross-section geometry was highly advantageous to facilitate rewetting through the two corners of the channel, which were always liquid filled. The continuous liquid supply and the rewetting phenomenon are particularly responsible for lowering the wall superheat and extending the critical heat flux limits.

The work presented in this thesis was submitted as a two-part study [33, 34] to the International Journal of Heat and Mass Transfer for review on January 9, 2013.

7. Future Work

In this work a parametric study was conducted with rectangular and V-groove cross-sectional microchannel geometries. During the fabrication, the corners at the bottom of the V-groove microchannels were unintentionally produced with a smooth curve. As explained earlier, this was due to the compromised strength of the micro machining tools. It would be important to observe the change in the performance if the V-groove cross-sections were re-manufactured with the intended sharp corners using a different manufacturing technique. It would be of interest to find out the effect of sharp corners on the heat transfer performance. Further, it is recommended that the study be performed with water as well as different working fluids, especially refrigerants over a range of operating conditions of interest in practical applications.

From literature it has been seen that the porous surfaces greatly aid in decreasing the onset of nucleate boiling temperature. In order to further enhance the heat transfer performance for a given microchannel surface, it would be highly interesting to study the effects of the application of a porous coating over them. Combining the advantages of the both, open microchannels and porous coatings is expected to prove highly advantageous in increasing the heat transfer coefficients. It would also be interesting to visualize the bubble nucleation, growth, and departure from the porous coated surfaces and their interactions with the microchannels.

The most common applications for the enhanced microchannel cylindrical surfaces are two-phase heat exchangers and boilers, which employ multiple tubes in close proximity of each other. It would be greatly beneficial to study the effect on the heat transfer performance in system consisting of bundles of microchannel tubes.

References

[1] Incropera, F., Dewitt, D., Bergman, T., and Lavine, A., 2011, Fundamentals of Heat and Mass Transfer, John Wiley & Sons, Inc.

[2] Kreith, F., Manglik, R., and Bohn, M., 2011, Principles of Heat Transfer, Brooks/Cole.

[3] Webb, R. L., and Pais, C., 1992, "Nucleate Pool Boiling Data for Five Refrigerants on Plain, Integral-Fin and Enhanced Tube Geometries," International Journal of Heat and Mass Transfer, 35(8), pp. 1893-1904.

[4] Memory, S. B., Sugiyama, D. C., and Marto, P. J., 1995, "Nucleate Pool Boiling of R-114 and R-114-Oil Mixtures from Smooth and Enhanced Surfaces. I. Single Tubes," International Journal of Heat and Mass Transfer, 38(8), pp. 1347-61.

[5] Huebner, P., and Kuenstler, W., 1997, "Pool Boiling Heat Transfer at Finned Tubes: Influence of Surface Roughness and Shape of the Fins," International Journal of Refrigeration, 20(8), pp. 575-582.

[6] Tatara, R. A., and Payvar, P., 2000, "Pool Boiling of Pure R134a from a Single Turbo-BII-Hp Tube," International Journal of Heat and Mass Transfer, 43(12), pp. 2233-6.

[7] Rajulu, K. G., Kumar, R., Mohanty, B., and Varma, H. K., 2004, "Enhancement of Nucleate Pool Boiling Heat Transfer Coefficient by Reentrant Cavity Surfaces," Heat and Mass Transfer/Waerme- und Stoffuebertragung, 41(2), pp. 127-132.

[8] Jung, D., Kwangyong, A., and Jinseok, P., 2004, "Nucleate Boiling Heat Transfer Coefficients of Hcfc22, Hfc134a, Hfc125, and Hfc32 on Various Enhanced Tubes," International Journal of Refrigeration, 27(2), pp. 202-6.

[9] Jung, D., Lee, H., Bae, D., and Ha, J., 2005, "Nucleate Boiling Heat Transfer Coefficients of Flammable Refrigerants on Various Enhanced Tubes," International Journal of Refrigeration, 28(3), pp. 451-455.

[10] Thome, J. R., and Ribatski, G., 2006, "Nucleate Boiling Heat Transfer of R134a on Enhanced Tubes," Applied Thermal Engineering, 26(10), pp. 1018-31.

[11] Wen-Tao, J., Ding-Cai, Z., Nan, F., Jian-Fei, G., Numata, M., Guannan, X., and Wen-Quan, T., 2010, "Nucleate Pool Boiling Heat Transfer of R134a and R134a-Pve Lubricant Mixtures on Smooth and Five Enhanced Tubes," Journal of Heat Transfer, 132(11), pp. 111502 (8 pp.).

[12] Chien, L.-H., and Webb, R. L., 1998, "Visualization of Pool Boiling on Enhanced Surfaces," Experimental Thermal and Fluid Science, 16(4), pp. 332-341.

[13] Liang-Han, C., and Webb, R. L., 1998, "A Parametric Study of Nucleate Boiling on Structured Surfaces. I. Effect of Tunnel Dimensions," Transactions of the ASME. Journal of Heat Transfer, 120(4), pp. 1042-8.

[14] Chien, L.-H., and Webb, R. L., 1998, "A Parametric Study of Nucleate Boiling on Structured Surfaces, Part II: Effect of Pore Diameter and Pore Pitch," Journal of Heat Transfer, 120(4), pp. 1049-1054.

[15] Chien, L. H., and Webb, R. L., 2001, "Effect of Geometry and Fluid Property Parameters on Performance of Tunnel and Pore Enhanced Boiling Surfaces," Journal of Enhanced Heat Transfer, 8(5), pp. 329-339.

[16] Nae-Hyun, K., and Kuk-Kwang, C., 2001, "Nucleate Pool Boiling on Structured Enhanced Tubes Having Pores with Connecting Gaps," International Journal of Heat and Mass Transfer, 44(1), pp. 17-28.

[17] Kulenovic, R., Mertz, R., and Groll, M., 2002, "High Speed Flow Visualization of Pool Boiling from Structured Tubular Heat Transfer Surfaces," Experimental Thermal and Fluid Science, 25(7), pp. 547-555.

[18] Chen, Y., Groll, M., Mertz, R., and Kulenovic, R., 2004, "Bubble Dynamics of Boiling of Propane and Iso-Butane on Smooth and Enhanced Tubes," Experimental Thermal and Fluid Science, 28(2-3), pp. 171-178.

[19] Chien, L.-H., and Huang, H. L., 2009, "An Experimental Study of Boiling Heat Transfer on Mesh-Covered Fins," Proc. 2009 ASME Summer Heat Transfer Conference, HT2009, July 19, 2009 - July 23, 2009, San Francisco, CA, United states, 1, pp. 593-599.

[20] Kotthoff, S., Gorenflo, D., Danger, E., and Luke, A., 2006, "Heat Transfer and Bubble Formation in Pool Boiling: Effect of Basic Surface Modifications for Heat Transfer Enhancement," International Journal of Thermal Sciences, 45(3), pp. 217-36.

[21] Gorenflo, D., Baumhogger, E., Windmann, T., and Herres, G., 2010, "Nucleate Pool Boiling, Film Boiling and Single-Phase Free Convection at Pressures up to the Critical State. Part I: Integral Heat Transfer for Horizontal Copper Cylinders," International Journal of Refrigeration, 33(7), pp. 1229-1250.

[22] Gorenflo, D., Baumhogger, E., Windmann, T., and Herres, G., 2010, "Nucleate Pool Boiling, Film Boiling and Single-Phase Free Convection at Pressures up to the Critical State. Part II: Circumferential Variation of the Wall Superheat for a Horizontal 25 Mm Copper Cylinder," International Journal of Refrigeration, 33(7), pp. 1251-1263.

[23] Shou-Shing, H., and Tsung-Ying, Y., 2001, "Nucleate Pool Boiling from Coated and Spirally Wrapped Tubes in Saturated R-134a and R-600a at Low and Moderate Heat Flux," Transactions of the ASME. Journal of Heat Transfer, 123(2), pp. 257-70.

[24] Cieilinski, J. T., 2002, "Nucleate Pool Boiling on Porous Metallic Coatings," Experimental Thermal and Fluid Science, 25(7), pp. 557-564.

[25] Kim, J. H., Rainey, K. N., You, S. M., and Pak, J. Y., 2002, "Mechanism of Nucleate Boiling Heat Transfer Enhancement from Microporous Surfaces in Saturated FC-72," Transactions of the ASME. Journal of Heat Transfer, 124(3), pp. 500-6.

[26] Dominiczak, P. R., and Cieslinski, J. T., 2008, "Circumferential Temperature Distribution During Nucleate Pool Boiling Outside Smooth and Modified Horizontal Tubes," Experimental Thermal and Fluid Science, 33(1), pp. 173-177.

[27] McNeil, D. A., Burnside, B. M., Miller, K. M., and Tarrad, A. H., 2002, "A Comparison between Highflux and Plain Tubes, Boiling Pentane in a Horizontal Kettle Reboiler," 22, pp. 803-814.

[28] Ribatski, G., and Saiz Jabardo, J. M., 2003, "Experimental Study of Nucleate Boiling of Halocarbon Refrigerants on Cylindrical Surfaces," International Journal of Heat and Mass Transfer, 46(23), pp. 4439-51.

[29] Myeong-Gie, K., 2003, "Effects of Tube Inclination on Pool Boiling Heat Transfer," Nuclear Engineering and Design, 220(1), pp. 67-81.

[30] Saidi, M. H., Ohadi, M., and Souhar, M., 1999, "Enhanced Pool Boiling of R-123 Refrigerant on Two Selected Tubes," Applied Thermal Engineering, 19(8), pp. 885-895.

[31] Cooke, D., and Kandlikar, S. G., 2011, "Pool Boiling Heat Transfer and Bubble Dynamics over Plain and Enhanced Microchannels," Journal of Heat Transfer, 133(5).

[32] Cooke, D., and Kandlikar, S. G., 2012, "Effect of Open Microchannel Geometry on Pool Boiling Enhancement," International Journal of Heat and Mass Transfer, 55(4), pp. 1004-1013.

[33] Mehta, J. S., and Kandlikar, S. G., "Pool Boiling Heat Transfer Enhancement over Cylindrical Tubes, Part I: Experimental Results for Circumferential Rectangular Open Microchannels," International Journal of Heat and Mass Transfer.

[34] Mehta, J. S., and Kandlikar, S. G., "Pool Boiling Heat Transfer Enhancement over Cylindrical Tubes, Part II: Experimental Results and Bubble Dynamics for Circumferential V-Groove and Axial Rectangular Open Microchannels," International Journal of Heat and Mass Transfer.

Appendix

Technical Drawings

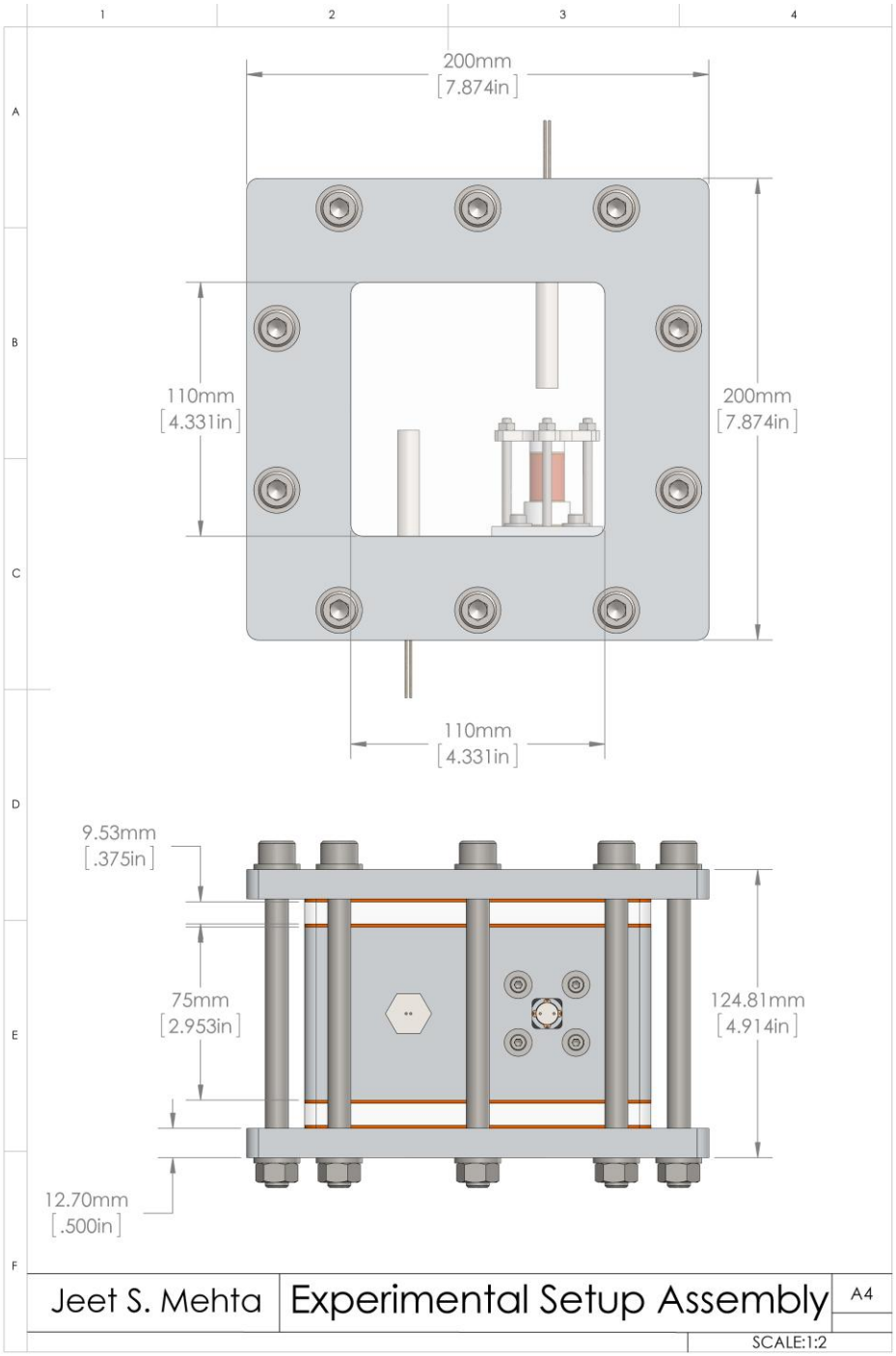

Figure 42: Technical drawing of the experimental setup assembly

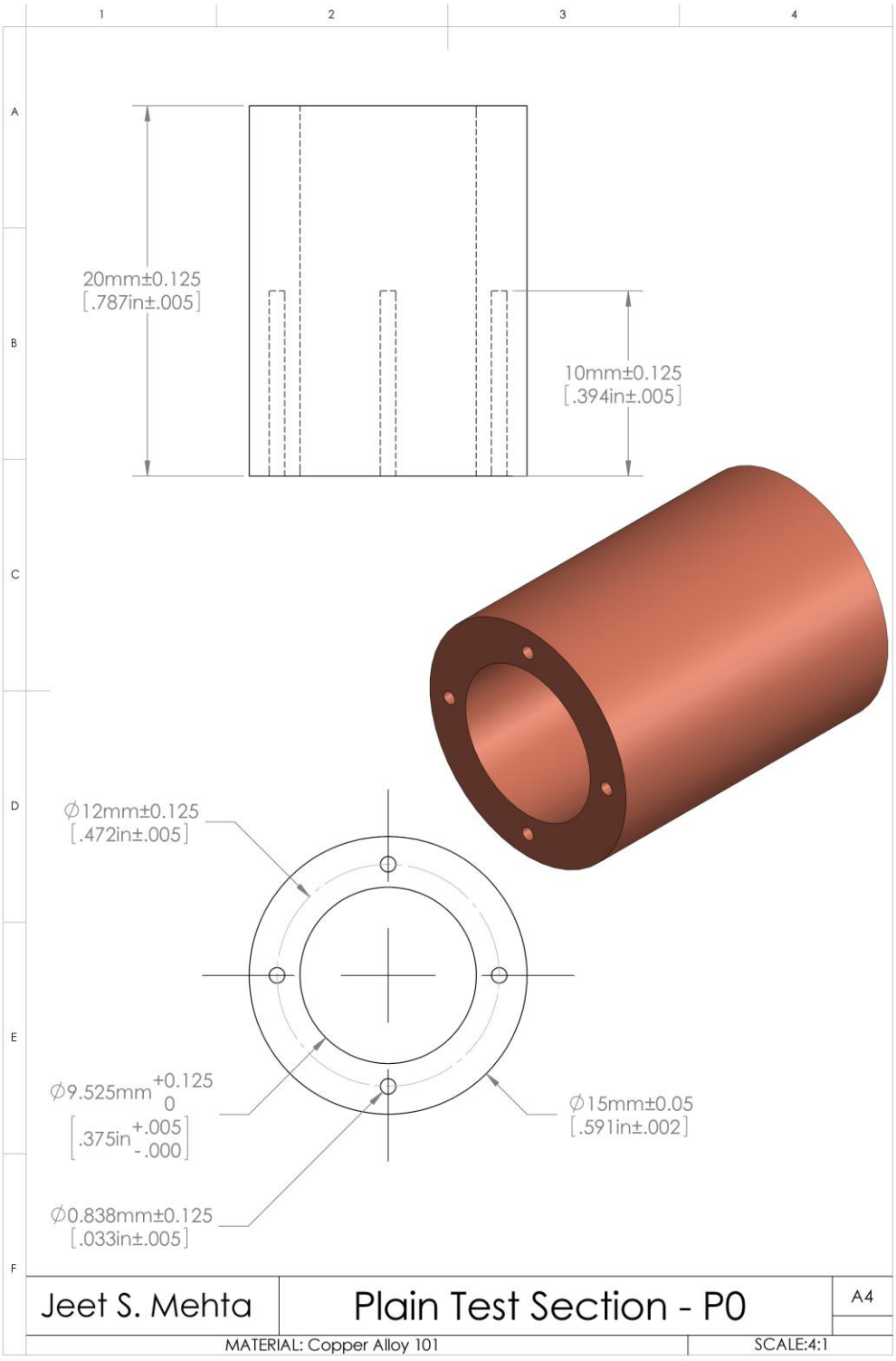

Figure 43: Technical drawing of the plain test section – P0

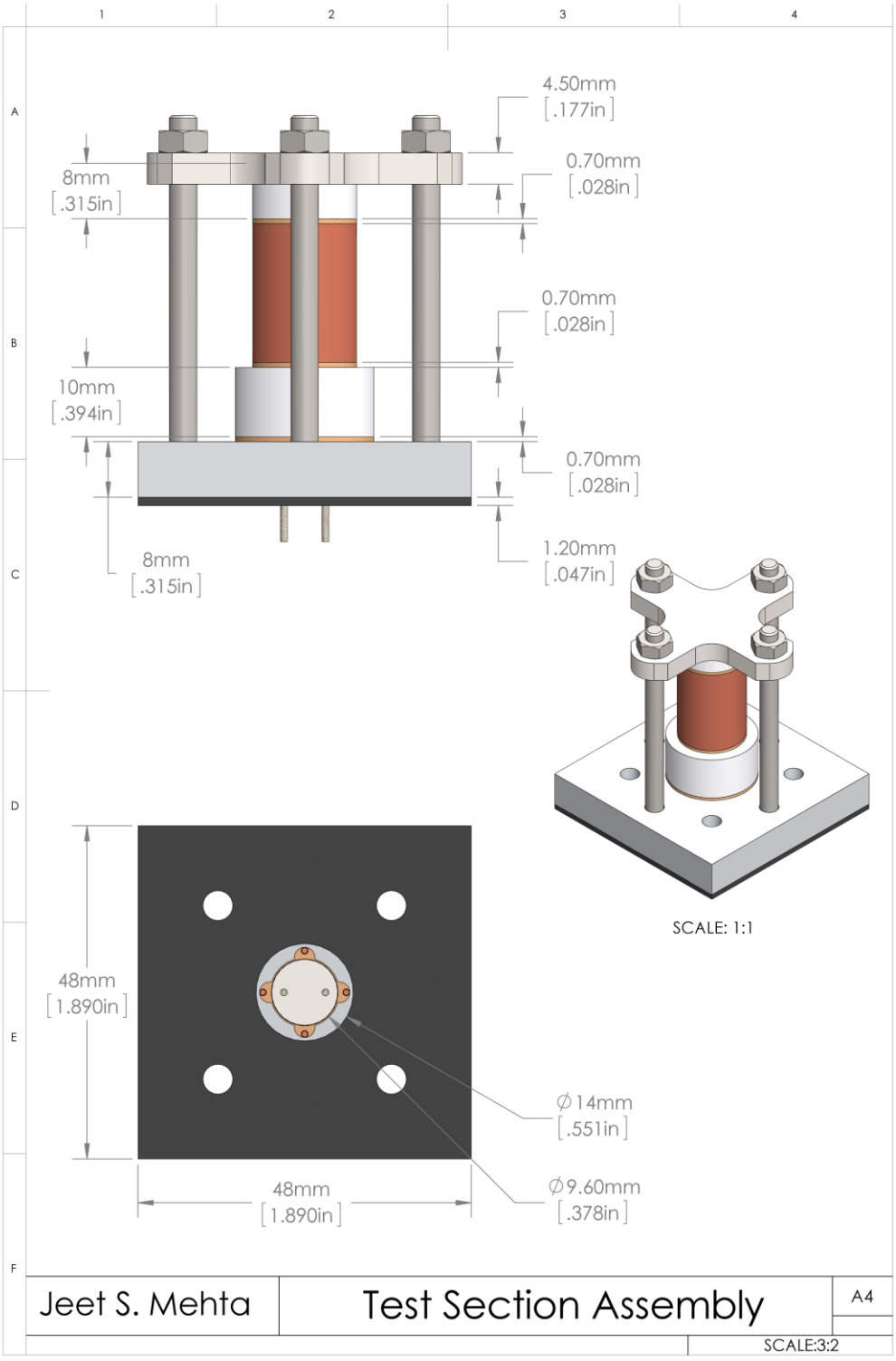

Figure 44: Technical drawing of the test section assembly

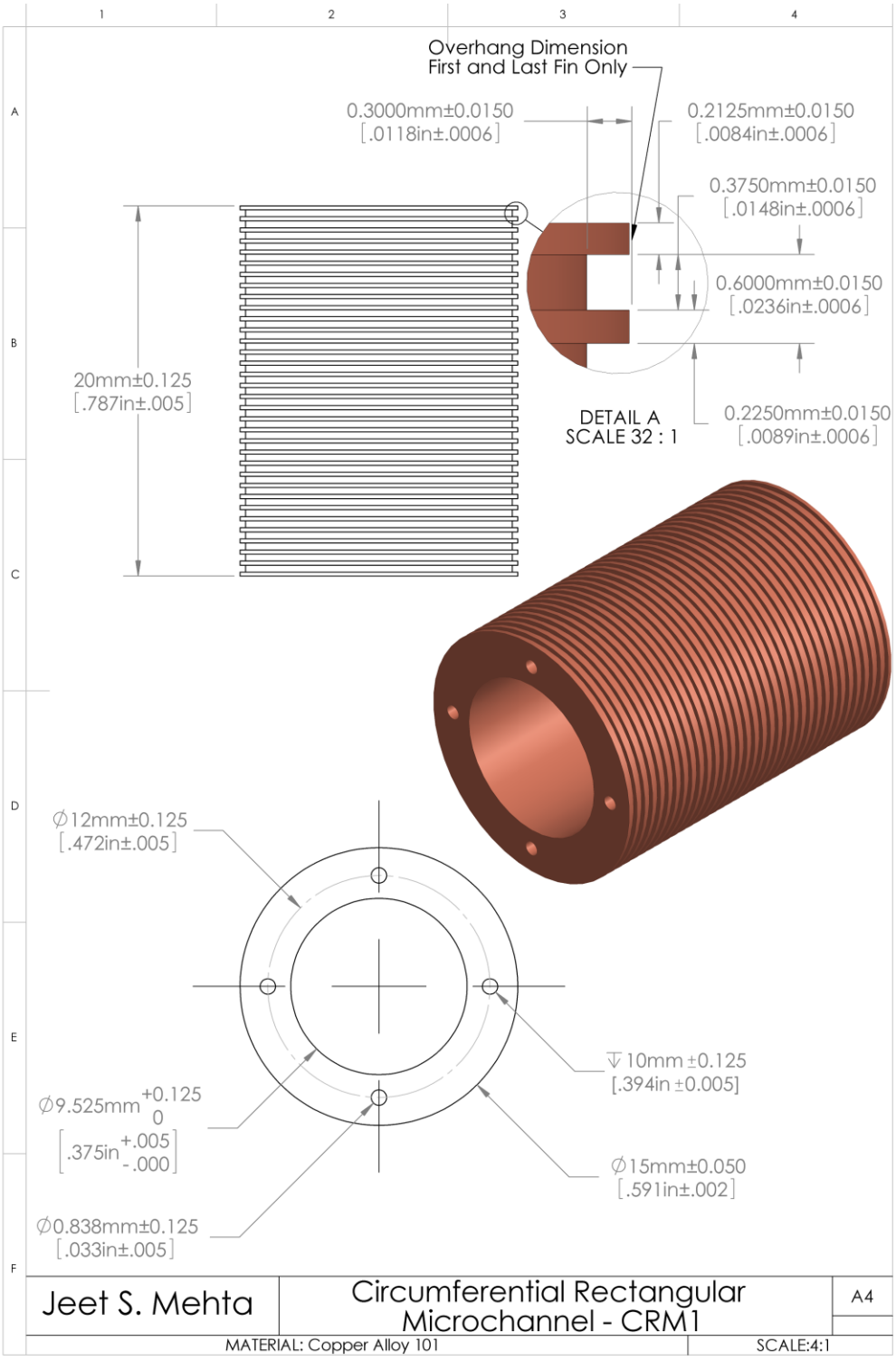

Figure 45: Technical drawing of the circumferential rectangular microchannel – CRM1 test section

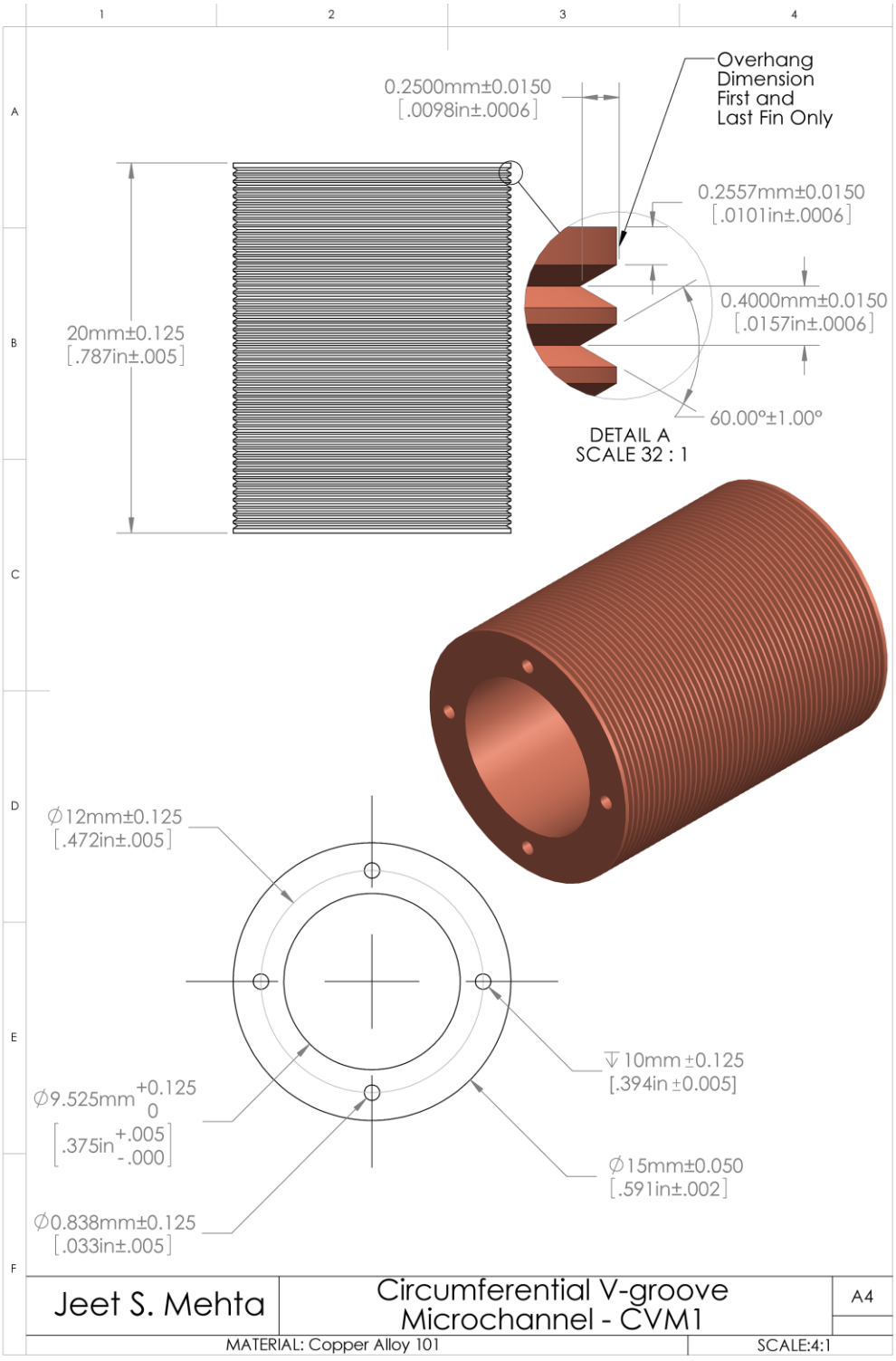

Figure 46: Technical drawing of the circumferential V-groove microchannel – CVM1 test section

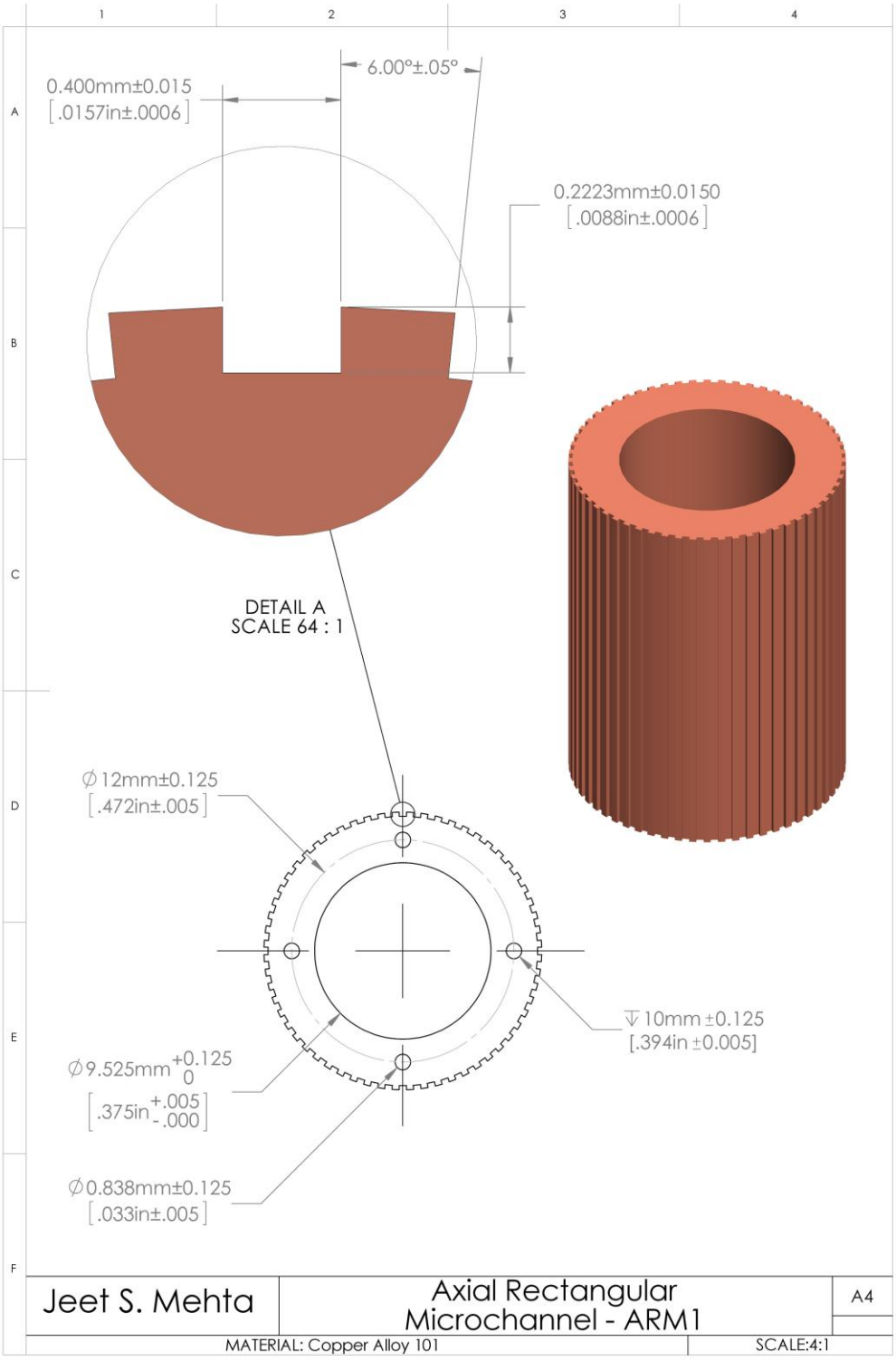

Figure 47: Technical drawing of the axial rectangular microchannel – ARM1 test section

Heat Loss Study Results

Test Section	*Percentage Axial Heat Losses*			
	Horizontal Orientation		**Vertical Orientation**	
	At minimum q_h	At maximum q_h	At minimum q_h	At maximum q_h
P0	2.03	0.40	1.91	0.43
CRM1	1.94	0.17	1.74	0.17
CRM2	2.06	0.16	1.68	0.18
CRM3	1.91	0.13	2.19	0.15
CRM4	1.72	0.15	1.42	0.17
CRM5	2.00	0.15	1.65	0.16
CRM6	1.95	0.15	1.79	0.17
CRM7	1.97	0.16	1.92	0.18
CRM8	2.06	0.17	1.91	0.20
CVM1	1.65	0.19	1.82	0.21
CVM2	1.73	0.19	1.68	0.19
CVM3	1.95	0.18	1.95	0.21
CVM4	1.67	0.18	1.61	0.20
CVM5	2.64	0.23	2.07	0.22
CVM6	1.73	0.19	1.53	0.19
ARM1	1.90	0.20	1.52	0.18
ARM2	1.53	0.18	1.13	0.17
ARM3	1.59	0.22	1.26	0.21
ARM4	1.46	0.21	1.20	0.20
ARM5	1.40	0.22	1.13	0.19
ARM6	1.68	0.23	1.34	0.18

Table 9: Detailed results of the heat loss study for all test sections under various conditions

Uncertainty Analysis: Equations and Derivations

Equations used for calculations:

$q_h = V \times I$
$q_r = q_h - q_{a,l}$
$T_{ave} = \frac{T_1 + T_2 + T_3 + T_4}{4}$
$T_s = T_{ave} - q_r \times \frac{ln(r_2/r_1)}{2\,\pi\,k\,L}$
$A_s = 2\,\pi\,r_2\,L$
$q_r'' = \frac{q_r}{A_s}$
$h = \frac{q_r''}{(T_s - T_5)}$

Uncertainty equations and derivations:

$\frac{U_{q_h}}{q_h} = \left[\left(\frac{U_V}{V}\right)^2 + \left(\frac{U_I}{I}\right)^2\right]^{1/2}$
$\frac{U_{q_r}}{q_r} = \frac{U_{q_h}}{q_h}$
$\frac{U_{T_{ave}}}{T_{ave}} = \left[\left(\frac{U_{T_1}}{T_1 + T_2 + T_3 + T_4}\right)^2 + \left(\frac{U_{T_2}}{T_1 + T_2 + T_3 + T_4}\right)^2 + \left(\frac{U_{T_3}}{T_1 + T_2 + T_3 + T_4}\right)^2 + \left(\frac{U_{T_4}}{T_1 + T_2 + T_3 + T_4}\right)^2\right]^{1/2}$

Derivation for Equation (8)

$$\frac{U_{T_s}}{T_s} = \left[\left(\frac{U_{T_{ave}}}{T_{ave}}\right)^2 + \frac{1}{2\,\pi}\left(\frac{U_X}{X}\right)^2\right]^{1/2}$$

$$where\ X = q_r \times \frac{ln(r_2/r_1)}{k\,L}$$

$$\frac{U_X}{X} = \left[\left(\frac{U_{q_r}}{q_r}\right)^2 + \left(\frac{U_{\left(\frac{r_2}{r_1}\right)}}{\left(\frac{r_2}{r_1}\right) \times ln\left(\frac{r_2}{r_1}\right)}\right)^2 + \left(\frac{U_k}{k}\right)^2 + \left(\frac{U_L}{L}\right)^2\right]^{1/2}$$

$$\boldsymbol{\frac{U_{T_s}}{T_s} = \left[\left(\frac{U_{T_{ave}}}{T_{ave}}\right)^2 + \frac{1}{2\,\pi} \cdot \left\{\left(\frac{U_{q_r}}{q_r}\right)^2 + \left(\frac{U_{\left(\frac{r_2}{r_1}\right)}}{\left(\frac{r_2}{r_1}\right) \times ln\left(\frac{r_2}{r_1}\right)}\right)^2 + \left(\frac{U_k}{k}\right)^2 + \left(\frac{U_L}{L}\right)^2\right\}\right]^{1/2}}$$

$$\frac{U_{T_s}}{T_s} = \left[\left(\frac{U_{T_1}}{T_1 + T_2 + T_3 + T_4}\right)^2 + \left(\frac{U_{T_2}}{T_1 + T_2 + T_3 + T_4}\right)^2 + \left(\frac{U_{T_3}}{T_1 + T_2 + T_3 + T_4}\right)^2\right.$$

$$+ \left(\frac{U_{T_4}}{T_1 + T_2 + T_3 + T_4}\right)^2 + \frac{1}{2\,\pi}$$

$$\left. \cdot \left\{\left(\frac{U_{q_r}}{q_r}\right)^2 + \left(\frac{U_{\left(\frac{r_2}{r_1}\right)}}{\left(\frac{r_2}{r_1}\right) \times ln\left(\frac{r_2}{r_1}\right)}\right)^2 + \left(\frac{U_k}{k}\right)^2 + \left(\frac{U_L}{L}\right)^2\right\}\right]^{1/2}$$

$$\frac{U_{A_s}}{A_s} = \left[\left(\frac{U_{r_2}}{r_2}\right)^2 + \left(\frac{U_L}{L}\right)^2\right]^{1/2}$$

Derivation for Equation (9)

$$\frac{U_{q_r''}}{q_r''} = \left[\left(\frac{U_{q_r}}{q_r}\right)^2 + \left(\frac{U_{A_s}}{A_s}\right)^2\right]^{1/2}$$

$$\boldsymbol{\frac{U_{q_r''}}{q_r''} = \left[\left(\frac{U_{q_r}}{q_r}\right)^2 + \left(\frac{U_{r_2}}{r_2}\right)^2 + \left(\frac{U_L}{L}\right)^2\right]^{1/2}}$$

Derivation for Equation (10)

$$\frac{U_h}{h} = \left[\left(\frac{U_{q_r''}}{q_r''}\right)^2 + \left(\frac{U_{T_s}}{T_s - T_5}\right)^2 + \left(\frac{U_{T_5}}{T_s - T_5}\right)^2\right]^{1/2}$$

$$\frac{U_h}{h} = \left[\left(\frac{U_{q_r}}{q_r}\right)^2 + \left(\frac{U_{r_2}}{r_2}\right)^2 + \left(\frac{U_L}{L}\right)^2 + \frac{\left(U_{T_s}\right)^2}{(T_s - T_5)^2} + \left(\frac{U_{T_5}}{T_s - T_5}\right)^2\right]^{1/2}$$

$$\boldsymbol{\frac{U_h}{h} = \left[\left(\frac{U_{q_r}}{q_r}\right)^2 + \left(\frac{U_{r_2}}{r_2}\right)^2 + \left(\frac{U_L}{L}\right)^2 + \frac{(T_s)^2}{(T_s - T_5)^2}\right.}$$

$$\boldsymbol{\left. \cdot \left\{\left(\frac{U_{T_{ave}}}{T_{ave}}\right)^2 + \frac{1}{2\pi} \cdot \left\{\left(\frac{U_{q_r}}{q_r}\right)^2 + \left(\frac{U_{\left(\frac{r_2}{r_1}\right)}}{\left(\frac{r_2}{r_1}\right) \times ln\left(\frac{r_2}{r_1}\right)}\right)^2 + \left(\frac{U_k}{k}\right)^2 + \left(\frac{U_L}{L}\right)^2\right\}\right\}}$$

$$\boldsymbol{\left. + \left(\frac{U_{T_5}}{T_s - T_5}\right)^2\right]^{1/2}}$$

Additional Experimental Results

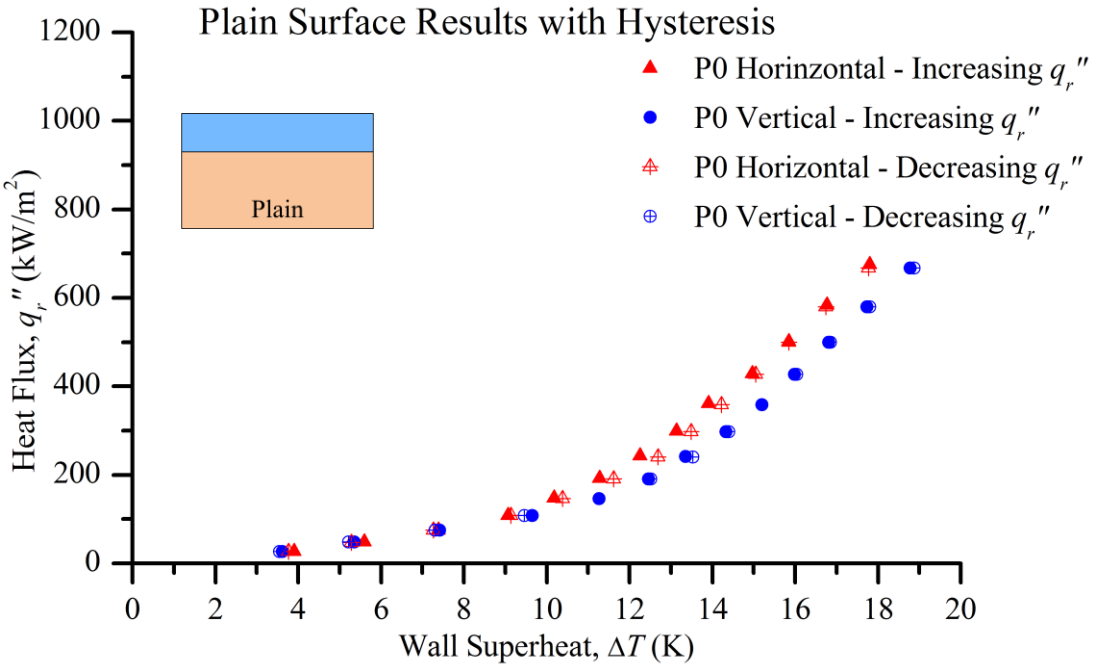

Figure 48: Boiling curves for the plain test sections (P0) in the horizontal and vertical orientation and showing its hysteresis

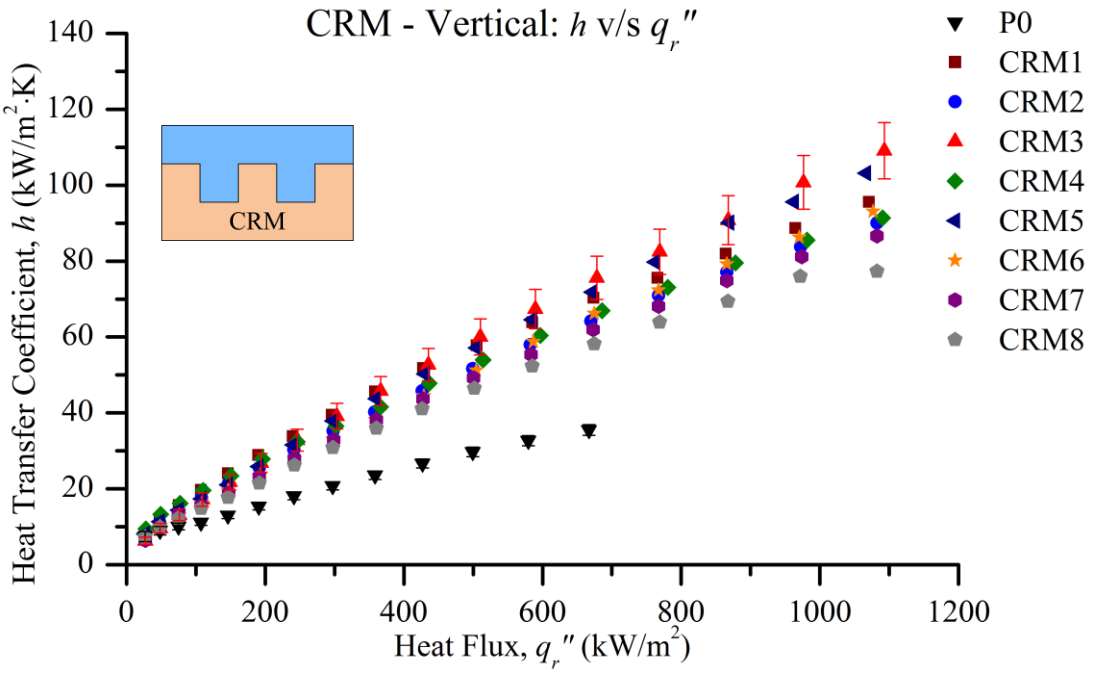

Figure 49: Plot of the heat transfer coefficient against the heat flux, comparing the CRM test section results in the vertical orientation

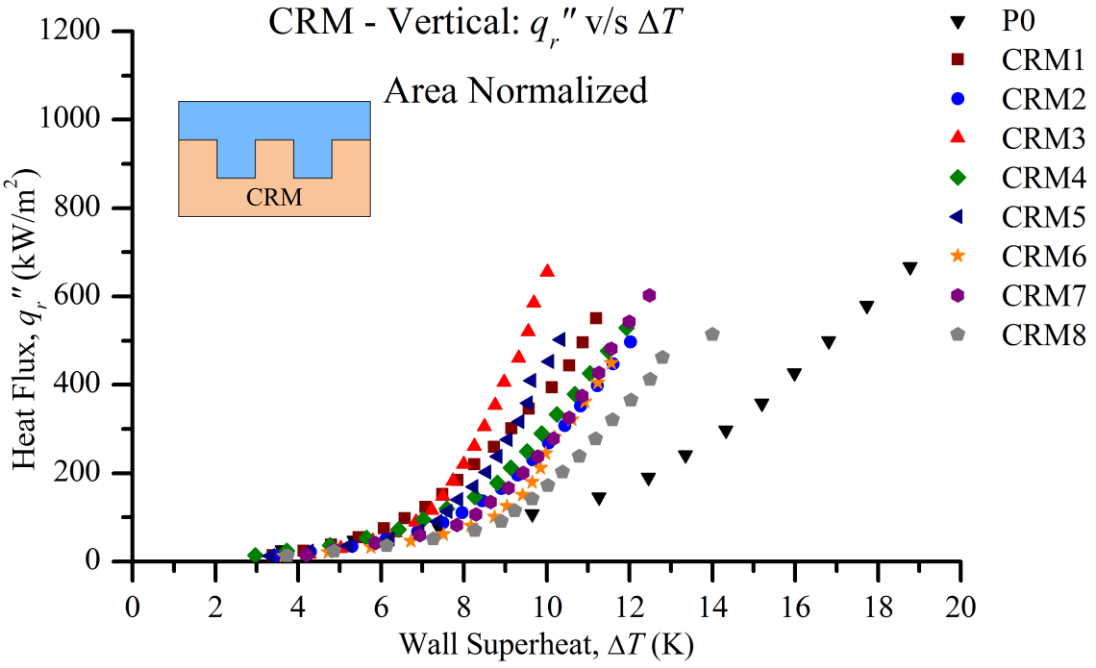

Figure 50: Boiling curves based on area normalized heat fluxes for the CRM test sections in the vertical orientation

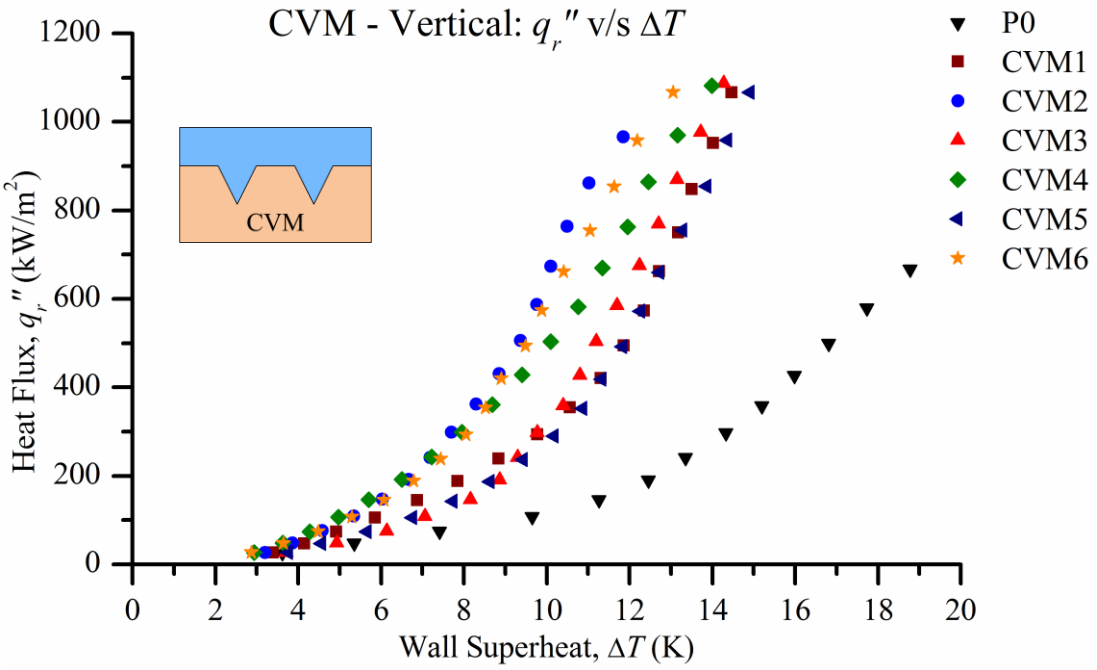

Figure 51: Boiling curves for the CVM test sections in the vertical orientation

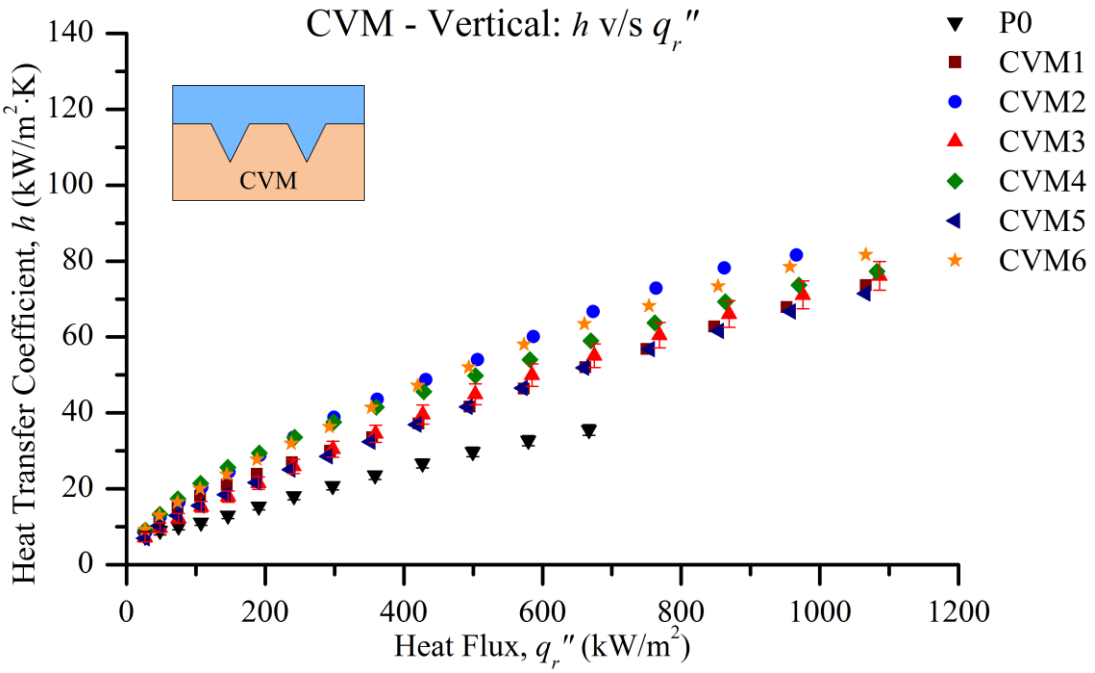

Figure 52: Plot of the heat transfer coefficient against the heat flux, comparing the CVM test section results in the vertical orientation

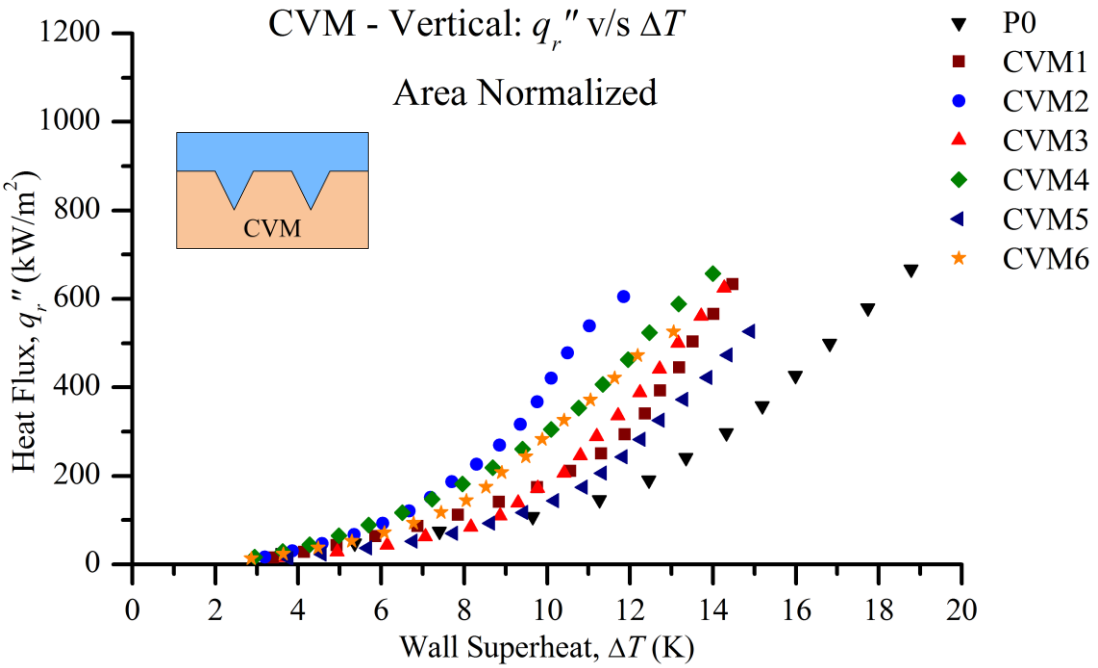

Figure 53: Boiling curves based on area normalized heat fluxes for the CVM test sections in the vertical orientation

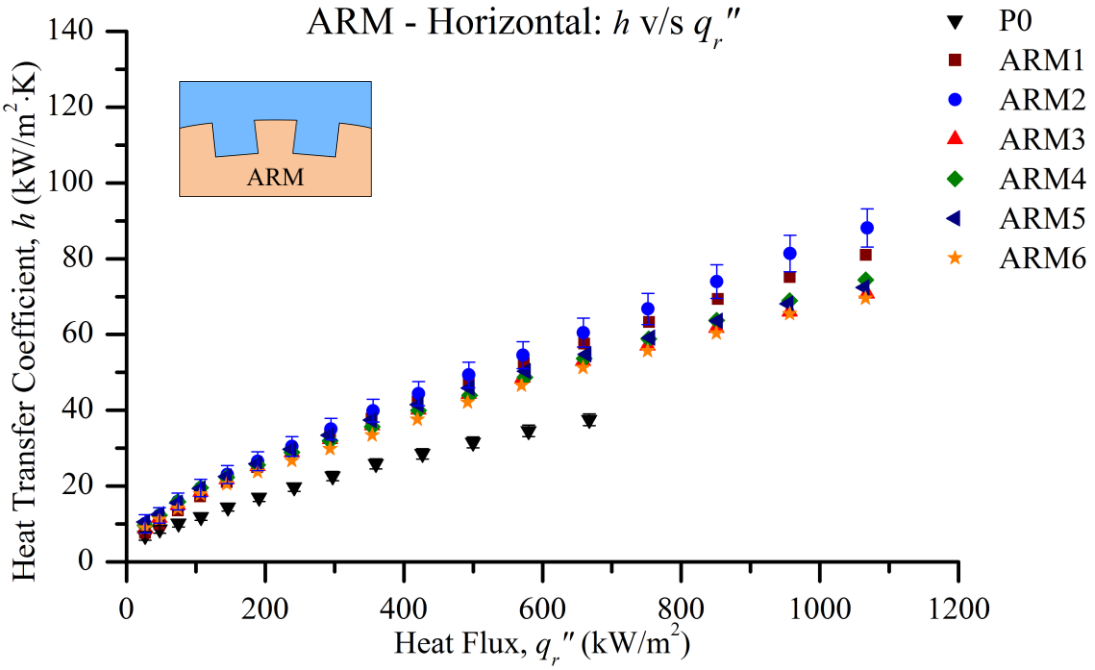

Figure 54: Plot of the heat transfer coefficient against the heat flux, comparing the ARM test section results in the horizontal orientation

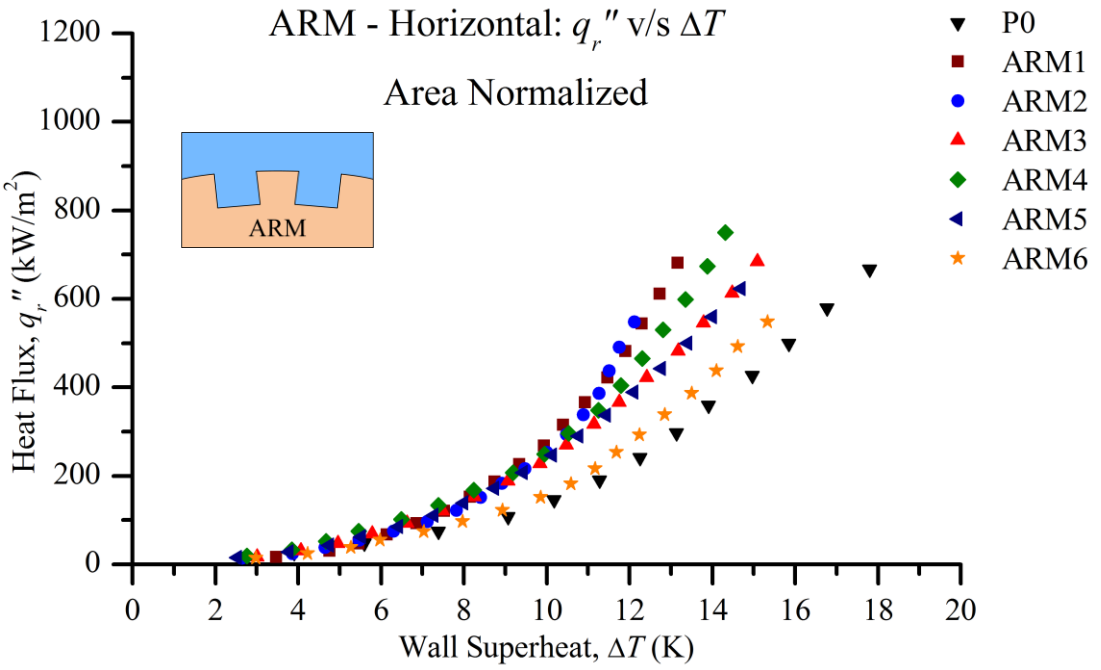

Figure 55: Boiling curves based on area normalized heat fluxes for the ARM test sections in pthe horizontal orientation